Università degli Studi di Padova

Dipartimento di Fisica e Astronomia "Galileo Galilei"

Modelling the Multiwavelength Emission of Ultra-Luminous X-ray Sources: Theory versus Observations

Coordinator: Prof. Giampaolo Piotto
Supervisor: Dott. Luca Zampieri

PhD candidate: Elena Ambrosi

Academic Year: 2017-2018

Contents

Abstract

Ultra-luminous X-ray Sources are point-like extragalactic X-ray Sources with bolometric luminosity higher than the Eddington limit for a 10 $M_{\odot}$ BH ($L_{Edd} \sim 2 \times 10^{39}$ erg s^{-1}). One of the main open problems regarding ULXs is to determine the nature and mass of their compact object and that of their donor. The main goal of this PhD Thesis is to investigate the nature of ULXs using their multiwavelength emission properties and to extend the treatment of the evolution of their binary systems including the effects of super-Eddington accretion. In this way we constrain the masses of the black holes and donor stars in these systems, and their accretion regime. We study the evolution of binary systems of Ultra-luminous X-ray sources and compute their optical emission assuming accretion onto a black hole via a non standard, advection-dominated slim disc with an outflow. We consider systems with black holes of $20M_{\odot}$ and $100M_{\odot}$, and donor masses between $8M_{\odot}$ and $25M_{\odot}$. Super-critical accretion has considerable effects on the optical emission. The irradiating flux in presence of an outflow remains considerably stronger than that produced by a standard disc. However, at very high accretion rates the contribution of X-ray irradiation becomes progressively less important in comparison with the intrinsic flux emitted from the disc. After Main Sequence the evolutionary tracks of the optical counterpart on the colour-magnitude diagram are markedly different from those computed for Eddington-limited accretion. Systems with stellar-mass black holes and $12 - 20M_{\odot}$ donors accreting supercritically are characterized by blue colors (F450W – F555W $\simeq -0.2 : +0.1$) and high luminosity ($M_V \simeq -4 : -6.5$). Systems with more massive black holes accreting supercritically from evolved donors of similar mass have comparable colours but can reach $M_V \simeq -8$. We then apply our model of super-Eddington accretion with outflow to systems with a wide range of BH and donor masses. We evolved the corresponding evolutionary tracks with the MESA stellar evolution code including the amount of orbital angular momentum removed from the systems because of the mass lost with the outflow. We applied our model to calculate the emission properties of binary systems accreting above Eddington to a number of ULXs with well studied stellar optical counterparts: NGC 1313 X-2, NGC 4559 X-7, NGC 5204 X-1, HolmbergII X-1 and NGC 5907 ULX-2. We found that binary systems with massive donors accreting above Eddington onto black holes in the mass range 25-55 $M_{\odot}$ can reproduce reasonable well their multiwavelength properties.

Chapter 1

Introduction

Ultra-luminous X-ray Sources are point-like extragalactic X-ray Sources with bolometric luminosity higher than the Eddington limit for a 10 $M_\odot$ BH ($L_{Edd} \sim 2 \times 10^{39}$ erg s^{-1}; Fabbiano 1989). The majority of them are X-ray binaries with a neutron star (NS) or a black hole (BH), most probably accreting above the Eddington limit (for a review see Feng and Soria 2011; Kaaret et al. 2017). In the past years, there has been an extensive debate on the possibility that the compact object is a stellar or a massive stellar BH accreting above Eddington (King et al. 2001; Zampieri and Roberts 2009; Mapelli et al. 2009; Belczynski et al. 2010; Feng and Soria 2011), or an Intermediate mass Black Hole accreting sub-Eddington (Colbert and Mushotzky, 1999; Miller et al., 2003, 2004). The recent discovery of pulsating ULXs (Bachetti et al. 2014; Fürst et al. 2016; Israel et al. 2017a,b; Carpano et al. 2018) led to the conclusion that the compact object can in fact also be a NS.

Therefore, one of the main open problems regarding ULXs is to determine the nature and mass of the compact object and that of the donor. In fact, being these objects hosted in nearby galaxies, the magnitude of their optical counterparts are very faint ($m \geq 23$ mag) and, being the environments typically rather crowded, uniquely identifying them is very hard (nowadays only a handful of unique ULXs optical counterparts have been identified (see Tao et al. 2011; Feng and Kaaret 2008; Tao et al. 2012; Zampieri et al. 2012; Gladstone et al. 2013 and references therein). As a consequence, their mass function cannot be easily measured. The scantly available measurements are mostly based on emission lines (e.g. Roberts et al. 2011). Stellar absorption lines are rarely detected (Motch et al., 2014). These facts concur against the possibility of a direct measurement of the masses of the donor and the compact object of these systems.

Two are the ULXs for which the donor mass has been estimated. The first is NGC 7793 P13 (Motch et al., 2014), whose optical spectrum shows absorption lines typical of a B9Ia supergiant star with mass in the range 18-23 $M_\odot$. Moreover, the compact object in this source has been shown to be a neutron star (Israel et al. 2017b; Fürst et al. 2016). Also the donor star of M101 ULX$-$1 has been classified thanks to the presence of helium and nitrogen emission lines and absence of hydrogen and carbon emission lines. It has been classified as a Wolf-Rayet star, whose mass is in the range 19 ± 1 $M_\odot$ (Liu et al., 2013).

As summarized in Zampieri and Roberts (2009), the BH mass of ULXs can be estimated through some indirect methods. All of them strongly depend on the structure of the accretion disc and

on the accretion regime. All the models which assume sub-Eddington accretion support the existence of Intermediate Mass Black Holes (IMBHs) of hundreds of solar masses, while models which assume super-Eddington accretion favour less massive BHs, with an upper limit of about 100 $M_{\odot}$ (Carpano et al. 2018; Feng and Soria 2011). With the launch of *NuSTAR* the analysis of the hard X-ray spectrum supported the conclusion that the emission is consistent with the expectations for super-Eddington accretion (e.g. Mukherjee et al. 2015; Walton et al. 2015).
Despite the considerable effort that has been made in the past years, constraining the masses of the donor and the compact object in ULXs, when no mass function measurement or detection of pulsations are available, is still difficult.
Patruno and Zampieri (2008, 2010) were among the first to evolve ULX binaries accreting sub-critically onto BHs and calculate their X-ray luminosity and optical emission properties on the color-magnitude-diagram. They computed the total emission from the donor and the disc, accounting for X-ray irradiation. Their study shows that, if the photometry is sufficiently accurate, it is possible to constrain not only the mass of the donor, but also that of the BH. It is important to notice that Patruno and Zampieri (2008), hereafter PZ, account for the optical emission of the disc, whose contribution is often neglected in the optical studies of ULXs.

The work of this thesis fits in this area and aims at extending the model of PZ to the case of super-Eddington accretion. Super-Eddington accretion is believed to take place in a large number of ULXs because of the characteristic properties of their X-ray spectra and the variability observed at high energies (Middleton et al., 2011, 2015a). In addition to this, most ULXs reside in O-B associations so that it is more likely that the donor star is a blue giant or a super-giant capable to transfer a large amount of mass on the compact object (e.g. Podsiadlowski et al. 2003; Patruno et al. 2005) .
The main goal of my PhD thesis is to investigate the nature of ULXs using their multiwavelength emission properties and to extend the treatment of the evolution of their binary systems including the effects of super-Eddington accretion.
This thesis contains 7 chapters.
In chapter 2 we will summarize the main properties and open questions on ULXs.
In chapter 3 we will introduce the reader to the theoretical background which is at the basis of the topic discussed in this thesis: binary evolution and accretion disc theory.
In chapter 4 we will describe our model and apply it to two ULXs: NGC 1313 X-2 and NGC 4559 X-7. The work contained in this chapter has been accepted for publication in MNRAS (Ambrosi and Zampieri, 2018).
Chapter 5 is dedicated to present the results of the calculation of a more extended grid of tracks using the MESA stellar evolution code and to show their evolution on the color-magnitude diagram.
In chapter 6 we present our model of the multiwavelength emission of ULXs and apply it to five sources with unique optical counterparts: NGC 1313 X-2, NGC 4559 X-7, NGC 5204 X-1, HolmbergII X-1, NGC 5907 ULX-2.
Finally, in chapter 7 we summarize the results obtained in this thesis and complete our discussion with a brief description of the potential future projects related to the work presented here.

Chapter 2

Ultra-luminous X-ray Sources

2.1 Properties of Ultra-luminous X-ray Sources

Figure 2.1: Composite optical (red, green and blue) and X-ray (purple) image of the galaxy M51 with its brightest ULX. Credit: NASA

This thesis is devoted to the study of Ultra-luminous X-ray Sources (ULXs). As already mentioned above, they are point-like, off-nuclear X-ray sources with an X-ray luminosity higher than the Eddington limit for a 10 $M_{\odot}$ BH: $L_x \gtrsim 10^{39} erg \cdot s^{-1}$ (Fabbiano 1989; Fabbiano et al. 2006).
They have been discovered in nearby galaxies and are associated mainly with different environments: star-forming regions or young stellar environments in spiral galaxies, or dwarf irregular galaxies (e.g. Ramsey et al. 2006, Pakull et al. 2006, Liu et al. 2007). In some cases they are associated with older stellar populations in elliptical galaxies (Feng and Kaaret 2008, Roberts et al. 2008).

Their observational properties, as the X-ray luminosity, the variability and the spectral changes suggest that ULXs are compact objects accreting via a disc (Makishima et al. 2000; Feng and Soria 2011).
Since their discovery, their observational properties revealed that we are dealing with binaries very different from the better known Galactic X-ray binaries (Mizuno et al., 2001), which makes them very interesting.
Their high X-ray luminosities suggested at the beginning that the mass of the compact object was higher than the average masses of the BHs observed in our Galaxy if standard accretion occurs. It was proposed (Colbert and Mushotzky, 1999) that they could be IMBHs with masses of $\sim 10^3\ M_{\odot}$.
Further investigations revealed also that their X-ray spectral properties are unusual if compared to those observed in Galactic X-ray Binaries (XRBs) opening the possibility to explain ULXs in terms of alternative accretion disc scenarios, without invoking intermediate mass BHs. It was proposed that super-Eddington accretion discs around stellar-mass or slightly more massive BHs, as the slim discs models, could reproduce the spectra of ULXs (Ebisawa et al., 2003).
A significant effort was devoted in recent years to understand the nature of ULXs. With the advent of more sensitive X-ray telescopes (*Chandra, XMM-Newton, NuSTAR*) the spectral properties of ULXs could be analyzed in greater detail. Gladstone et al. (2009) and Sutton et al. (2013b) identified the so-called *Ultra luminous state*, which is characterized by the presence of some important features in ULXs spectra. This led to the conclusion that ULXs should be stellar-mass or massive (up to 100 $M_{\odot}$) BHs accreting with marginally or highly super-Eddington rates from massive donors. In fact Mapelli et al. (2009) and Zampieri and Roberts (2009) explored the massive BH scenario, finding that low-metallicity environments could produce BHs in the range of 30-80 $M_{\odot}$ and that super-Eddington accretion onto these BHs provides good agreement with the observed properties of ULXs.
Understanding the nature of ULXs became more and more challenging after the discovery of the first pulsating ULX (Bachetti et al., 2014), which unequivocally showed that ULXs can also be accreting neutron stars. This discovery has been confirmed by the identification of other three Pulsar ULXs (Israel et al., 2017a,b; Carpano et al., 2018) whose emission properties can only been explained in terms of super-Eddington accretion.
ULXs appear to be the sources where super-Eddington accretion reveals itself in a variety of phenomenological modes. A strong evidence of such an extreme regime is also the presence of outflows, inferred from the detection of radio and optical giant nebulae (Pakull and Mirioni 2002; Miller et al. 2005), broad optical emission lines (Fabrika et al., 2015) and blue-shifted X-ray absorption lines (e.g. Pinto et al. 2016b, 2017). Considerations on the energy balance involved in the production of these features, leads to the conclusion that the observed X-ray luminosities are lower than the kinetic energy spent to launch outflows (Kaaret et al., 2017).

2.2 Estimate of the BH mass from X-ray spectral fitting

In this section we will summarize some indirect methods based on the X-ray spectra which were used early to estimate the BH mass, showing that they depend on the accretion state of

a ULX. In fact, different spectral and accretion regimes require different BH masses to produce comparable ULX luminosities (Zampieri and Roberts, 2009).
If the observed spectrum is fitted with a multi-color disc black body (MCD), which represents emission from a standard accretion disc, the BH mass can be estimated from (Lorenzin and Zampieri, 2009):

$$\frac{M_{BH}}{M_\odot} = f^2 \frac{67.5}{b} \left(\frac{D}{1Mpc}\right) \left(\frac{K_{BB}}{cosi}\right)^{1/2} \tag{2.1}$$

where D is the distance of the source, f a colour-correction factor, b the inner disc radius normalized to the gravitational radius and K_{BB} the MCD normalization inferred from the spectral fit. On the other hand, if a super-Eddington accretion disc is adopted, the mass estimate is different. For slim discs models, one can use the spectral fitting results of Vierdayanti et al. (2006) :

$$R_{in} = \chi \kappa^2 \sqrt{\frac{L_{bol}}{4\pi\sigma T_{in}^4}} \qquad R_{in} = 3\beta R_s = 8.86\beta \left(\frac{M}{M_\odot}\right) \mathsf{km} \tag{2.2}$$

where R_{in} is the radius of the last stable Keplerian orbit of the BH, T_{in} is the inner disc temperature, R_s the Schwarzschild radius, β a parameter which depends on the BH spin, $\chi = 0.412$ is a correction factor and $\kappa \sim 1.7$ is the spectral hardening factor.
As discussed in Zampieri and Roberts (2009) the difference in the estimate of the BH mass is large and depends on the disc model used for the fitting. We report the illustrative example of the mass estimate for NGC 1313 X-2: for an X-ray luminosity of $1.5 \cdot 10^{40} erg \cdot s^{-1}$, Eq. 2.1 for sub-Eddington accretion gives a BH of 300 $M_\odot$ while Eq. 2.2 for a slim-disc gives a BH mass of 16 ± 1 $M_\odot$ (taking for the parameters b, β, χ and κ the values reported in Vierdayanti et al. 2006 and Vierdayanti et al. 2008).

2.3 X-ray properties

The high X-ray luminosity observed in ULXs is not the only characteristic which distinguishes them from the classical Galactic Black-Hole binaries (GBHBs). In fact, their spectral shapes and their variability are also very different. In the following, we will briefly summarize the X-ray spectral properties observed in ULXs. The first ASCA spectra, in the 0.5-10 keV band, were fitted with a single spectral component, like those used for GBHBs, but with higher temperatures ($kT_{in} \approx 1.1 - 1.8$ keV) and luminosities (Makishima et al., 2000). This behaviour suggested the presence of massive BHs. Later, early observations with *Chandra* and *XMM-Newton* revealed that single component models, like power-law or simple accretion disc model (DBB), were statistically excluded with high quality spectra. They were best modelled instead using a second component or more complex single component models (Kaaret et al., 2017).
When ULXs were observed with the good quality spectra obtained with *XMM-Newton* and *Chandra*, the fitting with the two-component model used for GBHBs gave very cool disc temperatures ($kT_{in} \approx 0.1 - 0.3$ keV) and relatively hard power-laws ($\Gamma \sim 1.5 - 3$). These brought to the conclusion that the masses of ULXs BHs were $\sim 10^3$ $M_\odot$, the so-called Intermediate Mass Black Holes (IMBHs) (Kaaret et al. 2003; Miller et al. 2003; Cropper et al. 2004). As pointed out by Kaaret et al. (2017), these spectra were different from those of GBHBs also because the

power-law was dominant in regions of the spectrum where the disc dominated in GBHBs.
A very important discovery for what concerns the ULXs spectra was the identification of a curvature in the range 2-10 keV. (Roberts et al. 2005; Feng and Kaaret 2005; Stobbart et al. 2006; Gladstone et al. 2009). This curvature is an important signature of the ULXs spectra and extends above 10 keV, as it has been shown with *NuSTAR* observations (Bachetti et al. 2013; Walton et al. 2014). It is characterized by a break in the range 2-7 keV (Gladstone et al. 2009), in contrast to GBHBs, which display breaks in the spectra at above 60 keV (McClintock and Remillard, 2010).
Is then clear that the spectral appearance of ULXs cannot conform to the standard sub-Eddington states which are observed in GBHBs.

2.4 Spectral Models

The spectral shape of ULXs can be described as a soft excess and a hard curvature above ~ 2 keV. Moreover, at the highest energies they are described by a cool and optically thick corona. ($kT_e \sim 1-6$ keV and $\tau > 6$).
It is now commonly accepted that the spectral properties of ULXs, assembled in the so-called *ultraluminous state* (Gladstone et al. 2009; Sutton et al. 2013b), are the signature of $\sim$ Eddington or super-Eddington accretion. Gladstone et al. (2009) distinguish three different regimes among ULXs spectra: the broadened disc, the hard ultraluminous state and the soft ultraluminous state. Another class of ULXs spectra is represented by the Supersoft Ultraluminous. In Fig. 2.2a the ULXs main X-ray spectral features are compared to the two common states of GBHBs. Two main spectral states are identified in GBHBs: an hard (low) state and a soft (high) state. The hard state is dominated by a power-law component with a cut-off at energies above 100 - 200 keV. The soft state is instead dominated by a strong black body component Zdziarski and Gierliński 2004; Remillard and McClintock 2006. The characteristics of the three states of ULXs, depicted in Fig. 2.2a and compared to the two common states of GBHBs, can be summarized as follows (Gladstone et al. 2009; Sutton et al. 2013b, see also Kaaret et al. 2017):

- The **Ultraluminous (UL) state** is a two component spectra which can be hard (blue solid line) or soft (red solid line) depending on the spectral region of its highest peak. It characterizes at most the more luminous ULXs. They also differ in the variability properties: the hard ultraluminous spectra have fractional variability $\ll 10\%$, while soft ultraluminous ULXs display higher variability (fractional variability up to 10-30 %). The variability is stronger in the high energy tail of the spectrum ($> 1keV$). Both these states show a soft excess and a turnover in the hard tail of the spectrum.

- The **Broadened disc (BD)** (green solid line) is instead a single peaked disk-like spectrum which cannot be fitted by a simple multicolor disc black body due to its broadness. It is well fitted by a p-free disc model which gives $p \sim 0.6$, where p is the exponent of the power-law that represents the radial dependence of the disc temperature. It is the dominant spectral shape for luminosities lower than $\sim 3 \cdot 10^{39} ergs^{-1}$. Sutton et al. (2013b) suggested that this state can be the connecting feature between the standard sub-Eddington Black

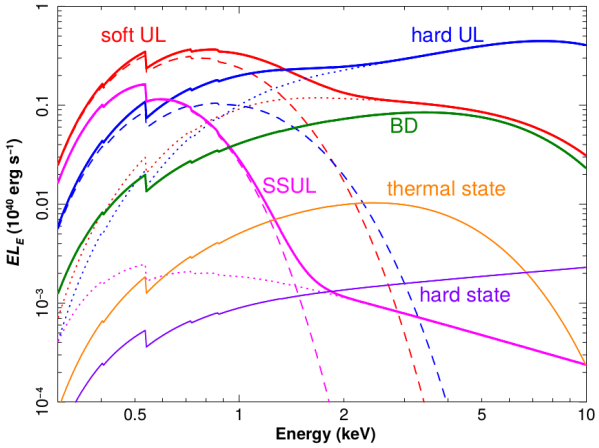

(a)

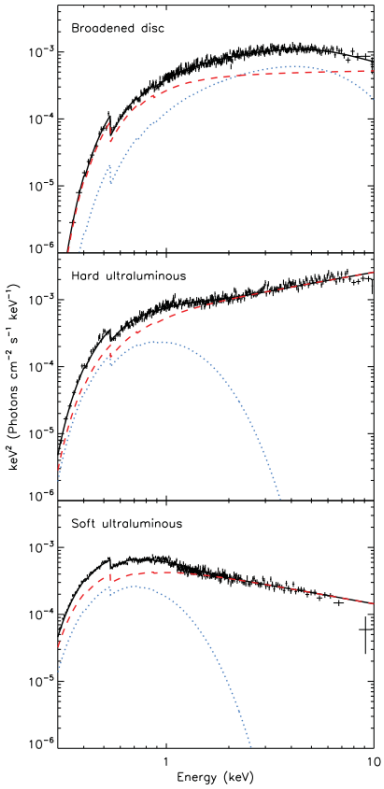

(b)

Figure 2.2: a)The soft and hard UL states are modelled with varying contributions from a disc-blackbody (dashed line) and a corona (dotted lines) component, while the SSUL with a black-body (dashed line) plus a power-law (dotted line) component. The BD state is often well reproduced with a p-free disc model. Taken from Kaaret et al. 2017. b) Spectra of three ULXs which show the hard and soft UL and the BD spectral states. From top to bottom: NGC 1313 X-2, Hol IX X-1 and NGC 5408 X-1. (Sutton et al. 2013b)

Hole Binaries and the super-Eddington ULXs, describing systems accreting at marginally super-critical rates.

- The **Supersoft ultraluminous (SSUL)** state produces the bulk of the flux below 1 or 2 keV. It is composed by a cool blackbody component, with typical temperatures of about 100 eV (Kaaret et al. 2017) and a high energies faint power-law component. The luminosity observed in this state is below $10^{39} erg\ s^{-1}$ but, if we correct for absorption from an extended photosphere which is believed to cover the innermost regions of the disc, their luminosities is higher (Urquhart and Soria, 2016).

Fig. 2.2b shows the spectra for three ULXs that have the different spectral states described above.

X-ray spectral variability

The spectra of ULXs are found to change between different epochs: in some sources the variation has been found to be $\sim 50\%$. Moreover, some ULXs display state transitions with short time scale: NGC 1313 X-2 (X-2) has been observed both with hard UL spectra and low luminosities and BD disc spectral shapes at high luminosities (Pintore and Zampieri 2012; Mukherjee et al. 2015). Moreover, Bachetti et al. (2013) found that the variability of X-2 occurs in timescales of weeks.
For what concerns the temporal variability, Heil et al. (2009) analyzed 16 ULXs and found that there are two group of sources, depending on their Power Density Spectra (PDS): those with a well defined variability and those without variability. This behaviour is independent from their spectral shape, at variance with GBHBs, whose state can be inferred from their variability.

X-ray Evidence of Outflows

From X-ray emission it is possible to determine also the presence of outflows which can be signatures of super-Eddington accretion. Middleton et al. (2015b) interpret the residuals from *XMM-Newton* spectra with high signal to noise ratio, as absorption from a ionized medium which is being launched as an outflow at velocity $v \approx 0.2c$. Later, outflow in ULXs were confirmed by Pinto et al. (2016b) which see rest frame emission and also blue shifted absorption in the spectra of NGC 1313 X-1. Similar features were found also in NGC 5408 X-1 .

2.5 Optical properties

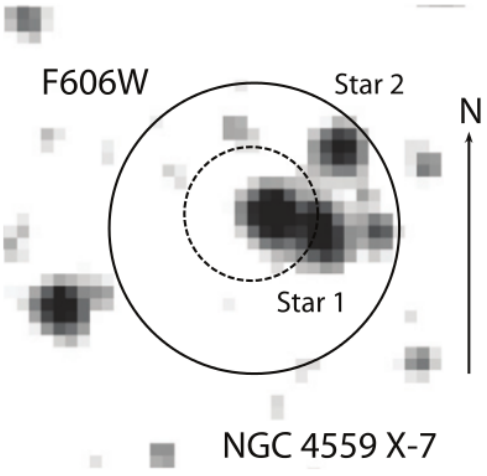

Figure 2.3: Optical counterpart of the ULX NGC 4559 X-7 (Tao et al., 2011)

The analysis of ULXs Optical counterparts is a very difficult task, because they are extra-galactic objects hosted in crowded environments. Also for the nearest ones, it is very difficult to isolate unique optical counterparts. Thank to the work of several authors including Tao et al. (2011) and Gladstone et al. (2013) the optical counterparts of $\sim$ 20 nearby ULXs have been uniquely identified using the *Hubble Space Telescope* (HST). Fig 2.3 shows the *HST* image in

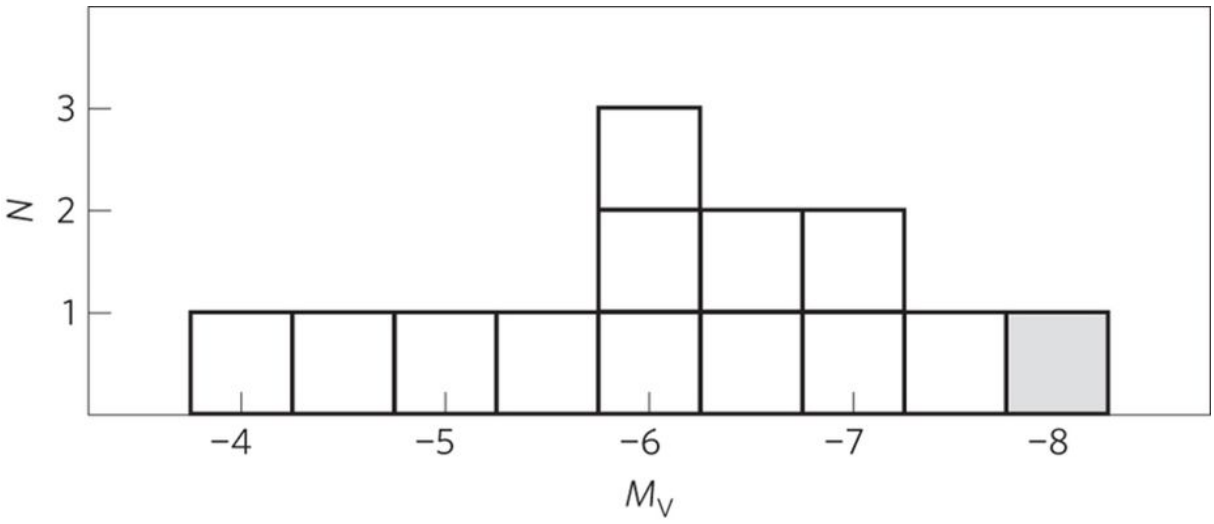

Figure 2.4: Number ULXs observed with a given magnitude (Fabrika et al., 2015) (The shadowed square represents the Galactic X-ray binary SS 433 for comparison.)

the F606W filter of the ULX NGC 4559 X-7. It shows the technique which is used to isolate ULXs optical counterparts from the environment: the X-ray position of the ULX (solid circle) is superimposed to the optical image and after registering the two images by means of an accurate astrometric procedure, the corrected position (dashed circle) is found. From Fig 2.3 it can be easily understood which are the difficulties to find an unique counterpart if the environment is very crowded and/or the source very faint.

The optical counterparts of ULXs exhibit high V magnitudes, in range -3 − -8 and blue colors (-0.6 − +0.4) (see Fig. 2.4). It is important to underline that also when the magnitudes in more than 2 filters are available, the optical Spectral Energy Distribution (SED) observed in different epochs does not reveal a single stellar spectral type. Tao et al. (2011) analyzed 13 sources and found that, among them, only the optical counterparts of two sources, when analyzed, give an unique estimate for the stellar spectral type: the counterpart of IC 342 X-1 turns out to be a F5 Ib-Iab and that of NGC 4559 X-7 a B2-B5 Ia. Also Gladstone et al. (2013) analyzed the optical counterparts of several ULXs. They resolved the unique counterpart for 22 ULXs. The approach that they adopted produces large errorbars in the magnitude measurements of some sources, that are not sufficiently accurate for our puposes. We will then not consider them further in this work.

We also underline that, being absorption lines absent in almost all ULXs, it is commonly believed that the bulk of optical flux is emitted by the accretion disc, which is affected by self-irradiation, as optical variability suggests. Detailed studies by Copperwheat et al. (2005); Patruno and Zampieri (2008, 2010); Zampieri et al. (2012) showed that optical emission is strongly affected by the flux emitted by the disc and by the X-ray reprocessing. Moreover, these sources can exhibit strong variability, as has been seen for NGC 1313 X-2.

Optical imaging permits also to detect the presence of optical nebulae associated with some ULXs. As reported by Kaaret et al. (2017), these nebulae tend to be large and very extended, up to tens or hundreds of parsecs. According to their observational properties, two formation

channels of the optical nebulae have been proposed. They can be powered by shocks which occur when the outflow of an ULX interacts with the surrounding medium or they can be produce by the X-ray photoionization of the nebula by the ULX (Kaaret et al., 2017). Optical nebulae expand at rates that can be supersonic ($\sim 150 km/s$). This velocity, together with the nebula size, can be used to estimate the age of the nebula, evaluated to be about 1 Myr by Roberts et al. (2003).
Optical emission can also reveal the presence of outflows. As pointed out by Kaaret et al. (2017), optical spectra of some ULXs shows broad emission lines, with width of 500-1500 km/s, in the Balmer series and in HeII λ4686. Fabrika et al. (2015) claim that these lines are produced by radiatively accelerated winds. This would be a further element in favour of super-Eddington accretion.

2.6 Environment and Formation Scenarios

The peculiarity of ULXs resides not only in their high luminosity and peculiar spectral properties. They are intriguing also for the environment in which they are observed. Many of them are located in or close to young O-B associations (see e.g. the population studies performed by Soria et al. 2005; Grisé et al. 2008; Goad et al. 2002), often embedded in low metallicity environments and/or high star-forming regions (Mapelli et al. 2011b; Wolter et al. 2015). A large number of ULXs has been found also in the young and star forming rings of ring galaxies (Wolter et al. 2018). Indeed, these galaxies have gone through head-on collisions, which triggered strong density perturbations, inducing star formation.
To shed light on the channels through which these objects can form, several authors performed dedicated studies: Zampieri and Roberts (2009); Mapelli et al. (2009) and Belczynski et al. (2010) showed that low metallicity environments lead to the formation of massive stellar black holes by direct collapse from massive stars. Mapelli et al. (2011a) howed that binary systems with massive BHs may form from dynamical exchange in young star cluster with low metallicity. Moreover, Mapelli and Zampieri (2014) found that in young star clusters 44% of binary systems which undergo a RLOF phase, formed through dynamical exchange. These studies support the notion that a fraction of ULXs host massive BHs accreting above Eddington.

Chapter 3

Accreting binary systems

3.1 Roche Lobe Overflow

Accreting binary systems are very complex objects: their phenomenology can be understood considering many physical and astrophysical aspects.
They can be divided into three classes: detached, semi-detached and contact binaries. *Detached binaries* have only dynamical interactions: they orbit around their common center of mass without mass transfer episodes. *Interacting binaries*, or *semi-detached binaries*, are characterized by mass transfer from one star to the other. In *Contact binaries*, the two stars transfer mass and heat one to another.
Roche lobe Overflow (RLOF) (Roche 1873, Kopal 1959), is the most common and efficient way through which mass transfer can occur.
Let us consider the three-body restricted problem and imagine two stars with masses M_1 and M_2 orbiting around their common center of mass (CM) with circular Keplerian orbits.[1] Let us introduce a test particle with negligible mass, such that it does not perturb the potential of the two stars. In stationary conditions, the test particle feels, in a frame co-rotating with the binary, a potential which depends on the two star masses, the Roche potential:

$$\phi_R = \frac{GM_1}{|\mathbf{r}-\mathbf{r}_1|} - \frac{GM_2}{|\mathbf{r}-\mathbf{r}_2|} - \frac{1}{2}\left|\boldsymbol{\omega}\times\mathbf{r}\right|^2 \tag{3.1}$$

where $\mathbf{r}_1$ and $\mathbf{r}_2$ are the position vectors of the centres of the two stars and $\omega = 2\pi/P$, P being the orbital period of the binary. In Fig. 3.1a some sections of the Roche equipotential surfaces are shown. Their shapes depend on the mass ratio of the two stars, q, while their scales depend on the binary separation, a. We distinguish, among others, an eight-shaped equipotential which circles both stars and is composed of two lobes, the Roche lobes, connected at the inner Lagrangian point L_1, which is a saddle point of unstable equilibrium for the configuration.
If one star, say M_1, fills the volume within its Roche lobe, its surface layers will pass through L_1, starting the accretion process. Following Eggleton (1983), we introduce the Roche lobe effective

[1] The approximation of circular orbits is a valid one. Tidal interactions tend to circularize orbits in a shorter time-scale than that driving the mass transfer process.

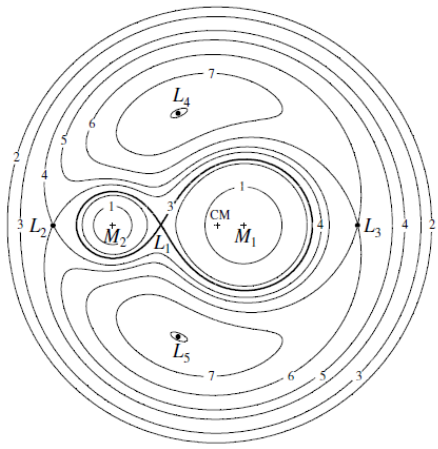

(a) Section across orbital plane of the Roche equipotentials $\phi_R = const$ for a binary system with mass ratio $q = M_2/M_1 = 0.25$. Also shown are the center of mass (CM) and Lagrange points $L_1 - L_5$. The equipotential surfaces are labelled 1-7 in order of increasing ϕ_R. (From Frank et al. 2002.)

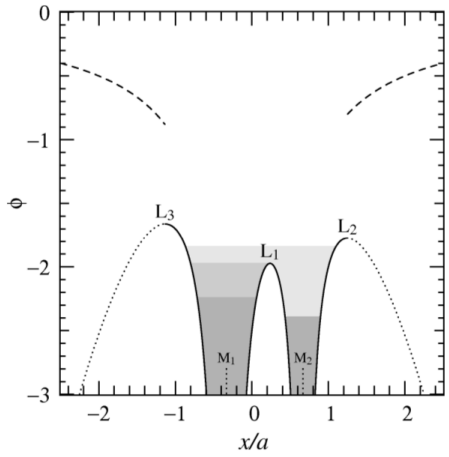

(b) Shape of the Roche potential (solid line) along the line connecting the two stars, for a binary with mass ratio $q = M_2/M_1 = 0.5$. The horizontal scale is in units of the semi-major axis a, and the potential ϕ is in units of $G(M_1 + M_2)/a$. Gray scales indicate the three possible stable binary configurations: detached (dark grey), semi-detached (intermediate grey) and contact (light gray). (From Pols 2011)

Figure 3.1: Roche equipotential surfaces (a) and Roche potential well (b) of two representative binary systems.

radius, R_L, as the radius of the sphere with the same volume as the Roche lobe of each star:

$$R_{L,j} \approx \frac{0.49 q_j^{2/3}}{0.6 q_j^{2/3} + \ln(1 + q_j^{1/3})} a \qquad j = 1, 2 \tag{3.2}$$

The onset of mass transfer can be identified comparing the radius of the star, R_j, to its corresponding Roche lobe effective radius. If $R_j < R_{L,j}$, the binary is detached (dark grey case of Fig. 3.1b): the two stars are inside their potential well and no mass transfer occurs. If one star overfills its Roche lobe, $R_j \geq R_{L,j}$, the matter in the vicinity of L_1 will no longer be in hydrostatic equilibrium, starting to feel the potential well of the other star. The binary is in the semi-detached phase, in which the stream of matter from the losing star accretes onto the other one through an accretion disc. This is the middle grey case in Fig. 3.1b. Finally, if both stars overfill their Roche lobe, the system is in contact, the light gray case in Fig. 3.1b.

ULXs are semi-detached binary systems undergoing mass transfer, therefore in the following pages we will refer to the *donor* (M_d) when talking about the losing mass star and the *accretor* (M_a) when talking about the receiving one. We also define $q = M_d/M_a$.

There are three ways in which the outer layers of a star can overfill its R_L: expansion driven by nuclear evolution, strong stellar winds or shrinkage of the orbit due to external perturbation or

orbital angular momentum losses.
The loss of orbital angular momentum is a key process in binary evolution. In the following, we will describe the main mechanisms which induce orbital angular momentum losses and their effect on RLOF.

3.1.1 Evolution of a binary: conservative and non conservative processes

The orbital angular momentum J_{orb} depends on the binary separation, a, and on the total of mass of the system (Frank et al., 2002):

$$J_{orb} = M_d M_a \left(\frac{Ga}{M_{tot}} \right)^{1/2}, \tag{3.3}$$

where $M_{tot} = M_d + M_a$. Let us consider the approximation of conservative mass transfer ($\dot{M}_d = -\dot{M}_a$, $\dot{M}_{tot} = 0$ and $\dot{J}_{orb} = 0$) to understand the first order effects of the mass ratio, q, on the evolution of the binary separation. The variation of the orbital separation is given by:

$$\frac{\dot{a}}{a} = \frac{2\dot{J}_{orb}}{J_{orb}} + \frac{2(-\dot{M}_d)}{M_d}(1-q), \tag{3.4}$$

where $q = M_d/M_a$. If $\dot{J}_{orb} = 0$ the binary expands ($\dot{a} > 0$) if the mass loosing donor star is less massive than the accretor ($q < 1$): the binary systems widens to conserve orbital angular momentum, because the accretor becomes more massive. Conversely, when mass is transferred from the more massive to the less massive ($q > 1$), conservative mass transfer leads to the shrinkage of the orbit. There are several non-conservative processes which can lead to non conservative mass transfer ($\dot{J} \neq 0$): the gravitational radiation, the spin-orbit coupling, the magnetic braking, and the mass loss from the donor or the accretor. In general, the resulting change in orbital angular momentum can be written:

$$\frac{\dot{J}_{orb}}{J_{orb}} = \frac{\dot{J}_{gw}}{J_{orb}} + \frac{\dot{J}_{ls}}{J_{orb}} + \frac{\dot{J}_{mb}}{J_{orb}} + \frac{\dot{J}_{ml}}{J_{orb}} \tag{3.5}$$

Gravitational radiation

The first term in Eq. 3.5 represents the angular momentum loss due to gravitational radiation (Landau and Lifshitz, 1951):

$$\frac{\dot{J}_{gw}}{J_{orb}} = -\frac{32G^5}{5c^5}\frac{M_d M_a M_T}{a^4} \qquad \mathrm{s}^{-1}, \tag{3.6}$$

where $M_T = M_d + M_a$ is the total mass. It is the dominant process for very narrow orbits ($P \leq 0.6$ days) leading to a shrinkage of the system. This effect was discovered in the Hulse-Taylor Pulsar (PSR 1913+16, Hulse and Taylor (1974)) which shows a decay of the orbital period in agreement with what predicted by gravitational radiation losses (Weisberg et al., 1981). In the recent years, the emission of gravitational radiation from binary mergers has been detected with the LIGO and VIRGO interferometers (see Abbott et al. (2016) and references therein).

Spin-orbit coupling

The second term in Eq. 3.5 refers to the exchange of angular momentum between the star and the orbit induced by the expansion or contraction of the star itself. It is an effective mechanism for orbital periods in range $2 < P_{orb} < 5$ days. For shorter periods the donor star does not expands or contract much, while for longer periods, or wider orbits, the tidal torque is negligible (see Tauris and van den Heuvel (2006) for details).

Magnetic braking

In isolated single stars, the ionized particles of the stellar wind escaping along the magnetic field lines threaded onto the surface of the star carry away angular momentum. The more intense the magnetic field, the larger is the angular momentum removed from the star. In a tidally coupled close binary not only the angular momentum of the mass-loosing mass star, but also the orbital angular momentum are effectively removed. (Verbunt and Zwaan, 1981; Rappaport et al., 1983). The change in orbital angular momentum due this process is:

$$\frac{\dot{J}_{mb}}{J_{orb}} \simeq -0.5 \cdot 10^{-28} f_{mb}^{-2} \frac{k^2 R^4}{a^5} \frac{G M_T^3}{M_d M_a} \qquad \mathrm{s}^{-1} \tag{3.7}$$

where R is the radius of the mass-losing star, k^2 is the gyration radius and f_{mb} is a constant of order unity.

Mass loss

The change in orbital angular momentum during RLOF is very sensitive to mass loss, which is usually the dominant term in Eq. 3.5. Mass leaving the system will remove orbital angular momentum in a way which depends on the region from which it is expelled. Following Soberman et al. (1997):

$$\frac{\dot{J}_{ml}}{J_{orb}} = \frac{\alpha + \beta q^2 + \delta\gamma(1+q)^2}{1+q} \frac{\dot{M}_d}{M_d} \tag{3.8}$$

where α is the fraction of the mass lost from the donor, β that expelled from the zones near the accretor, while δ that expelled from a circumbinary planar toroid with radius $r_t = \gamma^2 a$, if present.
The amount of mass dumped on the accretor, related to the efficiency of the accretion process, is:

$$\Delta M_a = -(1 - \alpha - \beta - \delta)\Delta M_d \tag{3.9}$$

3.1.2 Cases and stability of mass transfer

Following the theory of binary system evolution, we distinguish three cases of mass transfer, depending on the the evolutionary stage at which the donor overfills for the first time its Roche lobe: case A, B or C (see Fig. 3.2).
Case A occurs when the donor starts mass transfer on the Main Sequence (MS) and is burning hydrogen in the nucleus. In case B the mass transfer phase initiates when the donor is ascending the giant branch, during the hydrogen shell burning phase. Finally, in case C, the mass transfer

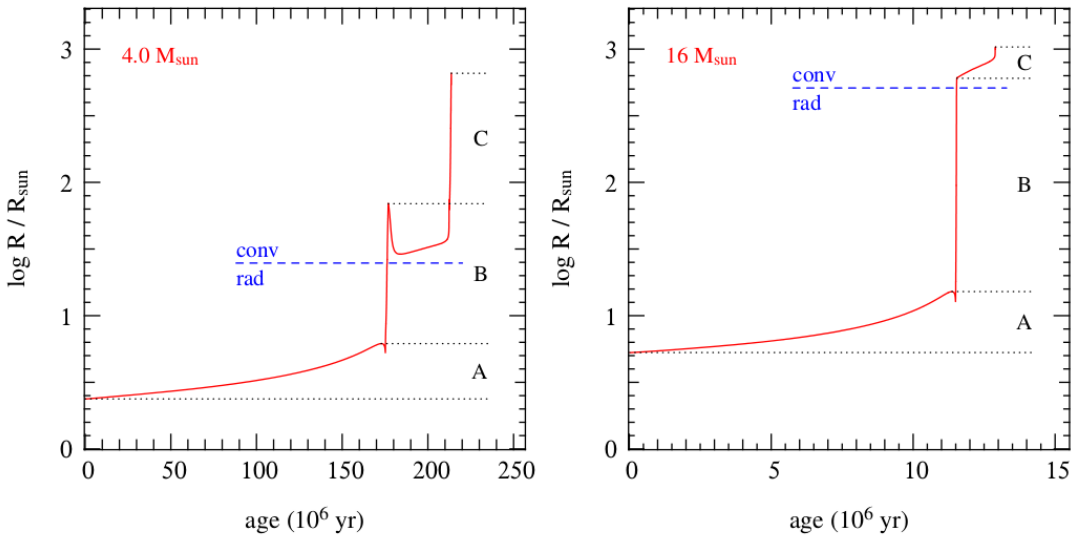

Figure 3.2: Variation of radii of stars (red lines) of $4M_\odot$ and $16M_\odot$ between the ZAMS (Zero Age Main Sequence) and either the end of the AGB (Asymptotic Giant Branch) (for a $4M_\odot$ star) or carbon burning (for a $16M_\odot$ star). The dotted lines indicate the radii at the ZAMS, the end of the MS, the He ignition and the final radius at the end of the computation. The dashed (blue) line shows the radius at which the stars develop a deep convective envelope on the giant branch (taken from Pols (2011).

starts during the helium nuclear burning phase.
Furthermore, we can distinguish between stable and unstable mass transfer depending on the relative response of both the donor radius and the Roche lobe radius to mass loss. Stable mass transfer requires that, after having lost a certain amount of mass, the donor star remains inside its Roche lobe (Soberman et al., 1997).
Therefore, in order to asses the stability of the process, one has to evaluate how the donor radius, R_d, and the Roche lobe radius, R_L, change as a function of mass loss, and how they compare one to another. In the linear stability analysis, this amounts to compare the exponents of the mass-radius relation for both the donor star and the Roche lobe radius, assuming a power-law dependence of radius on mass ($R \sim M^\zeta$):

$$\zeta_s = \left.\frac{\partial \ln R_d}{\partial \ln m_d}\right|_s \qquad \zeta_{eq} = \left.\frac{\partial \ln R_d}{\partial \ln m_d}\right|_{eq} \qquad \zeta_L = \left.\frac{\partial \ln R_L}{\partial \ln m_d}\right|_{bin,ev} \tag{3.10}$$

Here, ζ_s and ζ_{eq}, represent the exponent of the mass-radius relation determined from the requirement of restoring of the hydrostatic or thermal equilibrium, respectively. The stability criterion, ($R_d \lesssim R_L$) leads to to three cases of mass transfer (Pols, 2011):

- **stable mass transfer** ($\zeta_L \leq min(\zeta_s, \zeta_{eq})$): the donor remains inside its Roche lobe after restoring its hydrostatic and thermal equilibrium. The evolution of the mass transfer phase proceeds either on the nuclear timescale of the donor or in the timescale driven by angular momentum loss;

- **thermal-timescale mass transfer** ($\zeta_{eq} < \zeta_L \leq \zeta_s$): the mass transfer is dynamically stable. The mass loss rate, determined by the thermal timescale, has a maximum value

($\dot{M}_{max} \approx -M_d/\tau_{KH}$[2]);

- **dynamically unstable mass transfer** ($\zeta_L > \zeta_s$): the star does not remain inside its Roche lobe in response to mass loss. The mass transfer proceeds on a dynamical timescale and becomes dynamically unstable, driving the system towards a common envelope phase.

On the other hand, the response of the Roche radius to mass loss for conservative mass transfer ($\dot{J} = 0$) is given by the following equation (Frank et al., 2002):

$$\frac{\dot{R}_{L,d}}{R_{L,d}} = \frac{2\dot{J}}{J} + \frac{2(-\dot{M}_d)}{M_d}\left(\frac{5}{6} - q\right). \tag{3.11}$$

If $q > 5/6$ the Roche lobe shrinks after mass loss (eq. 3.11), on the contrary, if $q < 5/6$, the Roche lobe expands following mass loss. For non conservative mass transfer the expression is more complex. However, the removal of orbital angular momentum from the system will enhances the shrinkage of the system after mass loss.
It is possible to link the stability of mass transfer and the evolutionary phase of the donor. The response of the donor to mass loss depends on the structure of its envelope. A convective star expands, while a radiative star contracts in response to mass loss (Soberman et al. 1997 and references therein for more details). The evolution of a binary system then depends on the interplay of all these effects.
The variation of the radius of single stars with masses of 4 and 16 $M_\odot$ is shown as a function of time in Fig. 3.2 (solid red line). The radius at which their envelopes switches from being radiative to being convective is also indicated (dashed blue line). An intermediate mass donor ($2.5 \lesssim M \lesssim 8M_\odot$) will start to expand in response to mass loss while ascending the RGB, during the hydrogen shell burning phase. A massive donor will instead maintain its radial envelope up to the final stages of the RGB, becoming convective just before the He ignition in its nucleus.

Case A mass transfer

Systems undergoing conservative case A mass transfer and $q > 1$ at the beginning of the evolution evolve as depicted in Fig. 3.3. The upper left panel describes the variation of the key radii of the problem with the donor mass. From point A (ZAMS) to point B (where there is the onset of mass transfer) the donor expands on a nuclear timescale. From points B to C the star is not in thermal equilibrium and enters a phase of rapid mass transfer on a thermal timescale. The mass transfer rate is very high during this phase (upper right panel of Fig. 3.3), and the donor loses a large fraction of its mass leading to a reversal of the mass ratio. From point C up to point D the donor star gains again thermal equilibrium and the mass transfer proceeds on the longer nuclear timescale. At point D the system detaches. Afterwards, during the H-shell burning phase the donor expands again, and the mass transfer proceeds on the faster (but stable) expansion timescale. During this phase the star is crossing the Herzprung gap. Fig. 3.3 shows also the H-R diagram for both the donor star (red line) and the accretor (blue line). They are

[2]The Kelvin-Helmholtz time scale is the time scale on which a star reacts when there is disequilibrium between energy loss and energy production. It is defined as the radio between the thermal energy content of the star E_{th} and the luminosity L: $\tau_{KH} = \frac{E_{th}}{L} \approx \frac{GM^2}{2RL} \approx 1.5 \cdot 10^7 \left(\frac{M}{M_\odot}\right)^2 \frac{R_\odot}{R} \frac{L_\odot}{L}$ yr

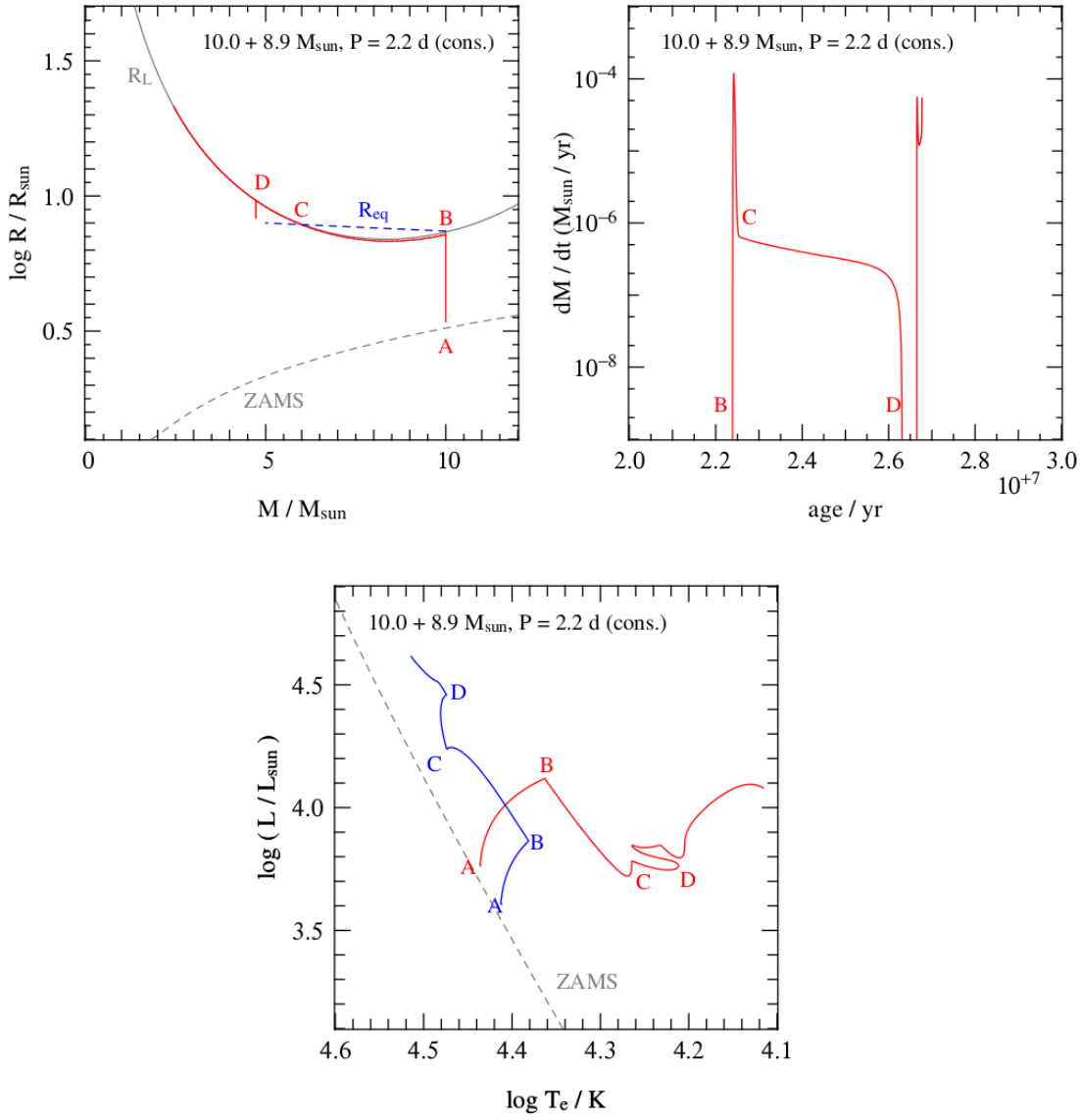

Figure 3.3: Case A mass transfer for a binary with a $10.0M_\odot$ donor and a $8.9M_\odot$ accretor. The upper left panel shows the variation of the donor radius (red), the Roche lobe radius R_L (solid black line) and the equilibrium radius R_{eq} (dashed blue line) below which the star is not in thermal equilibrium. From point B to C the donor is out of thermal equilibrium and the mass transfer proceeds on the fast thermal timescale with high values of the mass transfer rate, as shown in the upper right panel. Thereafter, the evolution proceeds on a nuclear timescale, with lower values of mass the transfer rates. The evolutionary tracks on the H-R diagram for the donor (red line) and the accretor (blue line) are shown in the lower panel. Taken from Pols (2011)

different from that of a single star with the same initial mass. Initially, from points B to C, both stars are out of thermal equilibrium. During this phase the donor becomes less luminous while the luminosity of the accretor increases. When the mass transfer occurs on a nuclear timescale, thermal equilibrium is restored and the stars occupy the H-R diagram of single stars but with

different masses.

Case B mass transfer

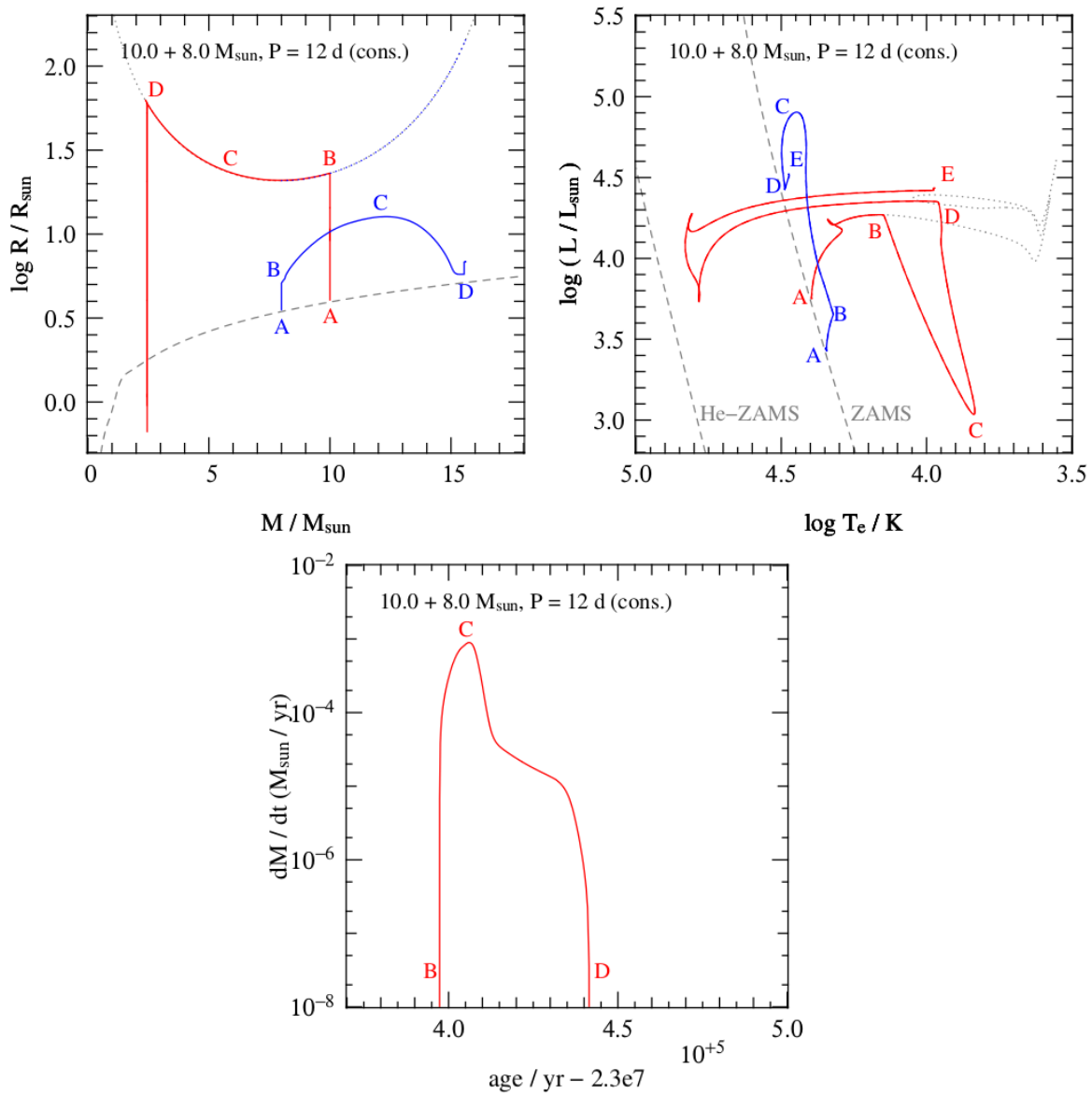

Figure 3.4: Same as Fig. 3.3 but for case B mass transfer. The mass transfer episode happens on a short timescale, and the long-nuclear timescale phase, tipical of case A mass transfer is here absent. Taken from Pols (2011)

The evolution of systems undergoing conservative case B mass transfer, with the same masses as above, is depicted in Fig. 3.4. When RLOF sets in, the donor is crossing the Herzprung gap out of thermal equilibrium. Therefore the mass transfer proceeds at high rates. When He-ignition occurs in the core, the star contracts and the system detaches. On the H-R diagram we see that the donor decreases its luminosity from points B to C, where it reaches the minimum

luminosity, corresponding to the maximum value of mass transfer rate.

Case C mass transfer

Case C mass transfer occurs when the donor fills its Roche lobe for the first time during the late stages of its evolution, after exhaustion of helium in the core. It is expected to be short and dynamically unstable (Pols, 2011), leading possibly to a common envelope phase. Since the aim of this Thesis is to consider RLOF systems relevant for persistent ULXs, we will not consider case C mass transfer further here.
The work presented in this thesis will consider systems undergoing case A mass transfer.

3.2 Accretion discs

An accretion disc consists mainly of hydrogen gas (sometimes highly ionized and sometimes in molecular forms), although helium and other elements are presented in cosmic abundances. As we will discuss later, a standard accretion disc is flat (geometrically thin) and opaque (optically thick). The gas in the disc is rotating around the central object with different velocities at different radii. The rotational velocity is very close to Keplerian. Frictional viscosity acts on the accreting matter: the gas heats up and radiates electromagnetic radiation.

Efficiency

During accretion, gravitational potential energy is ultimately converted into radiation. If matter falls onto a star in free-fall from infinity, it acquires kinetic energy as its gravitational potential decreases. Considering a proton falling in from infinity, we can write

$$\frac{1}{2}m_p v_{ff}^2 = \frac{GMm_p}{r}. \tag{3.12}$$

When the mass reaches the surface of the star at $r = R$, it is rapidly decelerated and, assuming all the matter accumulates on the surface of the star, all kinetic energy is transformed into heat and/or radiated away. If the rate at which mass is accreted onto the star is $\dot{m}$, the rate at which kinetic energy is dissipated at the surface of the star is $\frac{1}{2}\dot{m}v_{ff}^2$ and hence the luminosity of the source is

$$L = \frac{1}{2}\dot{m}v_{ff}^2 = \frac{GM\dot{m}}{R}. \tag{3.13}$$

Using the Schwarzschild radius, eq. 3.13 can be written

$$L = \frac{1}{2}\dot{m}c^2\left(\frac{r_s}{R}\right). \tag{3.14}$$

or:

$$L = \eta\dot{m}c^2 \tag{3.15}$$

where $\eta = r_s/2R$ is the efficiency of conversion of the rest-mass energy of the accreted matter into heat and radiation. The conversion is more efficient if the accreting object is more compact. In case of a Schwarzschild black hole we have $\eta \sim 0.06$.

Eddington Luminosity

The Eddington luminosity is the maximum luminosity that can be emitted by an accreting object in spherical symmetry and under stationary conditions. If luminosity is higher, radiation pressure would blow away the infalling matter. This limit is obtained setting the inward force of gravity equal to the outward force of radiation. It is also assumed that the infalling matter is fully ionised and that the radiation force is caused by Thomson scattering of photons on electrons in the plasma. Consider the forces acting on an electron-proton pair at distance r from the source. The inward gravitational force is:

$$F_g = \frac{GM}{r^2}(m_p + m_e) \approx \frac{GMm_p}{r^2}. \tag{3.16}$$

The radiation force acts upon the electron but, because the plasma must remain neutral, this force is communicated to the protons by the electrostatic forces acting between the protons and the electrons. Each photon gives up a momentum $p = h\nu/c$ to the electron in each collision. Therefore, the force f_r acting on the electron is the momentum communicated to it per second by the incident flux density of photons N_{ph}. Thus, $f_r = \sigma_T N_{ph} p$, where $\sigma_T = 6.653 \cdot 10^{-25} cm^2$ is the Thomson cross-section. The flux density of the photons at distance r from the source is $N_{ph} = L/4\pi r^2 h\nu$, where L is the luminosity of the source, and so the outward force on the electron is $f_r = \sigma_T L/(4\pi r^2 c)$. Setting this force equal to the inward gravitational force, we find :

$$\frac{\sigma_T L}{4\pi r^2 c} = \frac{GMm_p}{r^2}$$

from which it is straightforward to derive the Eddington luminosity:

$$L_{Edd} = \frac{4\pi GMm_p c}{\sigma_T}. \tag{3.17}$$

We emphasize again that it is the maximum luminosity a spherically symmetric source of mass M can emit in a steady state. This limiting luminosity is independent of the radius r and depends only upon the mass M of the accreting object. Using the Schwarzschild radius, the expression for the Eddington luminosity can be rewritten as follows:

$$L_{Edd} = \frac{2\pi r_s m_p c^3}{\sigma_T} = 1.3 \cdot 10^{38} \left(\frac{M}{M_\odot}\right) ergs^{-1} \tag{3.18}$$

From eq. 3.15, it follows that there exists also a limit on the mass transfer rate that can sustain the Eddington luminosity:

$$\dot{M}_{Edd} \equiv \frac{L_{Edd}}{c^2} \simeq 1.3 \cdot 10^{17} \left(\frac{M}{M_\odot}\right) gs^{-1}. \tag{3.19}$$

Accretion discs Models

In the present analysis we will consider two models of accretion discs: the standard Shakura-Sunyaev (1973) model, and the advection-dominated slim disc model (Abramowicz et al. 1988). These two models assume different physical conditions. In the standard model emission processes are radiatively efficient. All heat generated by viscosity at a given radius is immediately radiated away: viscous heating is balanced by radiative cooling locally. This configuration is valid if the mass transfer rate is not very high, so that the radial pressure and velocity gradients are very small. If mass transfer rate is very high (above Eddington), the radial velocity is large. We have to consider the radial pressure and velocity gradients and the fact that viscously-generated heat is not efficiently radiated away. Advection, where internal energy and photons are transported inward by the motion of the gas, becomes important.

3.2.1 Standard disc Model

Let us consider a disc in the thin approximation model: the disc is confined closely to the orbital plane and it is considered as a two-dimensional gas flow. Viscosity is assumed to remove energy

and angular momentum from the plasma. We analyse the problem in a cylindrical polar frame of reference (R, ϕ, z) assuming the matter moves in circular Keplerian orbits with angular velocity

$$\Omega = \Omega_K(R) = \left(\frac{GM_1}{R_1^3}\right)^{1/2} \tag{3.20}$$

and circular velocity

$$v_\phi = R\Omega_K(R). \tag{3.21}$$

Other quantities of interest for the radial structure study are the *radial velocity* v_R and the *surface density* Σ(R,t):

$$\Sigma(R,t) = \int \rho \; dz. \tag{3.22}$$

All variables are averaged in the vertical direction. The formation of the disc is well described by a diffusion equation in the surface density Σ. This is obtained from the mass and angular momentum conservation equations for the plasma combined with the definition of viscous torque. After integration in the vertical direction, along which hydrostatic equilibrium is assumed, for the mass conservation we have

$$R\frac{\partial \Sigma}{\partial t} + \frac{\partial}{\partial R}(R\Sigma v_R) = 0 \tag{3.23}$$

while the angular momentum conservation is

$$R\frac{\partial}{\partial t}(\Sigma R^2\Omega) + \frac{\partial}{\partial R}(R\Sigma v_R R^2\Omega) = \frac{1}{2\pi}\frac{\partial G}{\partial R} \tag{3.24}$$

and the viscous torque is given by: (see Frank et al. 2002):

$$G(R,t) = 2\pi R\nu\Sigma R^2\Omega' \tag{3.25}$$

where ν is the coefficient of kinematic viscosity. Combining these equations we obtain a diffusion equation for the surface density:

$$\frac{\partial \Sigma}{\partial t} = \frac{3}{R}\frac{\partial}{\partial R}\left\{R^{1/2}\frac{\partial}{\partial R}[\nu\Sigma R^{1/2}]\right\}. \tag{3.26}$$

If we assume for simplicity $\nu = const$, the solution of eq. 3.26 has the form (Frank et al. 2002):

$$\Sigma(x,\tau) = \frac{m_{ring}}{2\pi R_0}\tau^{-1}x^{-1/4}\exp\left\{-\frac{(1-x^2)}{\tau}\right\}I_{1/4}(2x/\tau) \tag{3.27}$$

where $x = R/R_0$, $\tau = 12\nu t R_0^{-2}$, $I_{1/4}$ is a modified Bessel function and the initial condition is a ring of mass m at radius $R = R_0$. In figure 3.5 we show $\Sigma(R,t)$ at different times τ. Viscosity spreads the original ring in radius on a typical timescale

$$t_{visc} \sim \frac{R^2}{\nu} \tag{3.28}$$

where t_{visc}, which is of the order of days or weeks, is the viscous or radial drift timescale, since it gives an estimate of the timescale for a disc annulus to move a radial distance R. From the diffusion equation it is easy to see also that the outer parts of the disc move outwards taking away angular momentum, while the inner parts of the disc move inwards.

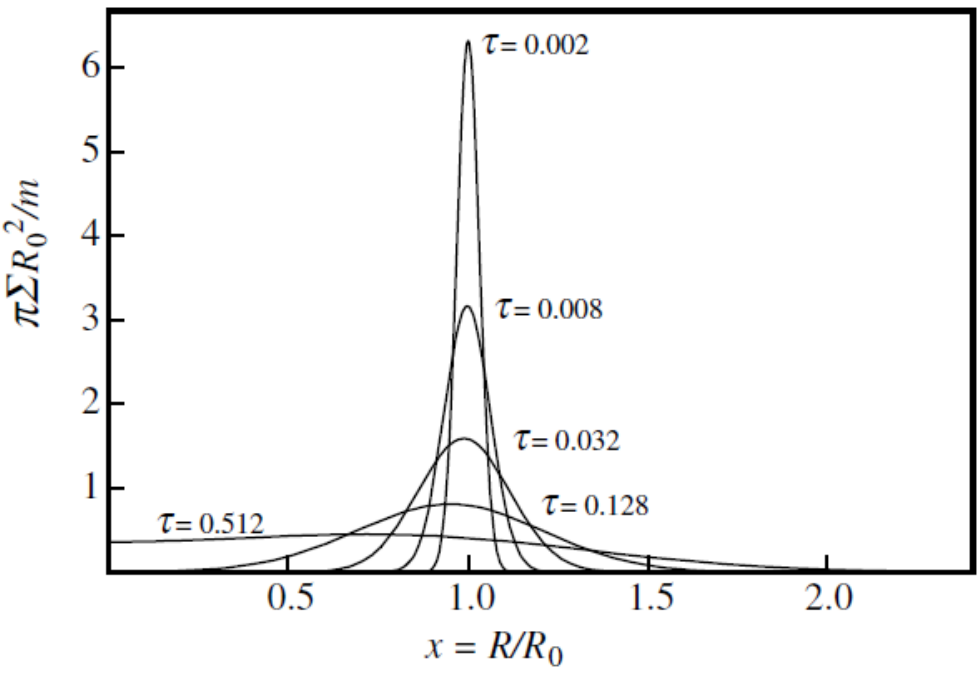

Figure 3.5: A ring of matter of mass m placed in a Kepler orbit at $R = R_0$ spreads out under the action of viscous torques. The surface density Σ is shown as a function of $x = R/R_0$ and the dimensionless time variable $\tau = 12\nu t R_0^{-2}$, with ν the constant kinemtic viscosity (Frank et al. 2002).

Steady thin disc

When the mass transfer rate changes on timescales longer than t_{visc} a steady thin disc forms. The structure of such a disc is obtained setting $\partial/\partial t = 0$ in the mass conservation and momentum equations 3.23 and 3.24. From the mass conservation (eq. 3.23), we get

$$R\Sigma v_R = const \tag{3.29}$$

This implies that the accretion rate:

$$\dot{M} = 2\pi R\Sigma(-v_R) \tag{3.30}$$

is constant.

From the angular momentum equation (3.24) we obtain the following relation for the surface density (see Frank et al. 2002):

$$\nu\Sigma = \frac{\dot{M}}{3\pi}\left[1 - \left(\frac{R_{in}}{R}\right)^{1/2}\right] \tag{3.31}$$

where R_{in} is the inner radius where the disc terminates. With this expression, the viscous dissipation per unit disc surface area, $D(R)$, becomes (see Frank et al. 2002 for details):

$$D(R) = \frac{3GM\dot{M}}{8\pi R^3}\left[1 - \left(\frac{R_{in}}{R}\right)^{1/2}\right] \tag{3.32}$$

Assuming that all the viscously dissipated energy is radiated locally at radius R, the luminosity emitted by the disc between R_1 and R_2 is:

$$L(R_1, R_2) = 2 \int_{R_1}^{R_2} D(R) 2\pi R \, dR \tag{3.33}$$

where the factor 2 accounts for the two sides of the disc. Then, we have:

$$L(R_1, R_2) = \frac{3GM\dot{M}}{2} \int_{R_1}^{R_2} \left[1 - \left(\frac{R_{in}}{R} \right) \right] \frac{dR}{R^2}. \tag{3.34}$$

Letting $R_1 = R_{in}$ and $R_2 \to \infty$, we obtain the luminosity of the whole disc:

$$L_{disc} = \frac{GM\dot{M}}{2R_{in}} \tag{3.35}$$

Assuming Local Thermodynamic Equilibrium (LTE) along the vertical direction, the flux of radiant energy along the vertical direction is given by

$$F(z) = \frac{-16\sigma T^3}{3k_R \rho} \frac{\partial T}{\partial z} \tag{3.36}$$

where k_R is the Rossleand mean opacity. In the stated assumptions, the energy-balance equation is then:

$$\frac{\partial F}{\partial z} = Q^+$$

where Q^+ is the volume rate of energy production by viscous dissipation. Integrating the previous equations along z, we have

$$F(H) - F(0) = \int_0^H Q^+(z) \, dz = D(R) \tag{3.37}$$

as the total dissipation rate through half of the disc must be equal to the dissipation rate per unit face area $D(R)$. Averaging eq. 3.36 along z and with the assumption $T_C^4 \gg T^4(H)$, where T_C^4 is the central temperature, we obtain:

$$\frac{4\sigma}{3\tau} T_c^4 = D(R) \tag{3.38}$$

where $\tau = \rho H k_R$ is the optical depth. The thin disc is finally described by a set of eight equation which must be solved. Once these equations are solved it is possible to obtain non only the disc structure but also the radial drift velocity of the plasma falling inward.

An important consequence of the optical thickness and LTE in the z-direction is the fact that the accretion disc can be considered as of a series of rings radiating as black bodies. Every annulus has a temperature $T(R)$ obtained by setting the dissipation rate $D(R)$ per unit face area equal to the local blackbody flux:

$$\sigma T^4(R) = D(R). \tag{3.39}$$

Using eq. 3.32, we get

$$T(R) = \left\{ \frac{3GM\dot{M}}{8\pi R^3 \sigma} \left[1 - \left(\frac{R_{in}}{R} \right)^{1/2} \right] \right\}^{1/4} \tag{3.40}$$

which gives the disc radial temperature profile. For large radii, $R \gg R_{in}$ eq. 3.40 simplifies to:

$$T = T_* \left(\frac{R}{R_*}\right)^{-3/4} \tag{3.41}$$

where $T_* = \frac{3GM\dot{M}}{8\pi R^3 \sigma}$. As every ring is considered to emit as a black body, we can approximate the spectrum emitted by each element of area of the disc, neglecting the effects of the atmosphere, as

$$I_\nu = B_\nu[T(R)] = \frac{2h\nu^3}{c^2(e^{h\nu/kT(R)} - 1)}. \tag{3.42}$$

Now it is possible to determine the spectrum seen by an observer at distance D who looks at the binary system with an inclination i:

$$F_\nu = \frac{2\pi \cos i}{D^2} \int_{R_*}^{R_{out}} I_\nu R \; . \tag{3.43}$$

Eq. 3.43 then becomes:

$$F_\nu = \frac{4\pi h \cos i \nu^3}{c^2 D^2} \int_{R_*}^{R_{out}} \frac{R}{e^{h\nu/kT(R)} - 1} \, dR. \tag{3.44}$$

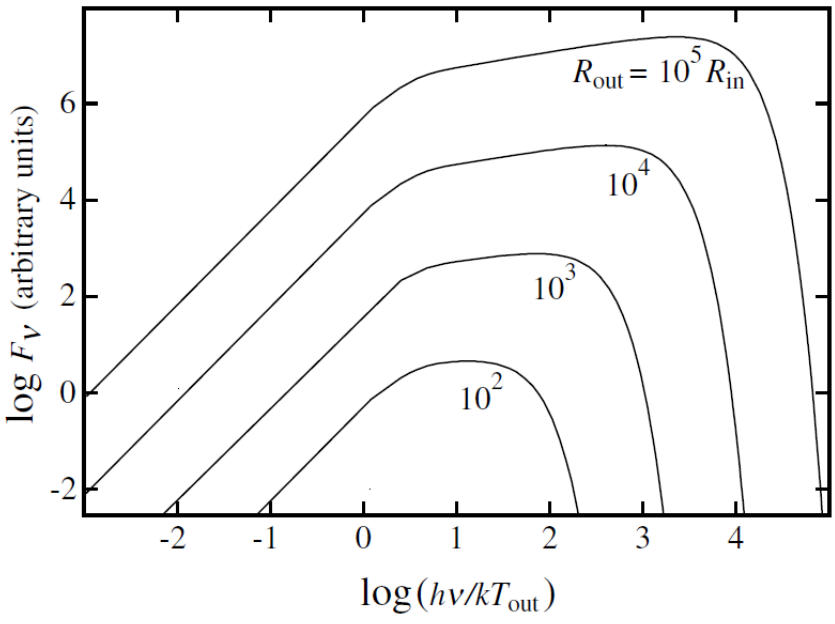

Figure 3.6: The continuum spectrum F_ν of a steady optically thick accretion disc radiating locally as a blackbody, for discs with different ratios R_{out}/R_{in}. The frequency is normalized to kT_{out}/h where $T_{out} = T(R_{out})$. These spectra illustrate the relative extent of the 'ν^{1-3}' continuum for discs with differing temperature ranges. In particular discs around white dwarfs with $R_{out} \sim 10^2 R_{in}$ do not possess an obvious power-law character (Frank et al. 2002).

In figure 3.6 the continuum spectrum of a steady optically thin disc is shown. As can be seen, at low frequencies, $\nu \ll kT(R_{out})/h$, $F_\nu \propto \nu^2$, while for high frequencies, $\nu \gg kT(R_{in})/h$, the spectrum decays exponential as $\nu^3 e^{-h\nu/kT}$. At intermediate frequencies $F_\nu \propto \nu^{1/3}$: this 'flat part' is considered to be the characteristic imprint of a standard disc spectrum.

Standard model: steady α-discs

The simpler model of a steady disc was proposed by Shakura and Sunyaev (1973) and is associated with their names. The physical origin of the viscosity mechanism acting in astrophysical flows has long been unknown. For this reason, Shakura and Sunyaev proposed to parametrize the viscosity coefficient ν using the the following prescription:

$$\nu = \alpha c_s H, \tag{3.45}$$

where α is a parameter assumed to be < 1 and c_s and H provide an estimate of the velocity and length scales of the physical mechanism that originates the viscosity. Although such a mechanism is now understood (Balbus and Hawley, 1991), the α-prescription is still largely used. The Rosseland mean opacity is approximated with Kramers' law:

$$k_R = 5 \times 10^{24} \rho T_c^{-7/2} cm^{-2} g. \tag{3.46}$$

With these assumption the full system of equations that describes the disc structure can be solved algebraically. The solution, expressed in terms of $R_{10} = R/(10^{10} cm)$, $m_1 = M/M_\odot$ and $\dot{M}_{16} = \dot{M}/(10^{16} g s^{-1})$, is:

$$\Sigma = 5.2 \alpha^{-4/5} \dot{M}_{16}^{7/10} m_1^{1/4} R_{10}^{-3/4} f^{4/15} g cm^{-2} \tag{3.47}$$

$$H = 1.7 \times 10^8 \alpha^{-1/10} \dot{M}_{16}^{3/20} m_1 - 3/8 R_{10}^{9/8} f^{3/5} cm \tag{3.48}$$

$$\rho = 3.1 \times 10^{-8} \alpha^{-7/10} \dot{M}_{16}^{11/20} m_1^{5/8} R_{10}^{-15/8} f^{11/5} g cm^{-3} \tag{3.49}$$

$$T_c = 1.4 \times 10^4 \alpha^{-1/5} \dot{M}_{16}^{3/10} m_1^{1/4} R_{10}^{-3/4} f^{6/5} K \tag{3.50}$$

$$\tau = 190 \alpha^{-4/5} \dot{M}_{16}^{-1/5} f^{4/5} \tag{3.51}$$

$$\nu = 1.8 \times 10^{14} \alpha^{4/5} \dot{M}_{16}^{3/10} m_1^{-1/4} R_{10}^{3/4} f^{6/5} cm^2 s^{-1} \tag{3.52}$$

$$v_R = 2.7 \times 10^4 \alpha^{4/5} \tag{3.53}$$

with

$$f = \left[1 - \left(\frac{R_{in}}{R} \right)^{1/2} \right]^{1/4}.$$

It is important to note that the α- parameter does not enter any of the expressions for the disc quantities with a high power. This means that these quantities are not very sensitive to the actual value of α and accordingly to the viscosity itself. Another interesting fact about this type of discs is that they are geometrically thin, being the H/R ratio

$$H/R = 1.7 \times 10^{-2} \alpha^{-1/10} \dot{M}_{16}^{3/20} m_1^{-3/8} R_{10}^{1/8} f^{3/5}. \tag{3.54}$$

Moreover, from the expression for τ eq. 3.51, we see that the disc is optically thick for any reasonable accretion rate.
The α-prescription introduced in the standard model is merely a parametrization. α can in general be function of $\dot{M}$, M, R, and z. The z-dependence can be ignored if we interpret the α value as 'vertically averaged' because the disc structure is supposed to be uniform in the vertical direction. The real importance of the solutions presented above is that for $\alpha \leq 1$ we get believable orders of magnitude for the disc quantities, and this is reinforced by the comparatively weak dependence on α noted above.

3.2.2 Irradiated discs

When calculating the spectrum emitted by the disc, we must consider the effects of self-irradiation. Radiation emitted from the inner regions can hit the outer regions of the disc. Here we present the classical treatment as described in "*Accretion Power in astrophysics*" (Frank et al., 2002). Let us suppose a geometrically thin and optically thick disc, irradiated by a central source. If the central source can be regarded as a point, its total radiative flux at disc radius r is simply

$$F = \frac{L_{irr}}{4\pi R^2} \tag{3.55}$$

where L_{irr} is the irradiating luminosity. The flux crossing the disc surface at this point is (see Fig. 3.7):

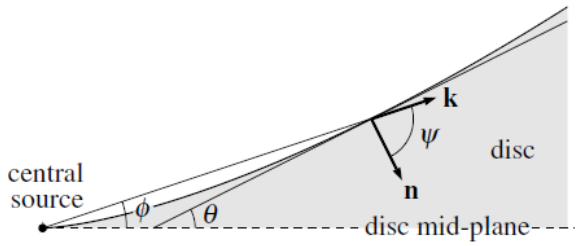

Figure 3.7: Irradiated disc geometry. The unit vector $\boldsymbol{k}$ *indicates the direction of propagation of the radiation incident on the disc and* $\boldsymbol{n}$ *is the local inward-directed normal vector.*

$$Q_{irr} = \frac{L_{irr}}{4\pi R^2}(1 - A)\cos\psi \tag{3.56}$$

where A is the albedo, namely the effective fraction of incident radiation scattered from the surface without absorption. ψ is the angle between the local inward-directed disc normal and the direction of the incident radiation. From the geometry of the disc surface (see Fig. 3.7), we see that

$$\psi = \frac{\pi}{2} - \theta + \phi$$

where

$$\tan\theta = \frac{dH}{dR}$$

and

$$\tan\phi = \frac{H}{R}$$

with H the local scale height. Since dH/dR, H/R are both $\ll 1$ for a thin disc we have

$$\cos\psi = \sin(\theta - \phi) = \cos\theta\cos\phi[\tan\theta - \tan\phi] \simeq \frac{dH}{dR} - \frac{H}{R}.$$

Thus, the heating rate can be expressed as

$$Q_{irr} = (1 - A)\frac{L_{irr}}{4\pi R^2}\left(\frac{dH}{dR} - \frac{H}{R}\right). \tag{3.57}$$

In addition to this irradiation heating, there is also the classical viscous heating inside the disc. Once the heating rate due to irradiation is known, we can easily obtain the structure and spectrum of the irradiated accretion discs. We assume that:

- the disc is steady and axisymmetric
- the self-gravity of the disc gas can be ignored
- as assumed before, since the disc is geometrically thin, all physical quantities are integrated along the vertical direction
- the disc is optically thick and heated by the X-ray source.

Under these assumptions, the basic equations governing the radial structure of the disc become the same as those of standard discs, except for the energy equation. That is to say, the continuity equation, the angular momentum conservation, the hydrostatic equilibrium equation, and the equation of state. The energy balance equation, becomes:

$$\frac{3GM\dot{M}}{4\pi R^3} + Q_{irr} = 2\sigma T^4 \tag{3.58}$$

where Q_{irr} is given by eq. 3.57. The standard theory of irradiated disc, divides the discs itself into two parts: the inner disc, where the viscous heating is dominant, and the outer disc, where self-irradiation is dominant.

Irradiation in the inner discs

We note that, in General Relativity, in the inner disc the self-irradiation caused by gravitational bending can become important especially for Kerr black holes. This effect is not considered here. In the inner part of the disc, where the viscous heating is dominant, the temperature and the disc height are (Sanbuichi et al., 1993):

$$\begin{aligned} T &= 1.29 \cdot 10^7 M_1^{-1/4}\dot{M}_{19}^{1/4} r_7^{-3/4} K \\ \frac{H}{R} &= 5.69 \cdot 10^{-3} M_1^{-3/8}\dot{M}_{19}^{1/8} r_7^{1/8} \end{aligned} \tag{3.59}$$

where $M_1 = M/10M_\odot$ and $\dot{M}_{19} = \dot{M}/10^{19}$ gs^{-1} and $r_7 = R/10^7$ cm.

Outer self-irradiated discs

For what concerns the outer disc, where $H \gg R$, the energy equation becomes

$$(1-A)\frac{L_{irr}}{4\pi R^2}\left(\frac{dH}{dR}-\frac{H}{R}\right)=2\sigma T^4 \tag{3.60}$$

In this case the radial profile of temperature and disc height are (Sanbuichi et al., 1993):

$$\begin{aligned} T &= 8.56\cdot 10^5 (1-A)^{2/7}\beta_{0.18}^{2/7}M_1^{-1/7}\dot{M}_{19}^{2/7}r_7^{-3/7}K \\ \frac{H}{R} &= 1.47\cdot 10^{-3}(1-A)^{1/7}\beta_{0.18}^{1/7}M_1^{-4/7}\dot{M}_{19}^{1/7}r_7^{2/7} \end{aligned} \tag{3.61}$$

where $\beta_{0.18} = \beta/0.18$, and β the ratio between the irradiated luminosity and the total disc luminosity.

Spectrum of Irradiated discs

Now that we know the temperature as a function of radius, we can compute the spectrum of a self-irradiated disc around a Schwarzschild black hole. Following Sanbuichi et al. (1993), the spectrum has been calculated under the Newtonian approximation, since we are mainly interested in the low energy part of the spectrum, emitted by the outer part of the disc. The surface temperature of the inner disc is given by equation 3.59 for $R_{in} \leq R \leq R_B$ and equation 3.60 for $R_B \leq R \leq R_{out}$, where R_{in} is the inner radius, R_{out} the outer radius and R_B the radius of the boundary annulus, at which self-irradiation is assumed to change regime (see Sanbuichi et al. 1993). The observed flux S_ν is calculated by integrating the specific intensity I_ν of the disc over its surface. It is assumed that the surface of the disc radiates blackbody radiation B_ν. Inserting in the expression for B_ν, the temperature of the disc and that of the irradiated part, Sanbuichi et al. (1993) obtained the emergent spectra, for the following values of the parameters involved:

- 1-A $= 1/2$
- $M = 10M_\odot$
- $\dot{M} = 10^{19} g s^{-1}$
- $R_{in} = 3r_s$.

The spectrum is shown in fig. 3.8. It is typically double peaked. At high frequencies, where radiation from the inner viscous disc is dominant, the observed flux varies as $S_\nu \propto \nu^{1/3}$. On the other hand, in the low frequency part of the spectrum, where irradiation is dominant, it varies as $S_\nu \propto \nu^{-5/3}$. In general the low-frequency part of the spectrum is modified by the presence of irradiation. The double-peaked structure is more visible in extended discs. It should be noted that if the X- rays are sufficiently hard, they may penetrate all the way down to the equatorial plane of the disc and the assumption that the disc is vertically isothermal is valid. If, however, X-rays are soft, they may be absorbed mainly at the surface of the disc through photoionization, and the internal structure of the disc may be different from the isothermal model. In such a case, the spectrum may be different from that presented here.

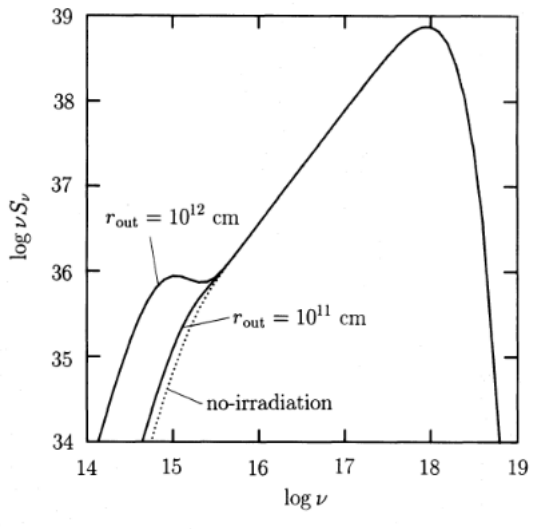

Figure 3.8: Emergent spectra of the self-irradiated disc around a Schwarzschild black hole (Sanbuichi et al., 1993). The low-fequency part of the spectrum is modified by the presence of self-irradiation if the disc is sufficient large. The influence of self-irradiationon the spectrum is important at optical wavelengths.

3.2.3 Advection Dominated discs

In slim discs the radial inflow velocity and the horizontal pressure gradient are important in the momentum equation. The radial inflow velocity of the gas is comparable to the rotational velocity. This model was first proposed by Abramowicz et al. (1988), who studied the effects of moderately super-Eddington accretion rates. The consequence of horizontal pressure and entropy gradients is the presence of a strong horizontal heat flux, which changes the energy balance in the disc. This horizontal heat flux is often called *advective cooling*. The gas does not have enough time to release all viscous heat produced at a given annulus through the emission of photons because the inward radial motion is too fast. As a consequence, a large fraction of the accretion energy is advected inward towards the BH and the total luminosity emitted is no longer proportional to the accretion rate, as in the standard model, but tends asymptotically to 10 L_{Edd}, as shown in fig. 3.9.

Self-similar solution

From now on we refer to the model proposed by Narayan & Yi (1994), who computed self similar solutions for slim discs, and first coined the definition of *advection-dominated* disc: a flow where the bulk of the liberated thermal energy is carried in by the accreting gas as entropy rather than being radiated. They construct a class of self-similar solutions which we will adopt in our model. It should be noted that the advection-dominated solutions of Narayan and Yi (1994) refer to general physical conditions of inefficient cooling in the gas, in particular at very low densities and at very low densities and significantly sub-Eddington mass transfer rates while here we refer only to the case when $\dot{M} \gg \dot{M}_{Edd}$. Self-similar solutions for advection-dominated accretion discs are calculated in the following assumptions:

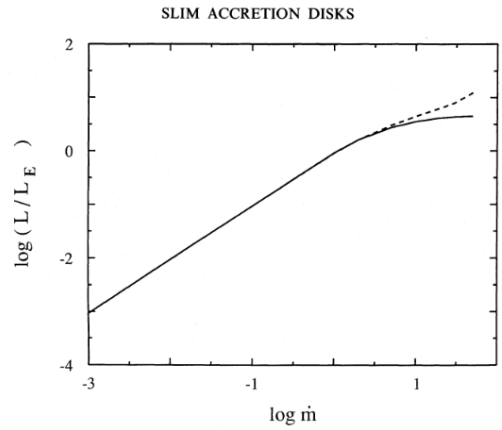

Figure 3.9: The total luminosity for slim disc models (solid line) as a function of the accretion rate $\dot{m}$ (both in Eddington unit). The dashed line represent the rate of energy generation by viscous stresses. Models computed with central black hole mass $M = 10M_{\odot}$. From Abramowicz et al. (1988).

- steady axisymmetric flow
- Keplerian angular velocity $\Omega_K(R) = \left(\frac{GM}{R^3}\right)^{1/2}$

The expression for the shear viscosity is the same as in the standard model: $\nu = \alpha c_s H$. In case of slim, advection-dominated disc, the energy equation becomes:

$$\Sigma v T \frac{dS}{dR} = Q^+ - Q^-. \tag{3.62}$$

The left-hand side represents advection of entropy S, while the right hand side gives the difference between the energy input per unit area due to viscous dissipation, Q^+, and the energy loss through radiative cooling, Q^-. In the assumption that the ratio of the advected and viscously dissipated energy does not depend on radius, Narayan and Yi ('94) derived power-law self-similar solutions for the structure of the disc. They take the form (see also Narayan and Yi 1988):

$$\rho \propto R^{-3/2}, v \propto R^{-1/2}, \Omega \propto R^{-3/2}, c_s^2 \propto R^{-1} \tag{3.63}$$

where v and Ω are significant fractions of v_k and Ω_k.

Properties of self-similar solutions

The self-similar solutions for advection-dominated discs have some interesting properties. First, the sound speed is comparable to the Keplerian speed. This has two consequences: the temperature of the accreting gas is nearly virial, and the disc vertical thickness is comparable to the radial coordinate. Furthermore, the radial velocity is much larger than in standard disc and the angular velocity is slightly sub-Keplerian. Finally, the radiative efficiency is much less than that of a standard disc.

Chapter 4

Modelling optical emission of Ultra-luminous X-ray sources accreting above the Eddington limit

This chapter is taken from Ambrosi and Zampieri (2018): 'Modelling optical emission of Ultra-luminous X-ray sources accreting above the Eddington limit'.

4.1 Introduction

In this chapter we present the implementation of a model aimed at indirectly estimating the masses of binary ULXs through a comparison of binary evolutionary tracks to the emission properties of their optical counterparts. Clearly, it is crucial to determine the masses of the two components of a ULX binary, but it is also very difficult to measure them directly (e.g. Roberts et al. 2011; Liu et al. 2013; Motch et al. 2014). Therefore, it is very important to develop reliable indirect methods to constrain them.
We apply our model to the counterparts of two well-known ULXs, namely NGC 1313 X-2 and NGC 4559 X-7. The optical emission of an accreting binary is produced by the irradiated donor star and the accretion disc. It has been already shown that comparison of stellar evolutionary tracks of ULXs with the photometric properties of their optical counterparts on the colour-magnitude diagram can be used to constrain the masses of their donor stars (e.g. Soria et al. 2005; Copperwheat et al. 2005, 2007) Patruno and Zampieri (2008, 2010) (hereafter PZ and PZ2, respectively) produced evolutionary tracks of ULXs binary systems accreting onto a BH via a standard self-irradiated accretion disc. They showed that a massive donor is needed to fuel persistent ULXs at the required rates (see also Patruno et al. 2005; Rappaport et al. 2005) and provided constrains on both the donor and the BH.
The aim of the work presented in this chapter is to extend the model introduced by PZ to systems which accrete at super-Eddington rates via RLOF.

4.2 Self-irradiated accretion discs in ULX binaries: the PZ model

The starting point of our calculation is the model of PZ, that includes X-ray irradiation. As in PZ, we compute the evolution of representative ULX binary systems with black holes (BHs) of 20 and $100 M_{\odot}$, and donor masses in the range between 8-25 $M_{\odot}$. The system is evolved up to the giant phase by means of an updated version of the Eggleton code. The emission properties and the track followed on the colour-magnitude diagram (CMD) are computed with the PZ code during the contact phases. We assume Population I chemical composition (Helium abundance Y = 0.28, metal abundance Z = 0.02), a mixing length parameter $\alpha = 2.0$ and an overshoot constant $\delta_{ov} = 1.2$. Wind mass loss from the donor has been taken into account following the prescription in de Jager et al. 1988 (see Patruno et al. 2005, Madhusudhan et al. 2006 and PZ for details). However, accretion takes place only when the donor fills its Roche Lobe.

In PZ accretion is assumed to be always sub-Eddington and the accretion rate is not allowed to exceed the critical rate $\dot{M}_{crit} \simeq 10 \dot{M}_{Edd}$ (for a standard efficiency of 0.1; $\dot{M}_{Edd} = L_{Edd}/c^2$). Once the mass transfer rate sets in, a standard accretion disc (Shakura and Sunyaev (1973)) forms. Its inner and outer radii are assumed to be equal to $r_{in} = 6 r_g$, where r_g is the gravitational radius, and $r_{out} = 2 r_{circ}$, where r_{circ} is the circularization radius.[1] A fraction of the X-ray flux emitted from the inner regions of the disc is absorbed and thermalized in the outer parts. Following Copperwheat et al. (2005), the local temperature stratification induced by such X-ray heating is given by:

$$T(\tau) = \left\{ \frac{\pi}{\sigma} \Big[B_x(\tau) + B_d(\tau) \Big] \right\}^{1/4}. \tag{4.1}$$

Here $B_x(\tau)$ is the energy flux originating from X-ray irradiation, while $B_d(\tau)$ refers to the contribution of viscous heating. The former takes the form:

$$B_x(\tau) = \frac{1}{2} S_x \left\{ k_s f_s(\alpha) \left(\frac{\xi}{1+\xi} \right) \left[A_s - \left(A_s - \frac{1}{2} \right) e^{\tau / A_s} \right] \right.$$
$$\left. + k_h f_h(\alpha) \left(\frac{1}{1+\xi} \right) \left[A_h + \left(A_h - \frac{1}{2} \right) e^{\tau / A_h} \right] \right\}. \tag{4.2}$$

where S_x is the incident X-ray flux absorbed by an annulus of the disc, τ is the optical depth to optical photons, $\xi = S_h / S_s$ is the hardness parameter (ratio of the hard and soft X-ray flux), k_s and k_h are the opacities (in units of the electron scattering opacity) for the soft and hard components of the incident radiation, $f_s(\alpha)$ and $f_h(\alpha)$ are functions that depend on the geometry of the system (α being the angle of incidence of the X-rays measured from the normal to the surface), $A_s = cos(\alpha)/k_s$ and $A_h = cos(\alpha)/k_h$. The incident X-ray flux has been calculated from the following expression:

$$S_x = \frac{L_x}{(1-A) 4 \pi r^2} \tag{4.3}$$

[1] The circularization radius r_{circ} is defined as the radius where the Keplerian angular momentum is equal to the angular momentum of the gas streaming from the inner Lagrangian point. The accreting gas settles initially at r_{circ} and then spreads at smaller and larger radii because of viscous dissipation and conservation of angular momentum, forming a disc (see e.g. Frank et al. 2002, chapter 5.2 for details). Typically, r_{circ} is a significant fraction of the Roche lobe radius, so that the disc outer boundary r_{out} cannot extend more than a few times r_{circ}. We take $r_{out} = 2 r_{circ}$ as a reference value.

where $L_x = \eta \dot{M} c^2$ is the bolometric luminosity of the source and A is the albedo to X-rays, fixed at $A = 0.9$[2]. The disc spectrum is calculated integrating over the disc annuli and assuming that they emit as black bodies at the temperature given by equation (4.1) (where we set $\tau = 2/3$ as the photospheric optical depth).

Concerning the star, assuming it at a distance equal to the binary separation a, its temperature is given by an expression similar to equation (4.1):

$$T_{star} = \left[T^4_{unirr,star} + T^4_{irr,star} \right]^{1/4}, \tag{4.4}$$

where $\sigma T^4_{unirr,star}$ and $\sigma T^4_{irr,star}$ represent the energy fluxes of the unirradiated star and that originating from X-ray irradiation, respectively. The latter is calculated from:

$$T_{irr,star} = \left[\frac{L_x (1 - A)}{8 \pi \sigma a^2} \right]. \tag{4.5}$$

For further details on the adopted irradiation model we refer to PZ, Wu et al. (2001), and Copperwheat et al. (2005).

4.2.1 Photometry of the donor

In order to perform a direct comparison of the emission properties of ULX binary systems with the available *HST* photometric measurements, in the present version of the code we implemented a different method for calculating the magnitudes of the donor stars. While PZ perform an interpolation of the tabulated magnitudes and bolometric corrections (BC) reported in Cox (1999), here we use the code of Girardi et al. (2003) to calculate the donor magnitudes for a given luminosity, mass and metallicity. Thus, output magnitudes of the donor are now given in different photometric systems, including the Johnson and *HST* systems.

4.3 Modelling super-Eddington accretion in ULX binaries

In the present model, when the accretion rate is below the Eddington limit, the treatment of the accretion flow follows that of PZ. However, in ULX binaries the mass transfer rate from the donor can exceed the Eddington rate. When $\dot{M} \geq \dot{M}_{crit}$, accretion can no longer proceed via a standard thin disc and a bimodal structure is assumed: an inner disc with non-standard disc geometry and temperature profile (vertical scale height comparable to the radius and $T \propto r^{-1/2}$), and an outer disc with standard structure. In addition, a massive optically thick outflow (with an inner advection dominated region) is assumed to set in. In these physical conditions, also the geometry of X-ray irradiation varies. Abramowicz et al. (1988) investigated accretion at $\dot{M} \geq \dot{M}_{crit}$ assuming a vertically integrated disc structure. In these discs (usually referred to as slim discs) the radial infall velocity and the horizontal pressure gradient become important and can no longer be neglected in the Euler equation. The radial infall velocity of the gas is comparable to the rotational velocity. As the optical depth in the disc is very large, the radiation diffusion timescale becomes larger than the infall timescale and the gas transports

[2] Varying the value of the albedo A between 0.7 and 0.95 has no major effects on the position and shape of the evolutionary tracks on the CMD, as shown in PZ2.

a large fraction of the internal energy inwards, producing a strong horizontal heat flux. Such an advective cooling changes the energy balance of the disc. As a consequence, the disc scale height and the radial temperature profile differ significantly from the standard case. Moreover, a large fraction of the advected heat is accreted by the BH and the disc luminosity is no longer proportional to the accretion rate, but tends asymptotically to $\approx 10 L_{Edd}$ (Watarai et al., 2000).

When the luminosity exceeds the Eddington limit, the huge pressure force produced by the emitted X-ray flux effectively removes gas from the surface of the disc, overcoming the gravitational force and leading to the formation of a massive radiation-driven outflow. This effect is clearly seen in recent 2D magneto-hydro simulations of super-Eddington accretion (e.g Takeuchi et al. 2013). Observational evidence of the existence of high velocity outflows in ULXs comes from the discovery of emission and absorption lines in their optical (Fabrika et al. 2015) and X-ray (Pinto et al., 2016a) spectra. Then, in the following we assume that, when the mass transfer rate exceeds the Eddington limit, a bimodal disc structure sets in: an outer standard disc and an inner advection-dominated slim disc with an outflow. The radius where the transition between the two regimes occurs, as well as the onset and extension of the outflow, depend on the mass transfer rate.

4.3.1 Bimodal disc without outflow

As a starting point towards a full implementation of our model, we first consider the case of an hybrid (inner advection-dominated plus outer viscosity-dominated) disc structure without an outflow. The innermost and outermost radii of the disc are $r_{in} = 6 r_g$ and $r_{out} = 2 r_{circ}$. For the inner slim disc we adopt the parameterization (for self-similar solutions) of Watarai et al. (2000). They define the boundary radius r_0 as the radial coordinate where the structure of the disc changes (the inward advected heat is equal to the viscously dissipated heat). It is:

$$r_0 \propto \dot{m} r_g \,, \tag{4.6}$$

where $\dot{m} = \dot{M}/\dot{M}_{Edd}$. As $\dot{m}$ increases, the inner slim disc becomes more and more extended. This bimodal configuration affects the temperature profile (and hence the emitted spectrum) of the disc: in the inner region, where advection dominates, the temperature varies as $T(r) \propto r^{-1/2}$, while in the outer region, where viscous heating is dominant, $T(r) \propto r^{-3/4}$. Fig. 4.1 shows the luminosity calculated integrating the emitted flux over all the annuli of the disc and assuming local blackbody emission. When advection becomes important, the disc luminosity significantly overcomes the Eddington limit but it never exceeds $\approx 10 L_{Edd}$ (Watarai and Fukue 1999; Watarai et al. 2000). In fact, as $\dot{m}$ increases, the photon mean free path becomes progressively smaller and the radiation diffusion timescale progressively larger. As a consequence, more and more internal energy is effectively advected inward on a dynamical timescale and not radiated away.

The geometry of the inner slim portion of the disc significantly affects also self-irradiation. The flux emitted from the inner regions intercepts the outer parts if $dH/dr \ll 1$ and $H/r \ll 1$ (see e.g. Frank et al. 2002). In the inner regions of a slim disc $H \simeq r$ and therefore the X-ray flux produced inside is not able to illuminate the outside. In these conditions the geometry of disc self-irradiation must be reconsidered.

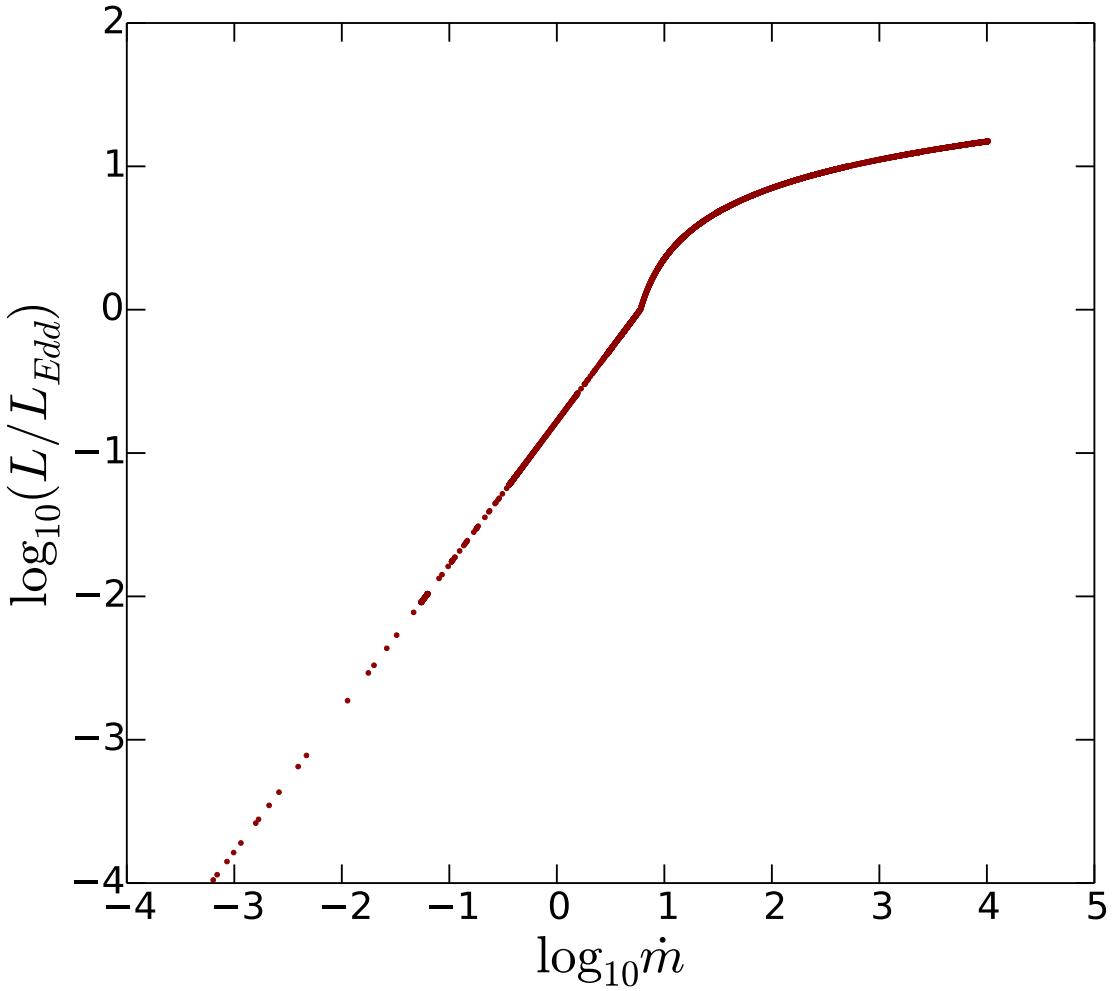

Figure 4.1: Luminosity of a bimodal disc without outflow as a function of the mass transfer rate. The curve is obtained plotting the luminosity calculated at different phases and for different systems (donors of 10 and 25 $M_\odot$, BHs of 20 and 100 $M_\odot$).

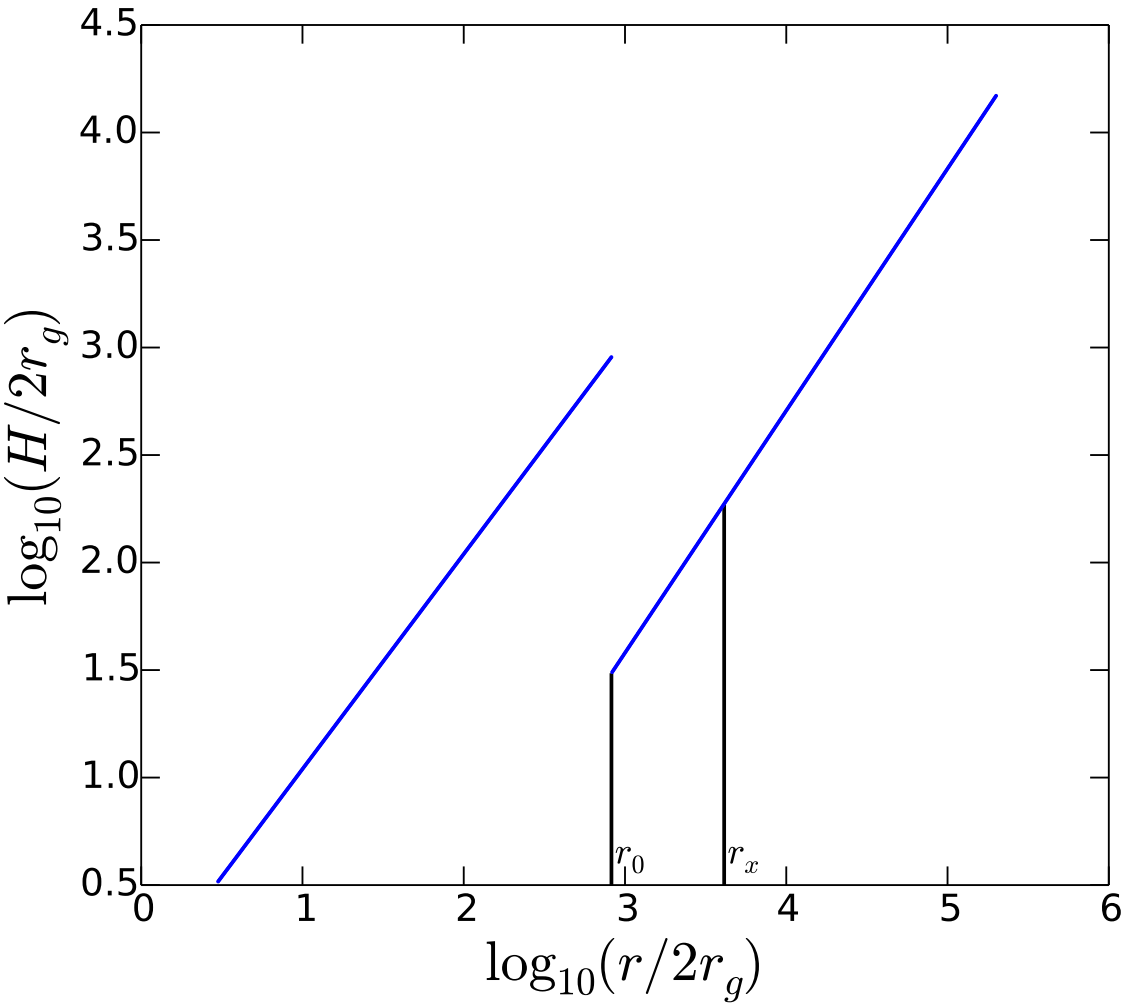

Figure 4.2: Inner slim disc and outer standard disc scale height (in units of $2r_g$ and in logaritmic scale) in our bimodal-disc model ($\dot{m} = 509$). The portion of the standard disc that can irradiate the outer regions is that between r_0 and r_x.

Geometry of disc self-irradiation

In our hybrid disc structure the X-ray irradiating flux is produced outside the boundary radius r_0. In these conditions, the fact that X-ray emission from the inner disc is isotropic or partially beamed has no effect on the outside region. We consider as irradiating flux all the radiation emitted between radii r_0 and r_x, where r_x marks approximately the boundary of the region where the gas temperature falls within the X-rays-ultraviolet (UV) energy band (see Fig. 4.2). If the temperature at r_0 is lower than $\simeq 5 \times 10^5$ K, no X-ray irradiation takes place. The extension of the irradiating region ($\Delta r = r_x - r_0$) for BHs of 20 $M_\odot$ and 100 $M_\odot$ is shown in Fig. 4.3. The extension of the irradiating region depends on the mass transfer rate, since both r_0 and r_x depend on $\dot{m}$. Δr reaches a maximum at around a few thousands $\dot{m}$ and then decreases sharply. The irradiation luminosity shows a similar trend with the mass transfer rate. Clearly, the irradiating region is less extended than in the standard case. However, the X-ray-UV irradiation luminosity is bigger, because the flux increases with the mass transfer rate.

As the results of the evolutionary tracks with a bimodal disc structure without an outflow are likely not to be directly relevant for modelling ULXs, they are reported in Appendix B and are no longer discussed further.

4.3.2 Bimodal disc with outflow

In addition to a bimodal disc, we included in our model of ULX binaries also an optically thick outflow. For sufficiently large $\dot{m}$ the outflow can cover all the slim disc and part of the standard disc. Following the treatment of Poutanen et al. (2007) (to which we refer for a detailed discussion), the outflow can be divided in four zones, depending on the optical depth (measured in the direction perpendicular to the disc plane) and on the mechanism involved in the energy transport. They are delimited by three characteristic radii: $r_{ph,in}$ and $r_{ph,out}$ mark the inner and outer radial locations of the photosphere, while r_{sph} (spherization radius; Shakura and Sunyaev 1973) is the radius below (above) which energy transport is dominated by the outward advected heat (radiation diffusion). The expression of these radii is given by (Poutanen et al., 2007):

$$\frac{r_{ph,in}}{r_{in}} \approx 1 + \frac{1}{3\epsilon_w} \tag{4.7}$$

$$\frac{r_{sph}}{r_{in}} \approx \left[1.34 - 0.4\epsilon_w + 0.1\epsilon_w^2 - (1.1 - 0.7\epsilon_w)\dot{m}_0^{-2/3}\right]\dot{m}_0 \tag{4.8}$$

$$\frac{r_{ph,out}}{r_{in}} \approx 3\epsilon_w \dot{m}_0^{3/2}\,, \tag{4.9}$$

where $\dot{m}_0 = \dot{M}/\dot{M}_{crit}$ and ϵ_w is the fraction of radiative energy spent in accelerating the outflow. Following Poutanen et al. (2007), we set $\epsilon_w = 0.5$. In terms of these radii the outflow is divided in four zones:

- zone A is the inner optically thin part of the outflow at $r < r_{ph,in}$;
- zone B is the inner optically thick part of the outflow between $r_{ph,in}$ and r_{sph}, where outward advection of energy dominates;

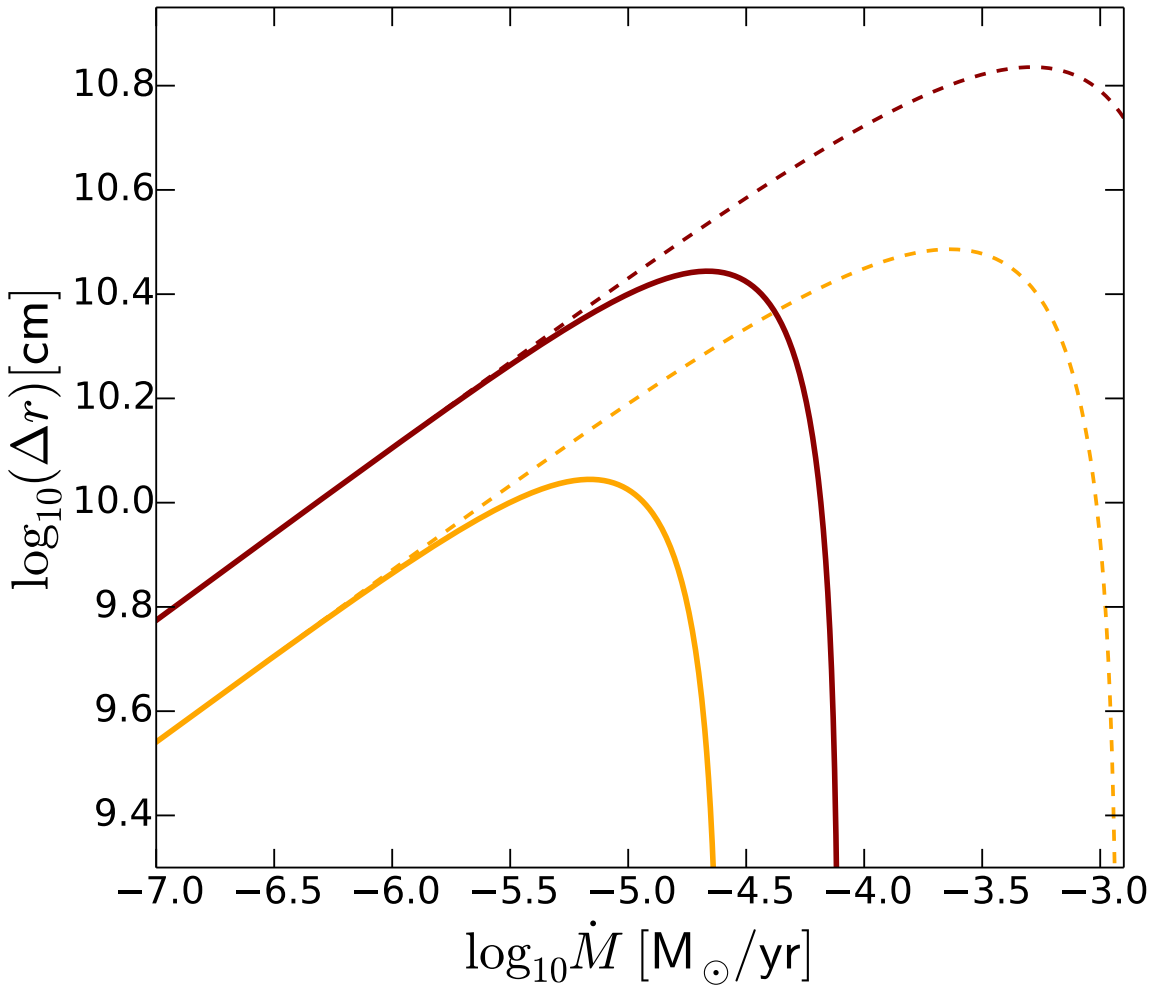

*Figure 4.3: X-ray-UV irradiating region of the disc for the model without outflow (dashed line) and with outflow (solid line). The (**red**) curves on the top refer to a BH of $100M_\odot f$, while the (**orange**) curves on the bottom to a BH of $20M_\odot$. For the case without outflow $\Delta r = r_x - r_0$, while for the case with outflow $\Delta r = r_x - r_{ph}$.*

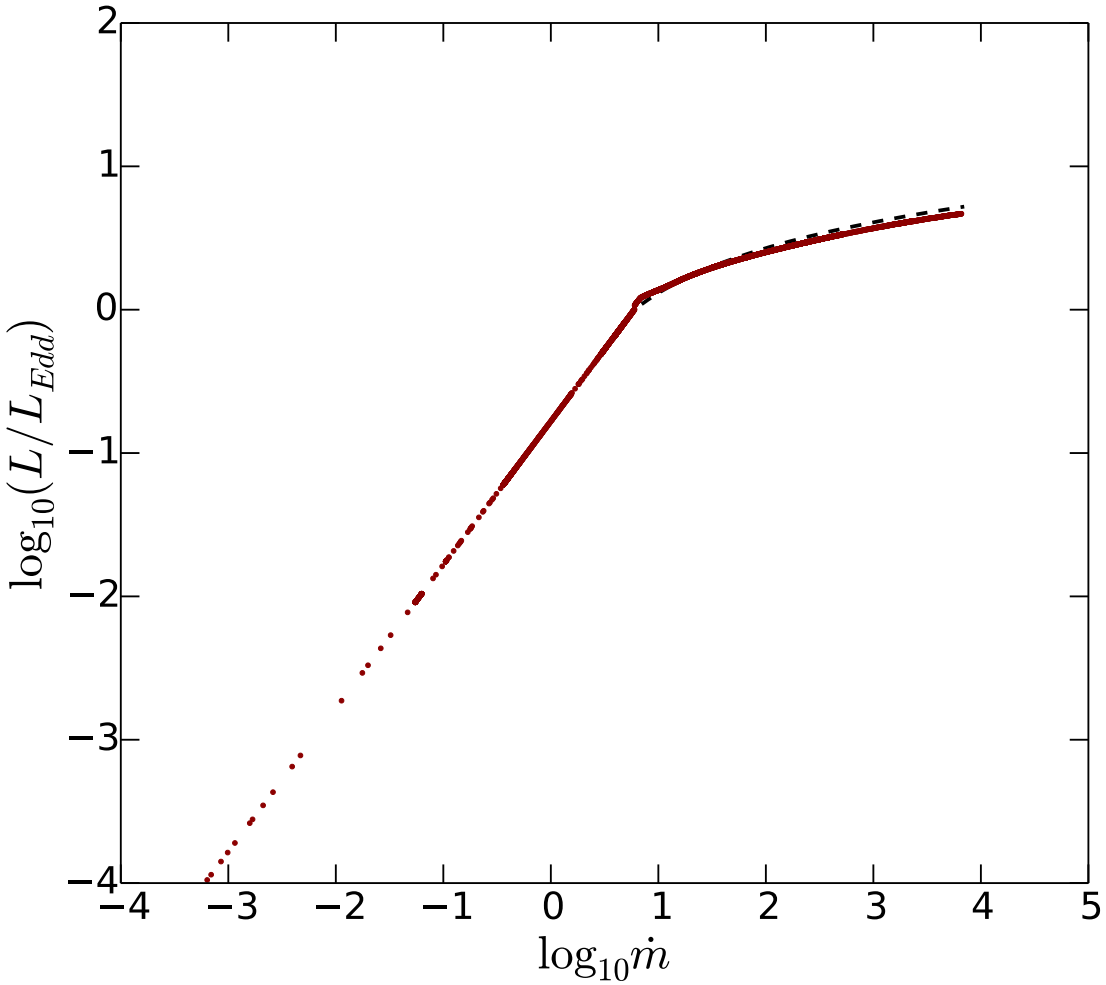

Figure 4.4: Luminosity of a bimodal disc with outflow as a function of the accretion rate. The dashed line is the expression reported in equation (4.12), while the dotted lines are the values computed for our models (donor mass of 10 $M_\odot$ and 20 $M_\odot$, BH masses 20 $M_\odot$ and 100 $M_\odot$).

Table 4.1: Donor and BH masses of the binary systems considered in this work

Donor star ($M_\odot$)	Black Hole ($M_\odot$)
8.0; 10.0; 12.0	20.0
15.0; 20.0; 25.0	20.0
8.0; 10.0; 12.0	100.0
15.0; 20.0; 25.0	100.0

- zone C is the outer optically thick part of the outflow between r_{sph} and $r_{ph,out}$, where diffusion of radiation dominates;
- zone D is the outer optically thin part of the outflow at $r > r_{ph,out}$.

We approximate the temperature profile of the outflow in regions B and C with the following expressions:

$$T_B(r) = T_{r_{sph}} \left(\frac{r}{r_{sph}} \right)^{-1/2} \tag{4.10}$$

$$T_C(r) = T_{r_{sph}} \left(\frac{r}{r_{sph}} \right)^{-3/4} , \tag{4.11}$$

where $T_{r_{sph}} = 1.5 m^{-1/4} \dot{m_0}^{-1/2} (1+0.3 \dot{m_0}^{-3/4})(1-\epsilon_w)\,\mathrm{keV}$ is the temperature at the spherization radius. The total luminosity of the system is calculated integrating the emitted flux over all the annuli of the disc for $r_{in} < r < r_{ph,in}$ and $r_{ph,out} < r < r_{out}$, and over all radial slices of the outflow for $r_{ph,in} < r < r_{ph,out}$. Local blackbody emission at the appropriate temperature is assumed. The final expression of the emitted luminosity is (Poutanen et al., 2007):

$$L \approx L_{Edd} \left(1 + \frac{3}{5} \ln \dot{m_0} \right) . \tag{4.12}$$

This luminosity is shown in Fig. 4.4, along with that computed from our models (see below). The fractional difference is at most 10%.

Geometry of disc self-irradiation

The geometry of disc self-irradiation with the outflow is different from that without the outflow. The outflow reprocesses entirely the disc emission up to $r_{ph,out} \gg r_0$ and has a scale height of order unity. Consequently, radiation from the disc emitted inside $r_{ph,out}$ cannot hit the region of the disc outside it. The irradiating region is then $\Delta r = r_x - r_{ph,out}$, with $r_{ph,out} \gg r_0$, and is thus significantly less extended than in the pure slim disc case. Moreover, its dependence on the mass transfer rate is different, as shown in Fig. 4.3. It has a maximum at a few hundreds times $\dot{m}$. An additional contribution to the emitting region may come also from the photosphere of the outflow located at $r_{ph,out}$ and facing the outer disc. We add its contribution to the irradiating flux if its temperature falls in the X-ray-UV band (eq.[4.11]). However, this is usually not sufficient to

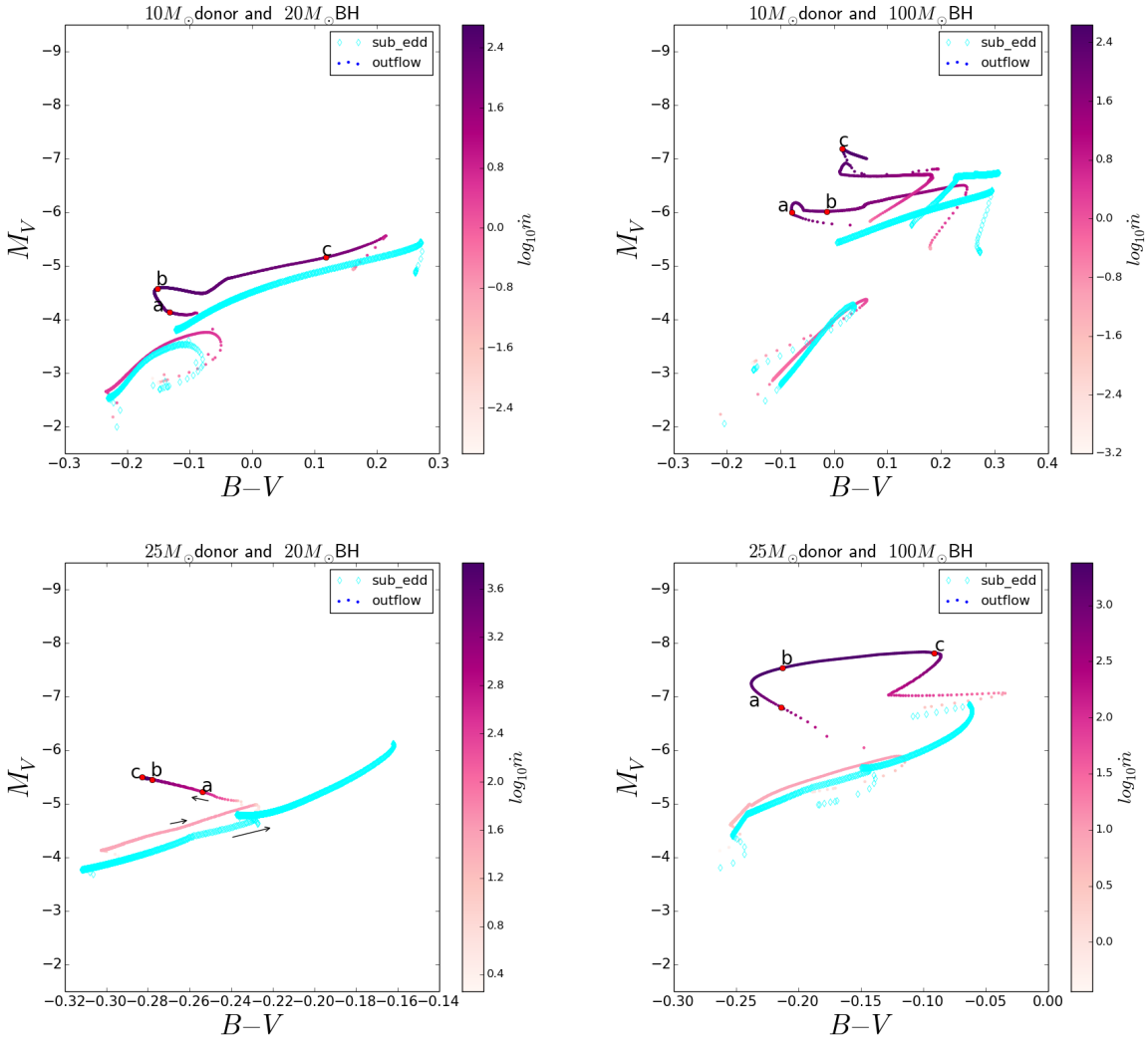

Figure 4.5: Evolution on the colour-magnitude diagram of a ULX binary system with a donor mass of $10M_\odot$ (upper panels) or $25M_\odot$ (lower panels) at zero age main sequence and a BH mass of $20M_\odot$ (left panels) or $100M_\odot$ (right panels). The thick (light grey, cyan in the on-line version) line represents the evolution calculated assuming standard sub-Eddington accretion (PZ). The thin (gray-scale, color-scale in the on-line version) line represents the new evolution computed for super-Eddington accretion. Points a, b and c mark the evolutionary phases at which the spectral energy distribution is computed. The track of the system with a $25M_\odot$ donor and a $20M_\odot$BH was interrupted when $r_{ph,out} > r_{out}$. Representative arrows in the bottom left panel indicate the direction of the evolution along the tracks.

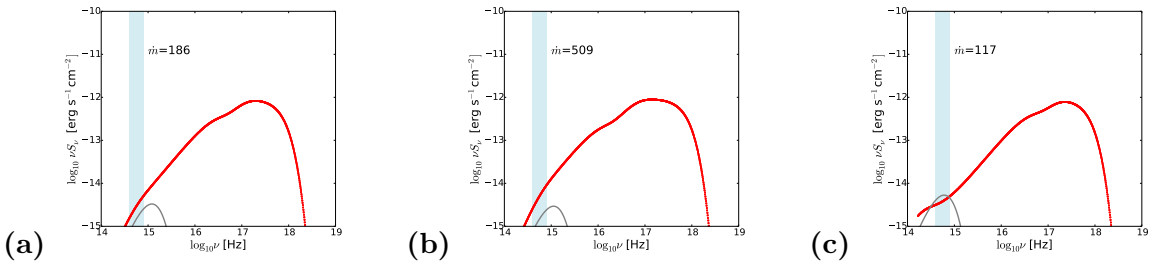

Figure 4.6: Optical-through-X-ray spectrum of the system with a $10M_\odot$ donor and a $20M_\odot$ BH at the phases marked with a, b and c on the evolutionary track for super-Eddington accretion. The thick (red) line represents the spectrum of the self-irradiated outer disc plus the outflow and the innermost slim disc, while the thin (gray) line is the spectrum of the X-ray heated donor. The gray (light blue) strip marks the optical band. At phases a and c both the disc and the outflow irradiate the outer standard disc, while at phase b only the outflow does it. The mass of the donor star at each time is: $M_{donor,a} \simeq 4.4M_\odot$, $M_{donor,b} \simeq 4.2M_\odot$ and $M_{donor,c} \simeq 2.03M_\odot$.

compensate the 'missing' flux from the region between r_0 and $r_{ph,out}$, and therefore irradiation is smaller than in the pure slim disc case. Also in this case, the fact that X-ray emission from the inner disc is isotropic or partially beamed has no effect on the outside region.

4.4 Results

4.4.1 Photometry

We compared the B, V and R (Johnson) magnitudes obtained with the new treatment of the photometry of the donor star presented in Sec. 4.2.1 with those of PZ. The accretion disc and X-ray irradiation are not taken into account, while the decrement of the mass of the donor during its evolution is considered. The maximum difference between the magnitudes computed with the old and new treatment of photometry occurs for massive ($> 20M_\odot$) stars during main sequence and is $\sim 40\%$. For comparison, in PZ the maximum fractional deviation of the adopted fitting formula from the tabulated reference magnitudes is $\sim 15\%$.

4.4.2 Evolutionary tracks on the color-magnitude diagram

We used the model described in the previous Sections to compute the evolution of 12 binary systems with the initial donor and BH masses reported in Tab. 4.1. In the following, we will show the results for systems with donors of $10M_\odot$ and $25M_\odot$, and BHs of $20M_\odot$ and $100M_\odot$. The initial binary separation of all systems is chosen so that the first contact phase occurs during MS. The possibility that accretion starts only after MS is not considered because, for massive donors, this phase is too short to be consistent with the characteristic age of the optical emission nebulae typically associated to ULXs (> 500 thousand years; Pakull and Mirioni 2002).

In Fig. 4.5 we show the evolutionary tracks on the color-magnitude diagram calculated in this paper, compared to those reported in PZ (case AB mass transfer). In the lower part of each track the donor is on the Main Sequence (MS). On the upper part the donor has left the MS and

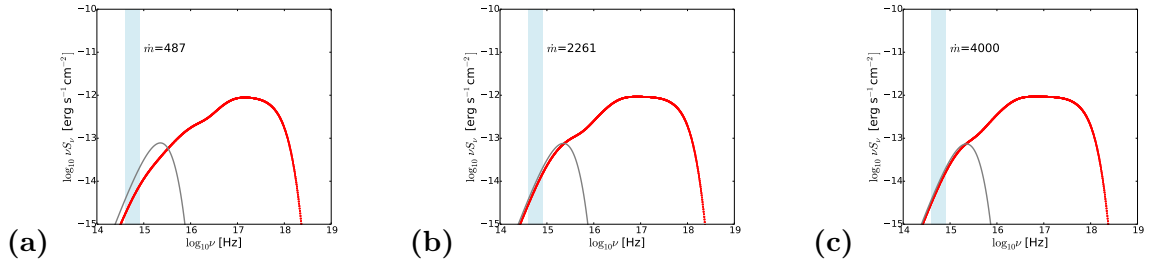

Figure 4.7: Same as Figure 4.6 for a $25M_\odot$ donor and a $20M_\odot$ BH. At phase a the outflow irradiate the outer standard disc, while at phases b and c there is no irradiation. The mass of the donor star at each time is: $M_{donor,a} \simeq 11.80M_\odot$, $M_{donor,b} \simeq 11.78M_\odot$ and $M_{donor,c} \simeq 11.70M_\odot$.

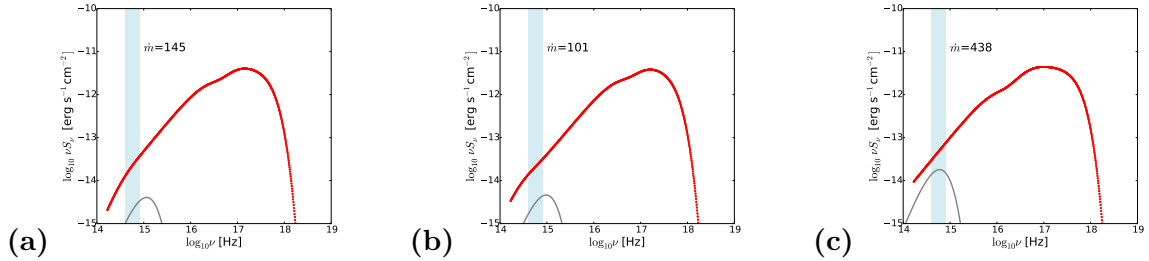

Figure 4.8: Same as Figure 4.6 for a $10M_\odot$ donor and a $100M_\odot$ BH. At phases a and c only the photosphere of the outflow at $r_{ph,out}$ radiates the outer standard disc. In b both the outflow and the disc irradiate the outer standard disc. In c the donor is on the Giant branch. The mass of the donor star at each time is: $M_{donor,a} \simeq 4.99M_\odot$, $M_{donor,b} \simeq 3.90M_\odot$ and $M_{donor,c} \simeq 1.38M_\odot$.

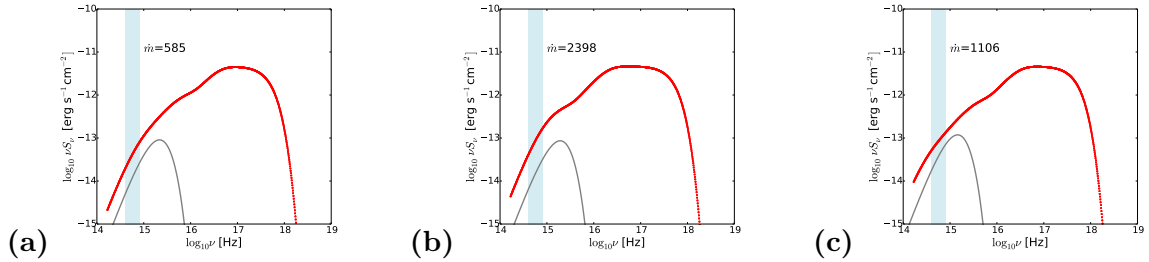

Figure 4.9: Same as Figure 4.6 for a $25M_\odot$ donor and a $100M_\odot$ BH. At phases a and c no irradiation occurs. The mass of the donor star at each time is: $M_{donor,a} \simeq 13.06M_\odot$, $M_{donor,b} \simeq 11.46M_\odot$ and $M_{donor,c} \simeq 7.30M_\odot$.

moves towards the Giant Branch. During MS $\dot{m}$ is sub-Eddington or mildly super-Eddington, while afterwards accretion becomes highly super-Eddington. As shown in Fig. 4.5, during MS our tracks almost overlap those obtained by PZ. The residual difference depends mainly on the different method used for calculating the donor magnitude (see Sec. 4.4.1) and on the fact that $\dot{m}$ is mildly super-Eddington.

When the donor evolves off the MS, the effects induced by the new structure of the accretion flow (super-Eddington accretion with outflow) become relevant and the tracks differ significantly from those of PZ. The evolutionary tracks are brighter and bluer than those computed assuming Eddington-limited accretion. These features depend on the combination of two effects. First, owing to the larger $\dot{m}$, the flux emitted from the outer standard accretion disc grows significantly. Then, the temperature in the disc and the irradiating flux become progressively higher than in PZ, despite the fact that the extension of the irradiation region is reduced. Second, even if the X-ray-UV emitting region of the disc is hidden below the optically thick outflow, the photosphere of the latter can have a temperature sufficiently high to effectively irradiate the outer regions. These effects increase both the emitted luminosity and irradiation making the system appearing brighter and bluer.

As the system evolves, the orbital separation increases, the accretion disc becomes bigger and the disc emission comparatively redder. In addition, at variance with PZ, in our model we allow the mass ratio to vary during the evolution of the binary system. As all our evolved donors lose a considerable amount of mass, the separation and the accretion disc are bigger than in PZ. We note that the track of the system with a $25M_{\odot}$ donor and a $20M_{\odot}$BH was interrupted when $r_{ph,out} > r_{out}$, as the outflow starts to engulf the binary because of the very high mass transfer and outflow rates, and the model is no longer self-consistent. While this does not rule out the possibility that these systems exist and may reproduce some of the observed ULXs, they are likely to evolve in a significantly different way and treating them is beyond the goals of the present investigation.

In general, systems with a $20M_{\odot}$ BH and $12 - 20M_{\odot}$ donors accreting supercritically are characterized by rather blue colors (F450W – F555W $\simeq -0.2 : +0.1$) and high luminosity ($M_V \simeq -4 : -6.5$) when the donor has evolved off the main sequence. Systems with a massive ($100M_{\odot}$) BH accreting supercritically from evolved donors of similar mass have comparable colours but can reach $M_V \simeq -8$.

Points a, b and c on the colour-magnitude diagram in Figure 4.5 mark the post-MS evolutionary phases at which optical-through-X-ray spectra are computed. They are shown in Figures 4.6 - 4.9 and refer to phases with high mass transfer rate. The X-ray spectrum includes the contribution of the disc and the outflow, assuming that they emit locally as blackbodies at different temperatures. A more realistic description of the inner disc spectrum, which involves modelling additional physical processes, will be presented in a forthcoming paper. The bump at optical wavelengths that forms in standard accretion discs because of self-irradiation (e.g. Sanbuichi et al. 1993) is suppressed as irradiation is comparatively less important than the intrinsic disc emission at very high $\dot{m}$. The flux emitted from the accretion disc overcomes that from the star in almost all cases.

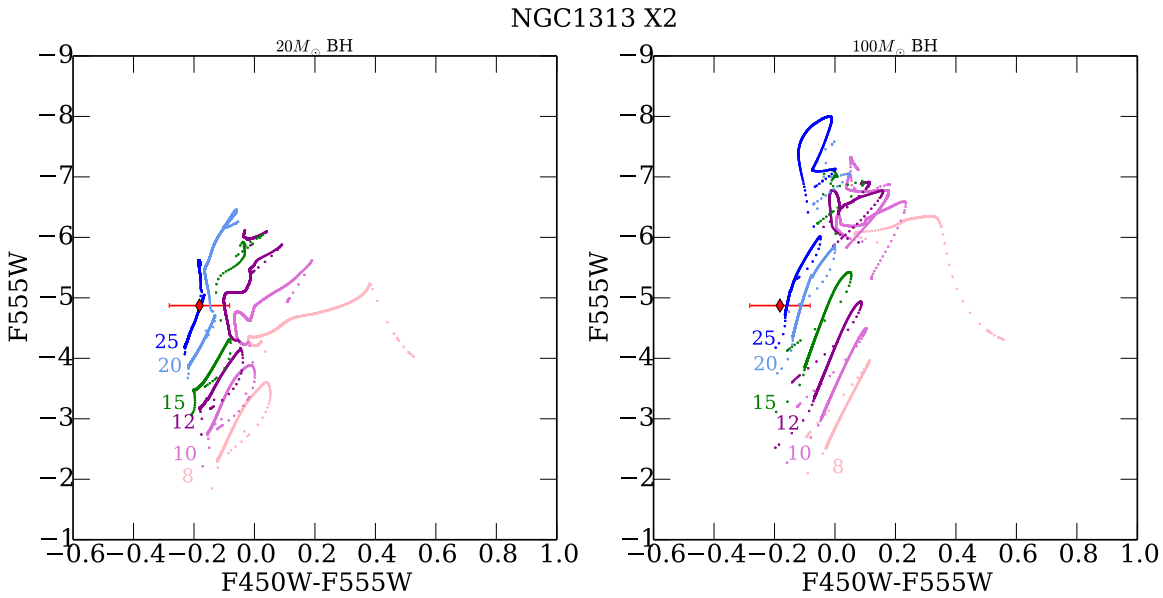

Figure 4.10: Evolution on the colour-magnitude diagram of ULX binary systems with a BH mass of $20M_\odot$ *(left) and* $100M_\odot$ *(right) for donors with different initial main sequence masses (from* $8M_\odot$ *up to* $25M_\odot$*). Magnitudes are in the HST photometric system. The point represents the mean value of all the measured magnitudes of NGC 1313 X-2 (see text for details). We assume a distance of 4.07 Mpc.*

4.4.3 Comparison with the HST photometry of NGC 1313 X-2 and NGC 4559 X-7

A detailed comparison of the computed evolutionary tracks and optical-through-X-ray spectra of our models with a sample of ULXs is ongoing. Here we show a preliminary application to NGC 1313 X-2 and NGC 4559 X-7 using only optical data. We compare the position on the CMD of the optical counterparts of NGC1313 X-2 and NGC4559 X-7 with the evolutionary tracks of our systems. We account for ULXs variability taking the mean values of the magnitudes collected in different epochs. Absolute magnitudes are calculated for the distances reported in the literature and adopted for the parent population studies (see below).

NGC 1313 X-2

NGC 1313 X-2 (hereafter X-2) is one of the best known and studied ULXs, hosted in the barred spiral galaxy NGC 1313. In the following, we assume a distance of 4.07 ± 0.22 Mpc (Grisé et al. 2008) and an optical extinction $E(B-V) = 0.13$ (Tao et al. 2011). The observed X-ray luminosity of NGC 1313 X-2 is in the range 10^{39}–3×10^{40} erg s^{-1} (Mucciarelli et al. 2007). The environment of this ULX has been analyzed in detail (Zampieri et al. 2004; Mucciarelli et al. 2007; Grisé et al. 2008). The source is found to reside in an OB association aged $\sim 20 \pm 5$ Myrs (Grisé et al., 2008). Intensive *HST* monitoring of its optical counterpart in 2009 led to the determination of the orbital period of the system, which turns out to be $P = 6.12 \pm 0.16$ days in case of significant X-ray irradiation of the donor or $P = 12.24 \pm 0.16$ if X-ray irradiation is negligible (Liu et al. 2009, Zampieri et al. 2012). As the source appears to show both regular

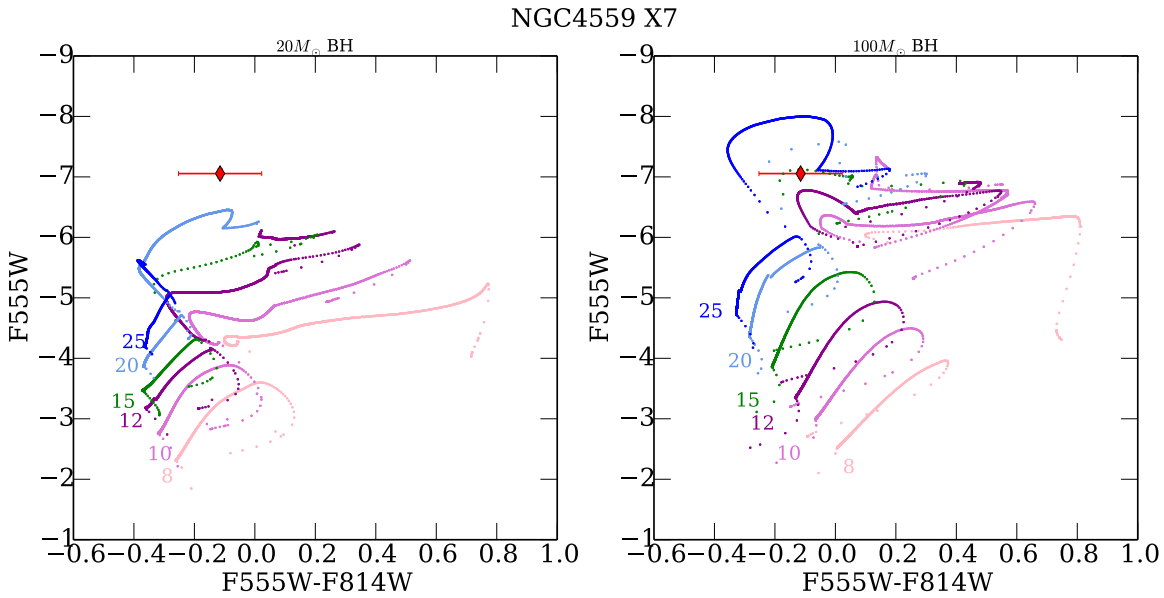

Figure 4.11: Same as Fig. 4.10 for NGC4559 X-7. We assume a distance of 10 Mpc.

and stocastic variability at the level of ~ 0.1 mag, in the following we will consider the average of all measurements of X-2 taken during the 2009 monitoring campaign (F555W $= -4.88 \pm 0.06$, F450W-F555W $= -0.18 \pm 0.1$; Tao et al. 2011)[3]. This value then represents a reasonable smoothed average of the observed orbital and X-ray irradiation-induced variability.

In Fig. 4.10 we compare the position on the colour-magnitude diagram of the optical counterpart of X-2 with the evolutionary tracks of ULX binaries accreting above Eddington. The point representing X-2 intersects: (i) the tracks of a $100M_\odot$ BH with donors of 20 and $25M_\odot$ in the MS phase, (ii) the tracks of a stellar-mass BH with donors of 12, 15, 20 and $25M_\odot$ during the terminal age MS or H-shell burning phase, when accretion is super-critical. We rule out the first possibility because the duration of the entire tracks that intersect the photometric point is less than 8–12 Myrs, not in agreement with the age of the parent stellar population ($\sim 20 \pm 5$ Myrs). Concerning the stellar-mass BH case (ii), we exclude donors more massive than $20M_\odot$ for similar reasons. On the other hand, case (ii) with donors having initial masses in the range $12 - 15M_\odot$ is in agreement with the age of the parent stellar population. For these systems the bolometric luminosity ($\sim 10^{40}$ erg s^{-1}) is consistent with the observed range of values. It is important to note that, at the time of intersection, accretion is highly super-critical and the optical emission is dominated by the outer standard portion of the disc. Nonetheless, the contribution of the star to the optical flux is 10%, sufficient to produce a ~ 0.1 mag modulation on the optical light curve if irradiation is important. The orbital period P is between 4.5 and 5 days, in reasonable agreement with the reported photometric periodicity. In this case, the observed ~ 6 days modulation would represent a single orbital period and the maximum of the light curve would correspond to superior conjunction, when the largest fraction of the irradiated

[3]The error on the colour is the quadratic sum of the standard deviations $\sigma = (\sum_i (m_i - \bar{m})^2/(n-1))^{1/2}$ of the single magnitudes, where we take σ (not the error of the mean) as representing the dispersion of the measurements induced by the intrinsic source variability.

donor surface is visible. Any evidence of a $\sim$ 12 days asymmetric modulation would rule out this scenario.

NGC 4559 X-7

NGC 4559 X-7 (hereafter X-7) is a ULX located in the outerskirts of the spiral galaxy NGC 4559. We assume a Galactic extinction $E(B-V) = 0.018$ (Tao et al., 2011) and a distance of 10 Mpc (Soria et al., 2005). The ULX is embedded in a young star-forming complex with age $\leq$ 30 Myrs and stars in the *Chandra* error circle are Red or Blue Supergiants with age $\sim$ 20 Myrs. The average magnitude and colours of the optical counterpart of X-7 are F555W $= -7.05 \pm 0.08$ and F555W-F814W $= -0.11 \pm 0.13$ (from two measurements; Tao et al. 2011), while its bolometric luminosity is $\sim 5 \times 10^{40}$ erg s^{-1} (Soria et al., 2005).

In Fig. 4.11 we compare the position on the colour-magnitude diagram of the optical counterpart of X-7 with the evolutionary tracks of ULX binaries accreting above Eddington. We rule out that X-7 is powered by accretion onto a stellar-mass BH of 20 $M_{\odot}$ because, even for super-Eddington accretion from a $20-25 M_{\odot}$ donor in the H-shell burning phase, the magnitude is too low to reproduce the observed photometry. Conversely, the point representing X-7 intersects the evolutionary tracks of a 100 $M_{\odot}$ BH accreting above Eddington from a $15-25 M_{\odot}$ evolved donor. Assuming a characteristic age of $\sim$ 20 Myrs, a $\sim 15 M_{\odot}$ donor is more plausible. Tracks computed for a more extended grid of BH masses show agreement for masses in the range $70-100 M_{\odot}$ (Ambrosi, Zampieri et al. in prep.). For all these systems the bolometric luminosity ($\sim 4 \times 10^{40}$ erg s^{-1}) is in fair agreement with the observed value.

Finally, we note that, irrespective of the BH mass, both the counterparts of NGC 1313 X-2 and NGC 4559 X-7 appear to be associated with evolved donors. Despite the post-MS phase of a massive star not being its longest evolutionary phase, it is certainly the only one with significant super-Eddington rates. Limiting the comparison to this phase, the position on the post-MS tracks of NGC 1313 X-2 (where agreement with the observed photometry is found) falls on a rather short-lived phase of the system (when the orbital separation is rapidly increasing), while it falls along a comparatively slower evolutionary phase for NGC 4559 X-7. On this ground alone, the probability of finding NGC 4559 X-7 at the observed position on the CMD seems somewhat higher than that of NGC 1313 X-2.

4.5 Discussion and conclusions

In this work we modelled the optical emission of ULXs accreting super-Eddington. At first we considered a bimodal accretion disc formed by an inner advection-dominated slim disc and an outer standard disc. Then, we included the effects of an outflow produced by radiation pressure. As noted above, the case of a pure slim disc is useful to understand the effects of supercritical accretion on the emission properties of the disc and on self-irradiation. For $\dot{m} > 10^3$ the outflow can completely cover the accretion disc and the evolution can no longer be followed with the present model.

Super-critical accretion has considerable effects on the optical emission. The disc self-

irradiation is very different from that produced in the standard case. The innermost regions do not radiate the outer ones. Two competing effects influence self-irradiation. On one side, the irradiating flux grows with $\dot{m}$. On the other side, it decreases because the size of the irradiating region diminishes. Irradiation is considerably stronger than that produced by an Eddington-limited disc, but at very high $\dot{m}$ it is progressively less important than the intrinsic disc and donor emission.

During MS, the evolutionary tracks on the CMD obtained with our model almost overlap with those of Patruno and Zampieri (2008). The residual difference depends on the treatment of photometry and to the fact that the accretion rate can be mildly super-Eddington. On the other hand, the post MS evolution is markedly different and is characterized by two phases. Initially, when the accretion disc is not very extended, the luminosity increases with $\dot{m}$ and the system becomes bluer ($B-V=-0.3-0.1$). As the orbital separation increases, the accretion disc becomes bigger, the emission becomes progressively redder and the system moves to the right on the CMD. At super-Eddington rates, the disc flux typically overcomes that produced by the donor (apart from the case of small black holes and very massive donors) and the 'optical bump' that characterizes standard self-irradiated discs disappears.

We compared the predictions of our model with the *HST* observations of NGC 1313 X-2 and NGC 4559 X-7. We constrain the donor and the BH mass of these objects, considering as a further constraint the age of the parent population and the observed bolometric luminosity. The position of NGC 1313 X-2 on the CMD is in agreement with a $20M_{\odot}$ BH accreting above the Eddington limit from a post-MS donor with initial mass in the range $12-15M_{\odot}$. The orbital period of the system is ~ 5 days, in fair agreement with the observed one. It should be emphasized that the $20M_{\odot}$ BH and $12-15M_{\odot}$ donor tracks intersect the observed photometric point of X-2 because accretion is highly super-critical and the optical emission, dominated by the outer standard portion of the disc, is significantly enhanced and blue in comparison with that for Eddington-limited accretion.

We now compare the results of the dedicated analysis of NGC 1313 X-2 presented by Patruno and Zampieri (2010) (PZ2) for Eddington-limited accretion with those obtained here. PZ2 found that the photometric point representing X-2 is well reproduced by a system with a $\sim 50-100M_{\odot}$ BH and a MS donor of $\sim 12-15M_{\odot}$ or by a system with a $\sim 20M_{\odot}$ BH undergoing mass transfer from a H-shell burning donor of $\sim 12-15M_{\odot}$. The orbital period of the systems that intersect X-2 on the CMD is ~ 6 days in the first case and ~ 12 days in the second case. In both cases accretion is Eddington-limited. A similar conclusion for the $\sim 20M_{\odot}$ BH case was reached by Mapelli and Zampieri (2014) who calculated the magnitudes of simulated ULX binaries evolved in young star clusters and compared them with the available photometry of several ULXs. The adopted code is that of PZ and PZ2, while the input parameters at the beginning of the Roche-lobe overflow phase (radius, mass, optical luminosity, effective temperature, and age of the donor, mass of the BH, orbital period) were provided by N-body simulations, that did not produce matches with systems having BH masses larger than $\sim 25M_{\odot}$.

In fact, besides the accretion regime, there are two other aspects to consider when comparing the results of PZ2 with our ones. First, PZ2 considered the *HST* ACS observations performed in 2003 (taken from Mucciarelli et al. 2007), while here we considered a longer dataset, averaging over the variability induced by the orbital motion and X-ray irradiation. Second, the conversion

from *HST* ACS/WFC F435W and F555W filters to the standard Johnson photometric system leads to some inaccuracy, especially for variable sources (see e. g. Sirianni et al. 2005). We note that also Mapelli and Zampieri (2014) used the first 2003 *HST* ACS photometric epoch (taken from Gladstone et al. 2013).

Using the two 2003 *HST* photometric measurements adopted in PZ2, we find agreement with the tracks of $20-25M_{\odot}$ donors during MS for a $100M_{\odot}$ BH and the track of a $20M_{\odot}$ donor at terminal age MS for a $20M_{\odot}$ BH, that do not have the correct age of the parent OB association. This would rule out both Eddington-limited accretion onto a $100M_{\odot}$ BH and super-Eddington accretion onto a $20M_{\odot}$ BH for X-2. On the other hand, comparison with the average photometry of the 2009 *HST* monitoring campaign still rules out the $100M_{\odot}$ BH scenario, but allows for super-Eddington accretion onto a $20M_{\odot}$ BH from a H-shell burning donor of $\sim 12-15M_{\odot}$. Therefore, adopting the 2009 average photometry and performing the comparison with the new tracks in the original *HST* photometric system is crucial to rule out the Eddington-limited $100M_{\odot}$ BH scenario of PZ2 and to pinpoint the matching $20M_{\odot}$ BH super-Eddington system.

Letting aside the details of the photometric comparison, we note that the orbital period of the $20M_{\odot}$ BH matching binary system is ~ 12 days for Eddington-limited accretion, while it is ~ 5 days for super-Eddington accretion. In fact, in order to reach a comparable optical luminosity an Eddington-limited disc has to be more extended, and hence the system has to have a longer orbital period. This would provide a further means to distinguish between Eddington-limited and super-Eddington accretion in this system. Unfortunately, present measurements are not sufficiently accurate to discriminate between a ~ 6 days irradiation-modulated orbital periodicity and a ~ 12 days ellipsoidally-modulated one.

Also the optical counterpart of NGC 4559 X-7 has been previously analysed by PZ. The same caveat concerning the photometric transformation to the Johnson system applies also here, but is less critical. The same *HST* measurement of Soria et al. (2005) is considered. PZ found that X-7 is reproduced by a massive or a stellar-mass BH accreting from a $30-50M_{\odot}$ donor during the H-shell burning phase. We did not consider donors more massive than $25M_{\odot}$ for a 20 $M_{\odot}$ BH because, after the MS, the outflow starts to engulf the binary and the model is no longer self-consistent. For less massive donors, no agreement is found because the optical emission is not sufficiently luminous. For a 100 $M_{\odot}$ BH, agreement is found for evolved donors of $15-25M_{\odot}$, smaller than in the Eddington-limited systems of PZ owing to the fact that super-Eddington accretion makes the tracks more luminous and bluer for a given donor mass.

We note that our result for NGC 1313 X-2 is consistent with the findings of Bachetti et al. (2013), who performed a detailed analysis of the *NuSTAR* and *XMM-Newton* spectra of the source using a slim disc plus Comptonization model and found that they are well described by a low mass BH ($M \sim 20-30M_{\odot}$). The results for NGC 1313 X-2 and NGC 4559 X-7 are also in agreement with the BH masses estimated by Fiacconi et al. 2017 using the same wind model (Poutanen et al., 2007). From the properties of the outflow measured in the X-rays they constrain the masses and accretion rates of NGC 1313 X-1, NGC 55 ULX and NGC 5408 X-1, finding that the BH mass is likely to be in the range $10-100M_{\odot}$.

In the future we will explore in detail the properties of all the ULXs with available optical observations. We will compare them with updated evolutionary tracks covering a wider parameter space in terms of BH and donor masses. The comparison will be performed in the same

photometric system used for the observations, accounting for the variability of the sources and including the optical-through-X-ray spectral energy distribution. Moreover, the case of accreting NSs will be explored in order to asses whether optical emission can help distinguishing between ULXs hosting BHs and NSs. As detecting pulsation has proven to be very difficult, it would be important to have other methods to discriminate among them. Modelling accreting NSs is made more difficult by the dynamical and radiative effects of the magnetic fields, the structure and strength of which in pulsar ULXs are unknown. At present we are working at extending our super-Eddington accretion model to the case of a non-magnetized NS, which can be accommodated with relatively little effort within the present framework. Results will be presented in a forthcoming paper.

Chapter 5

Evolutionary tracks with MESA

Introduction

In the previous chapter we analyzed the effects of super-Eddington accretion on the optical emission of synthetic ULXs considering two representative values for the BH masses: 20 and 100 $M_{\odot}$.

Here we extend the adopted grid of BH and donor masses. At variance with our previous calculation (chapter 4), which was done using the Eggleton code (Eggleton 1971; Pols et al. 1995), we produced the new tracks with the stellar evolution code MESA (Modules for Experiments in Stellar Astrophysics, release 10108, Paxton et al. 2011, 2013, 2015). This choice is motivated by the fact that the modular structure of MESA allows us to easily select different prescriptions for the input physics and the numerical evolution of the system, if needed. Moreover, MESA contains useful tools for simultanous on-screen visualization of the stellar and binary evolution. We briefly discuss the various aspects behind this choice and analyze the main differences between the two codes in the appendix C.

At variance with our previous tracks, the new ones are computed considering the effects of the orbital angular momentum removed from the systems (because of the mass lost with the outflow). This chapter is divided in two parts: the first one is devoted to the description of the new evolutionary tracks, while in the second we apply to them our model of super-Eddington accretion with outflow.

5.1 Initial Conditions

We calculated a new extended grid of binary evolutionary tracks. We run a set of models of binaries accreting via Roche Lobe Overflow considering solar metallicity donors (Y = 0.28, Z= 0.02) with masses in the range $5-30M_{\odot}$ and BH masses in the range $10-100M_{\odot}$. We account for stellar winds adopting the 'Dutch' wind scheme, with the 'de Jager' prescription for low temperature stars (Paxton et al., 2011).

We set the start of the RLOF phase during Main Sequence (MS), when the central Hydrogen

Initial P_{orb} [days]						
M_d \ M_{BH}	10.0	20.0	30.0	50.0	70.0	100.0
5.0	1.01	1.02	1.02	1.02	1.02	1.00
8.0	1.15	1.19	1.21	1.21	1.20	1.19
10.0	1.22	1.28	1.29	1.30	1.30	1.30
12.0	1.28	1.36	1.38	1.39	1.39	1.39
15.0	1.37	1.46	1.50	1.52	1.52	1.52
20.0	1.53	1.66	1.71	1.75	1.76	1.77
25.0	1.59	1.74	1.80	1.86	1.88	1.89
30.0	1.65	1.82	1.90	1.98	2.00	2.02

Table 5.1: Initial orbital periods, for the MESA binary evolutionary tracks considered in this chapter They have been calculated considering that RLOF starts when the center Hydrogen abundance of the donor is ∼0.5.

abundance (h1) is $\simeq 0.5$ (case A mass transfer). The evolution is stopped at the onset of Helium burning in the core. First, we run the *star* module for each donor mass and stop it when h1 $\simeq 0.5$. We denote the radius of the donor at this stage with $R = R_{d,h1}$.
We then set the initial period for the binaries combining Kepler law:

$$P \approx 2\pi G^{-1/2} a_1^{3/2} (M_d + M_a)^{-1/2} \tag{5.1}$$

with the Eggleton approximation, under the hypothesys that $R_{d,h1} = R_L$ (Eggleton 1983):

$$a_1 \approx R_{d,h1} \frac{0.6q^{2/3} + \ln(1 + q^{1/3})}{0.49q^{2/3}} \tag{5.2}$$

where a_1 is the initial orbital separation and $q = M_d/M_{BH}$. The combination of BH-donor masses adopted in this work are listed in Tab. 5.1, together with their initial orbital periods, which are in the range 1-2 days.
The RLOF is calculated with the MESA implicit scheme 'Roche Lobe'. We set the minimum mass transfer rate at $\dot{M}_{min} = 1.0 \cdot 10^{-12} M_\odot/yr$.
The timestep is chosen in such a way to generate an adequate time resolution without increasing excessively the computational time (the evolution of a model typically requires $\sim 4-5$ hours). As the binary evolution proceeds faster after the TAMS, the time resolution for the evolution of the donor during the post-MS stages is tighter than that adopted during the MS.
The combination of the most significant MESA parameters used for the calculation of the binaries and the corresponding values are listed in Appendix D. We also set to zero the initial spin of the BH, which increases as accretion proceeds.

Orbital angular momentum through the outflow

According to the model of the accretion disc plus outflow adopted here for computing the emission properties of ULXs (see chapter 4), the evolution proceeds via non-conservative mass

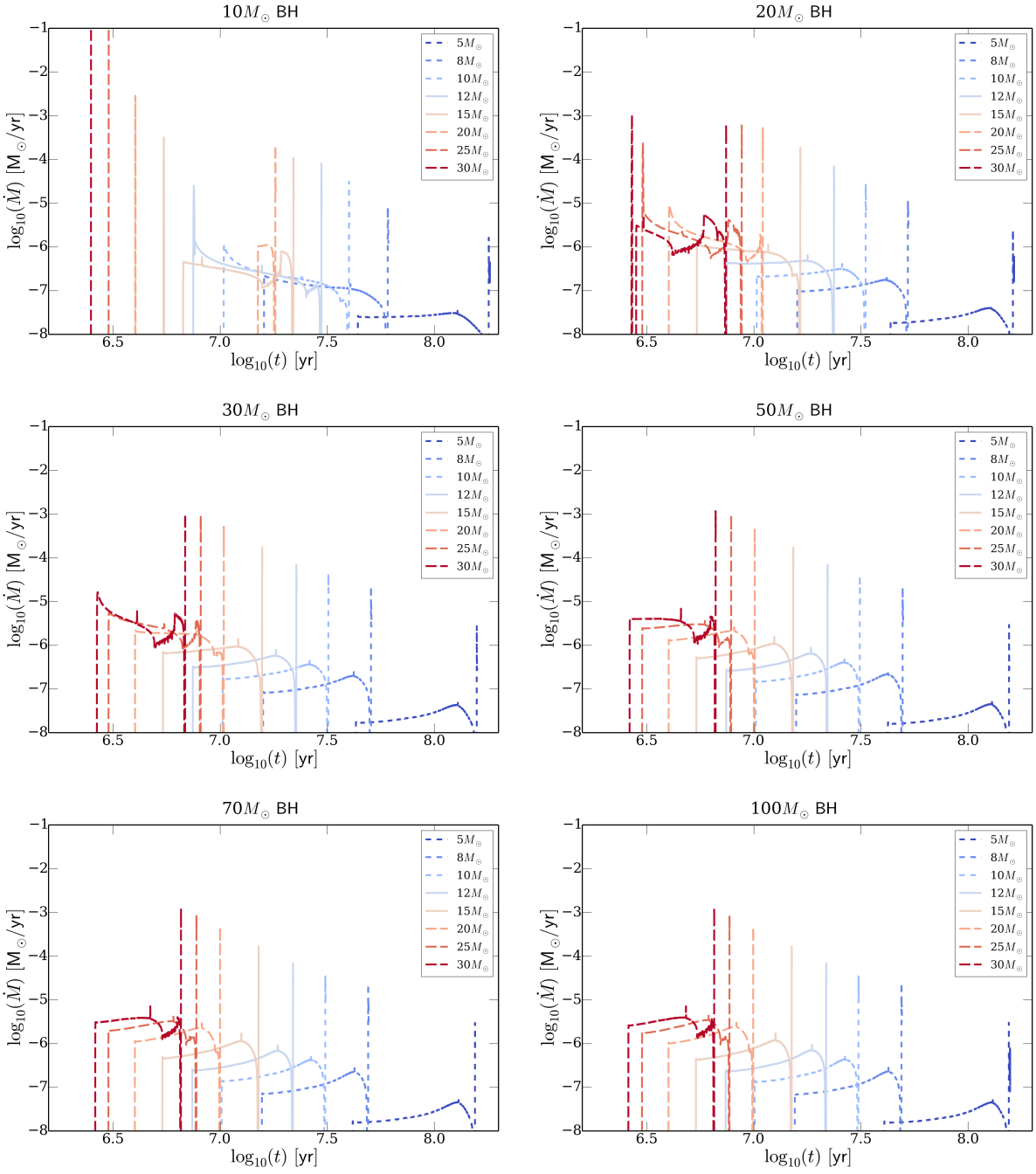

Figure 5.1: Evolution of the mass transfer rate for the binaries analyzed in this work. The BH mass is fixed in each panel. Short dashed lines refer to donors of 5, 8 and 10 $M_\odot$, solid lines to donors of 12 and 15 $M_\odot$, and long dashed lines to more massive donors of 20, 25 and 30 $M_\odot$.

transfer and and the accretion flow is not Eddington-limited. When mass transfer rate becomes super-critical, the mass ejected with the outflow effectively removes also orbital angular momentum. The total outflow rate depends on the fraction of radiative energy spent in launching the wind, ϵ_w, and is given by (eq. 24 of Poutanen et al. 2007):

$$\dot{M}_w \approx a_w \dot{M} \tag{5.3}$$

where $\dot{M}$ is the mass transfer rate and $a_w = \epsilon_w(0.83 - 0.25\epsilon_w)$. We assume that a half of the radiative energy accelerates the outflow ($\epsilon_w = 0.5$)and then $a = 0.3525$.
As the outflow is launched from the inner disc where the radiation pressure is higher, we assume that matter leaves the system from the vicinity of the black hole. The resulting orbital angular momentum loss can be implemented in MESA using the prescription for mass loss described in Sec. 3.1.1 (we refer to Paxton et al. 2015, van den Heuvel 1994; Soberman et al. 1997 for details). According to Eqs. 3.8 and 5.3, we then set $\beta = a_w = 0.3525$, α , δ, $\gamma = 0$.

5.1.1 Evolutionary tracks

The evolution of the mass transfer rate for the systems considered here is shown in Fig. 5.1. The tracks are grouped together according to the initial BH mass and color-coded according to the initial donor mass.

We describe the evolution of the tracks taking as reference the systems accreting onto a $10M_\odot$ BH. They span a wide range in the mass ratio q, which is an important parameter driving the evolution of accreting binaries (see chapter 3). We distinguish three different evolutionary paths.
For very massive donors of 25 and 30 $M_\odot$ (q = 2.5 and q = 3 respectively), the accretion phase starts abruptly with an instability, reaching high rates (up to $10^{-1} - 1\ M_\odot\,/yr$). The timescale for mass transfer ($\tau_{\dot{m}} = \frac{M}{\dot{M}}$) is faster than the thermal timescale, as shown in the top panel of Fig. 5.2: τ_{KH} is up to six orders of magnitude greater than $\tau_{\dot{m}}$. Moreover, as the donor looses mass, it is driven rapidly towards dynamic instability, being the mass transfer rate higher than the maximum value which is permitted by the condition of hydrostatic equilibrium (see chapter 3 and the second and third panels in Fig. 5.2). This effect is likely to lead the system towards a common envelope (CE) phase. This particular phase of binary evolution needs a dedicated modelling with physical assumptions different from those adopted for RLOF accretion, which is the relevant mechanism considered here for persistent ULXs. For this reason we stop the evolution of these systems at this stage, and postpone the inclusion of the CE phase in our model to the future. Donors with initial mass of 15 and 20 $M_\odot$ (q = 1.5 and q = 2 respectively) go through the first, thermal unstable mass transfer episode but do not become dynamically unstable: $\tau_{\dot{m}}$ is shorter than τ_{KH} (top panel of Fig. 5.2) but the ratio between the dynamical timescale and the mass transfer timescale, after having reached a peak, decreases driving the system towards stability (middle panel of Fig. 5.2). As they loose mass, and the BH grows, the mass ratio decreases, the system detaches while the donor restores the thermal equilibrium. Thereafter, mass transfer is stable and proceeds on the nuclear timescale. We emphasize the extreme properties of the track of the 20 $M_\odot$ donor: after having lost more than 50% of its mass during the first fast episode, the system widens and detaches. The donor restart RLOF at about

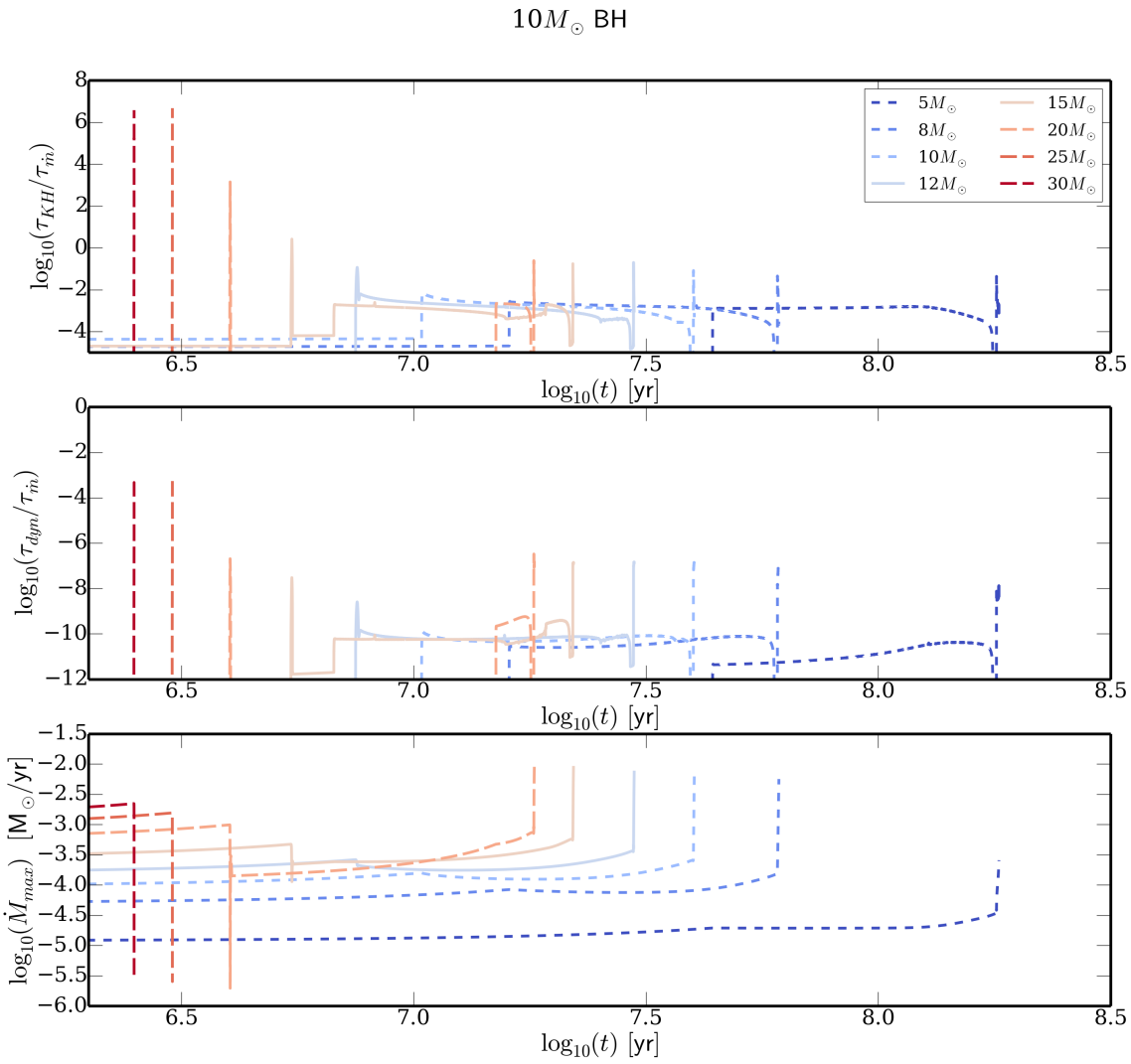

Figure 5.2: Evolution of the characteristic timescales for binaries accreting onto a $10M_\odot$ BH. Upper panel: evolution of the ratio between the thermal (τ_{th}) timescale of the donor and the characteristic timescale for the mass transfer $\tau_{\dot{m}}$. Middle panel: evolution of the ratio between the dynamical timescale τ_{dyn} of the donor and the mass transfer timescale. Lower panel: evolution of the maximum value of mass transfer achievable without perturbing hydrostatic equilibrium of the donor.

TAMS.

For lower donor masses with $q \leq 1$ the evolution does not go through the first unstable phase of mass transfer, but it proceeds smoothly up to the TAMS, being the mass transfer timescale longer than both the Kelvin-Helmholtz and dynamical timescales. Accretion during the giant phase proceeds with high accretion rates, but the donors maintain both hydrostatic and thermal equilibrium.

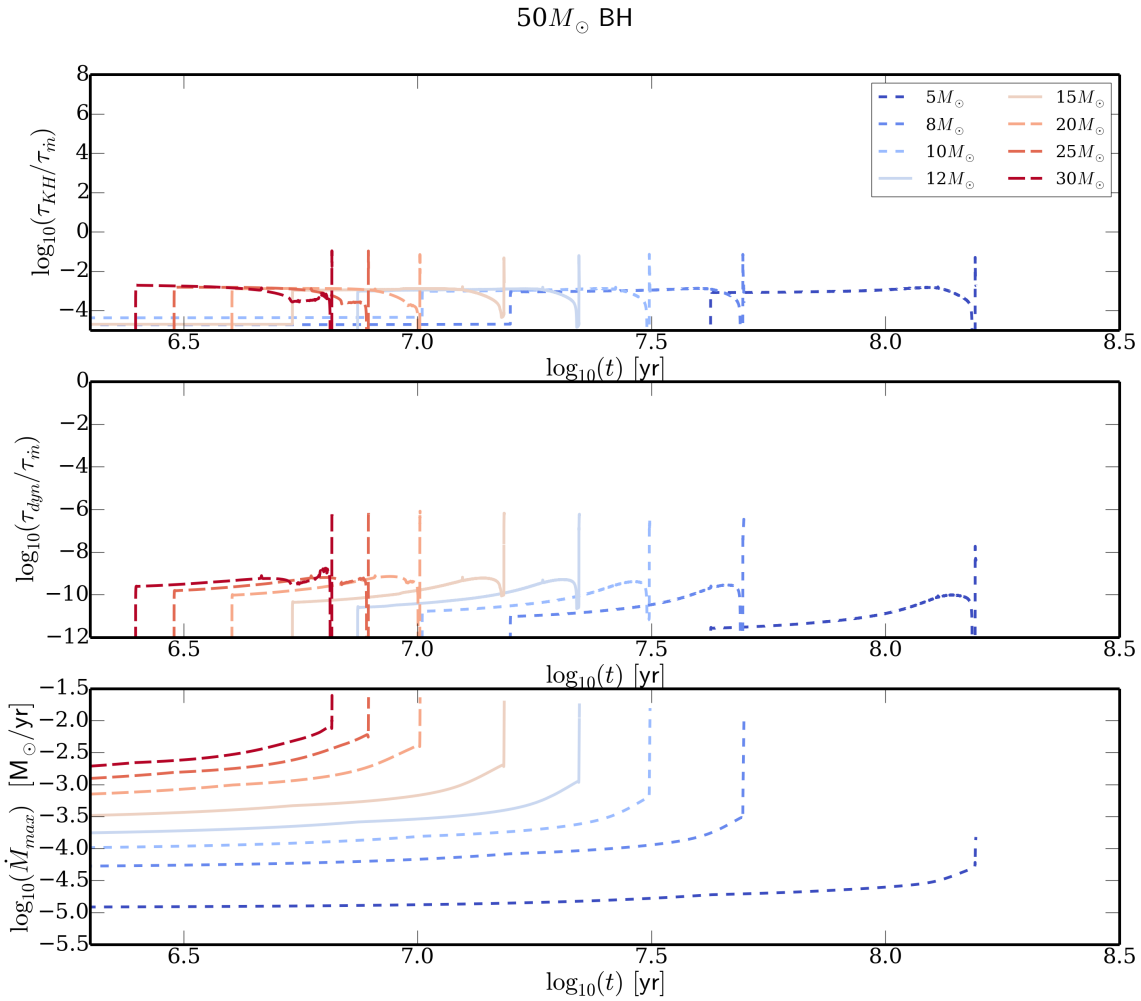

Figure 5.3: Same as Fig. 5.2 for a 50 $M_\odot$ BH.

The evolution of systems accreting onto more massive BHs proceeds in a similar way but the initial accretion episode is less extreme for the more massive donors. For the $20M_\odot$ BH, the 25 $M_\odot$ and 30 $M_\odot$ donors can restore thermal and dynamical equilibrium, at variance with the 10 $M_\odot$ case. For the 50 $M_\odot$ BH the evolution is always stable Fig. 5.3. Accretion is super-Eddington only during the giant phase.

Figs. 5.4- 5.9 show the variation of some of the parameters of the binary systems: donor and BH mass (upper and lower left panels), orbital period and mass ratios (upper and lower right panels). The 5 $M_\odot$ donor is almost totally stripped irrespectively of the BH mass (see upper left panel). Being its mass almost totally stripped, MESA could not find a convergence solution during the final phases of its evolution which has been stopped before the onset of He burning in the nucleus. From Figs. 5.4- 5.9 we see that irrespective of the BH mass, the final orbital period is shorter for systems with more massive donors. For a given BH mass, final orbital periods for

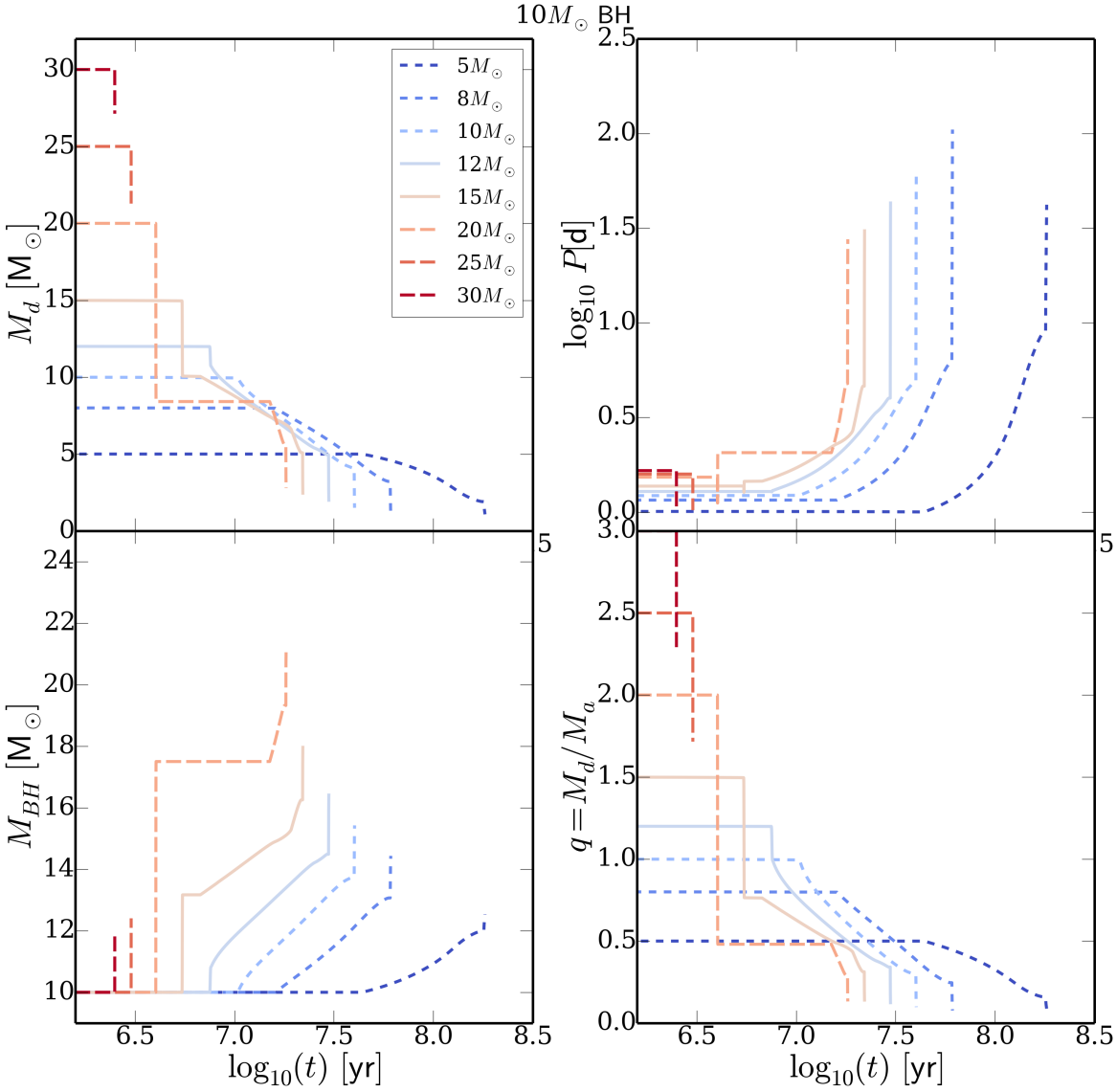

Figure 5.4: Evolution of the binary parameters for systems accreting onto a 10 $M_\odot$ BH: donor mass (upper left), orbital period (upper right), BH mass (lower left), and q ratio (lower right).

$8M_\odot$ donors can be one order of magnitude longer than those for 30 $M_\odot$ donors.

5.2 Evolutionary tracks on the CMD

We apply our model to the evolutionary tracks evolved with MESA. As the tracks obtained with MESA are sampled very tightly ($\sim 10^4$ snapshot each), to reduce the computational time for our code, we resampled them leaving ~ 1400 snapshots for each track. As we did for the tracks computed with the Eggleton code, we calculated the optical emission in the UBVRI Johnson and in the HST WFPC2, ACS and WFC3 photometric systems, with the aim to make the most

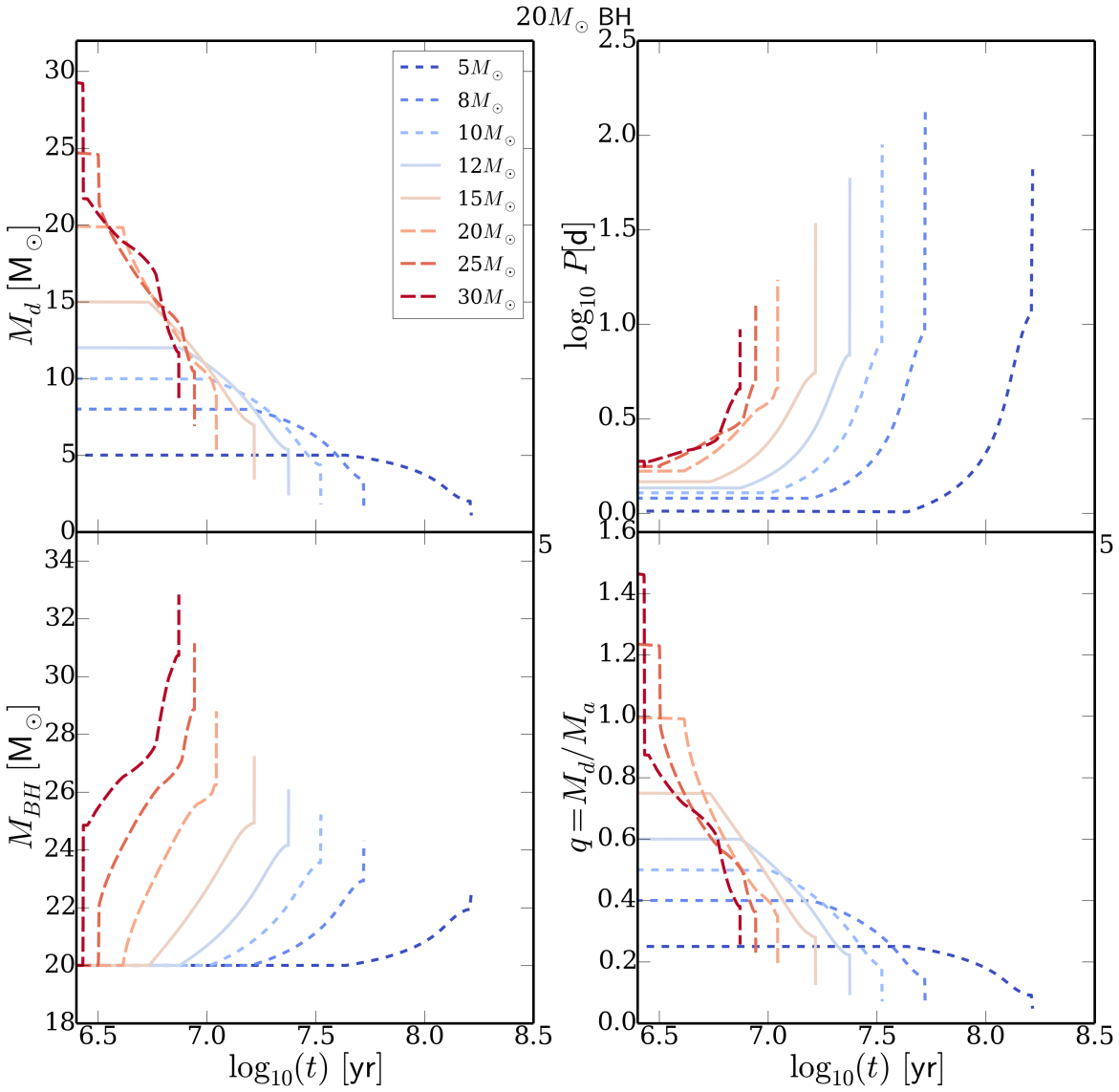

Figure 5.5: Same as Fig. 5.4 for a BH of 20 $M_\odot$.

detailed comparison with the observed optical counterparts of ULXs. Moreover, the code has been adapted so that one can easily add other photometric systems, if needed.
In order to better compare the properties of the new evolutionary tracks with those reported in chapter 4, here we briefly summarize the results previously obtained. The optical emission of accreting binary systems is produced by different sources,each contributing with a different weight to the total optical emitted flux, depending on the accretion regime and evolutionary stage. These sources are:

- the donor star, the properties of which are different from that of an isolated star with the same initial mass (chapter 3). During RLOF, its radius is constrained to be the Roche

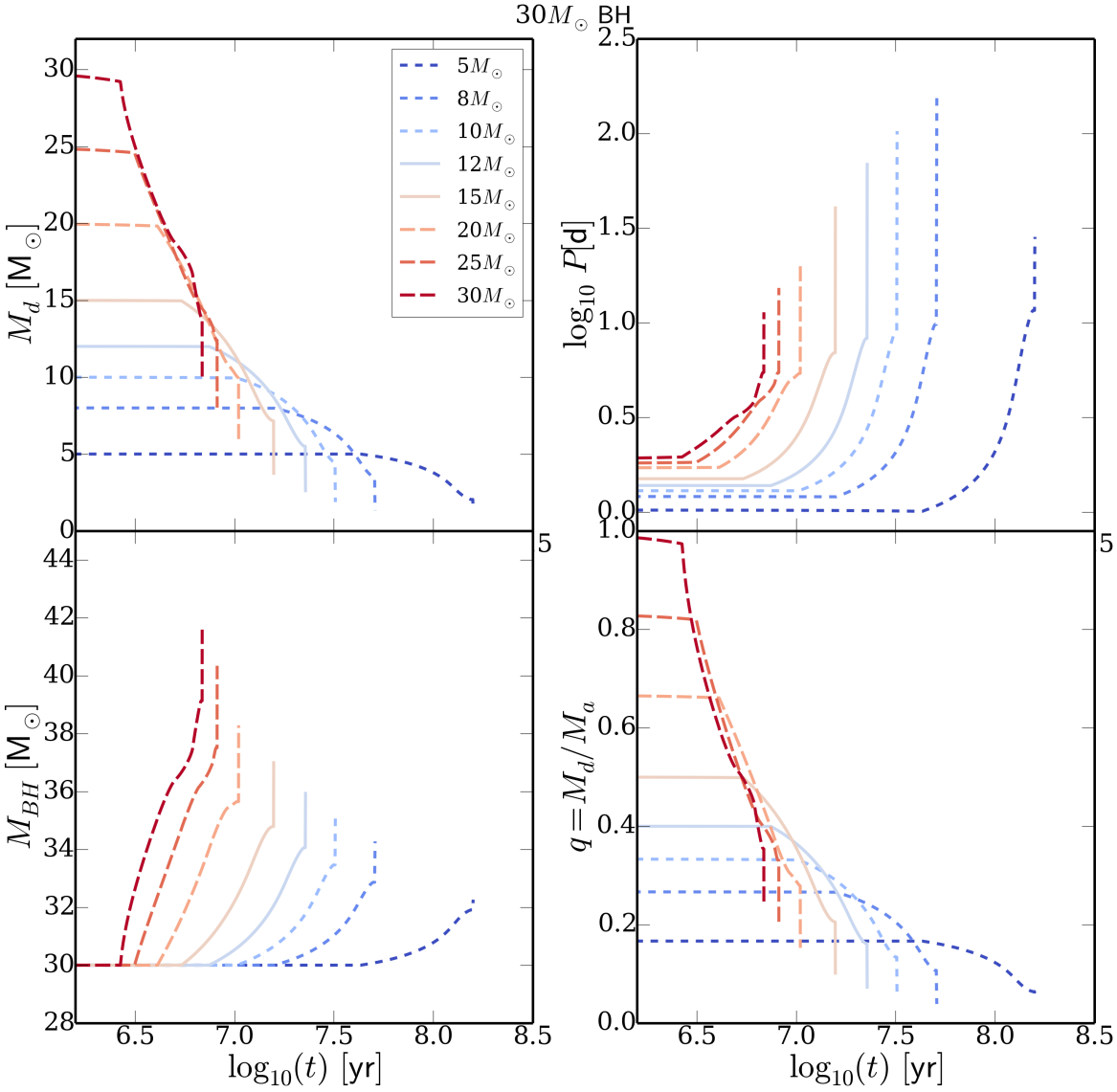

Figure 5.6: Same as Fig. 5.4 for a BH of 30 $M_\odot$.

lobe radius and its temperature is determined by the condition of thermal equilibrium. Moreover, it can be also heated up by the X-ray flux which is produced by the disc;

- the outer part of the accretion disc. In both cases of sub-Eddington and super-Eddington accretion, the disc in the outer region is a standard Shakura & Sunyaev disc, emitting an amount of optical flux proportional to the mass transfer rate. Also this region can reprocess and thermalize the X-ray from the innermost regions;

- the outflow, the extension of which depends on the mass transfer rate. For extremely super-Eddington accretion, the outflow produces a large emission of optical radiation, which can significantly contribute to the observed magnitude and, in the more extreme

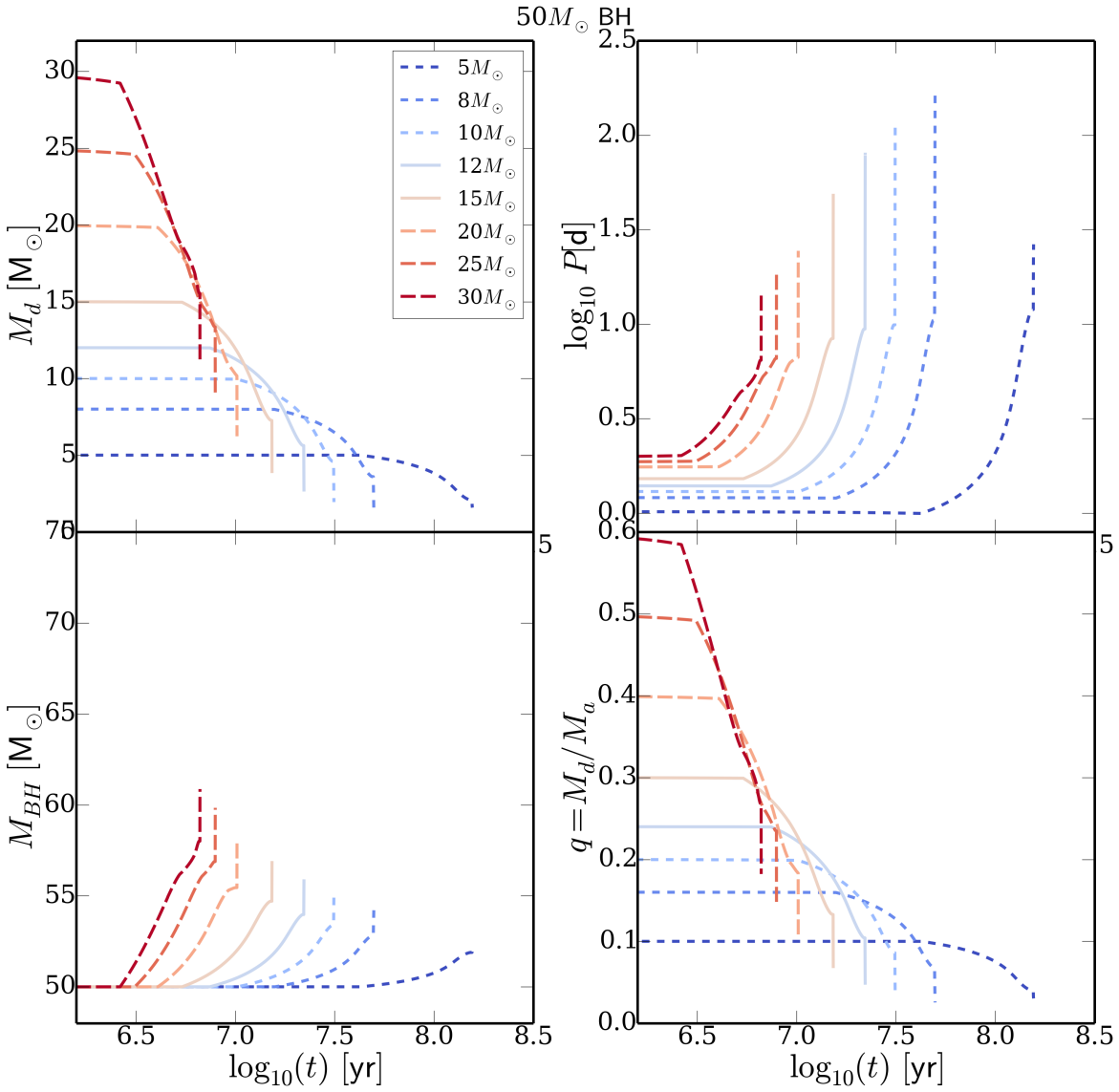

Figure 5.7: Same as Fig. 5.4 for a BH of 50 $M_\odot$.

regimes, be the dominant component.

As mentioned above, a strong contribution to the optical emission comes from the reprocessing of the X-ray-UV radiation produced by the inner regions of the disc and impinging in the outer disc and the donor star. If the disc is accreting at sub-Eddington rates, the flux intercepting the outer disc and the donor star makes the latter bluer than an isolated star with the same mass (see e.g. PZ) and produces a bump in the red tail of the disc optical spectrum (see e.g. Sanbuichi et al. 1993).

Self-irradiation for super-Eddington accretion is more complex. In Ambrosi and Zampieri (2018) we showed that the innermost regions of the disc do not irradiate the outer ones, because of

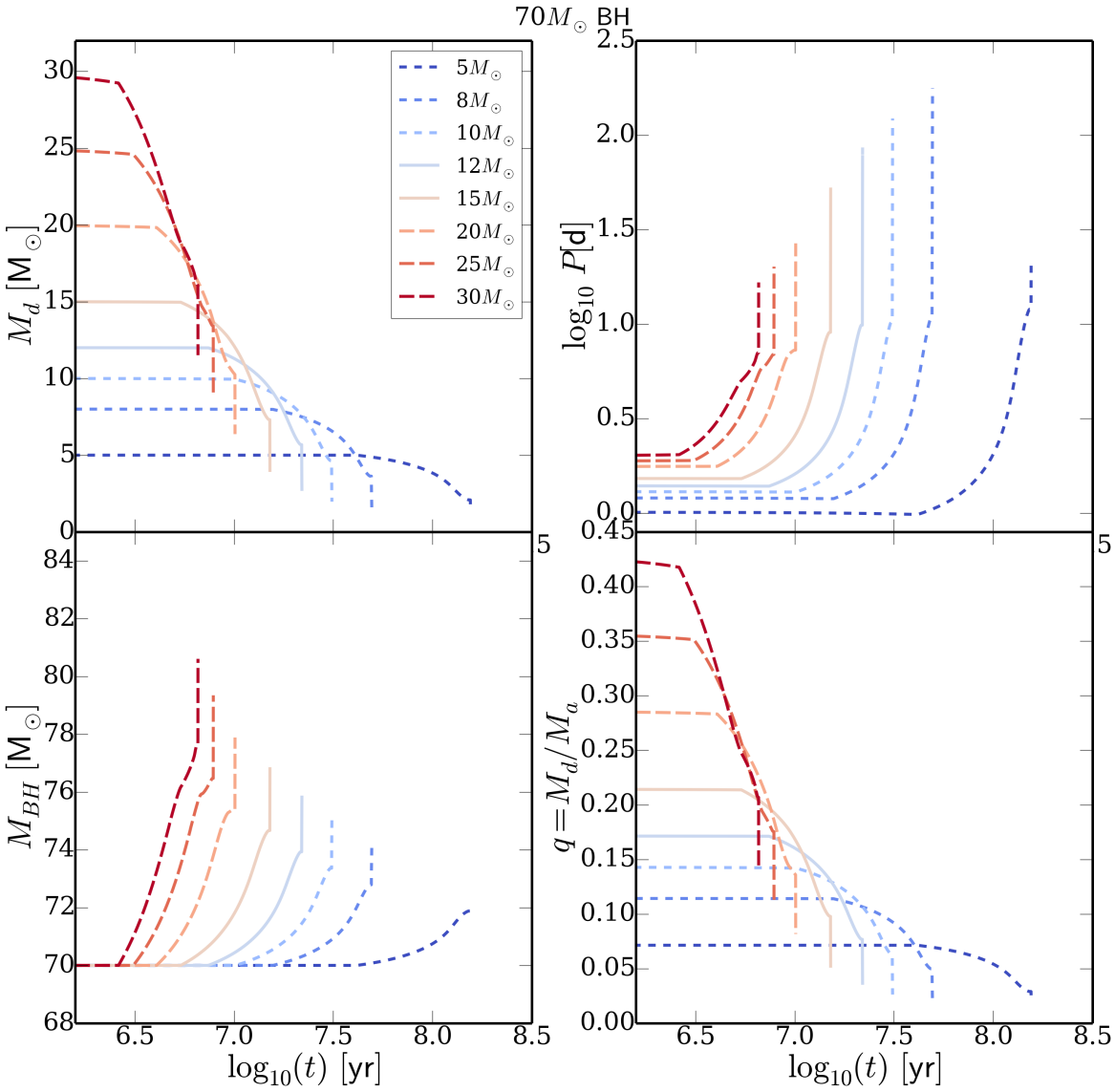

Figure 5.8: Same as Fig. 5.4 for a BH of 70 $M_\odot$.

the intervening outflow. The X-ray-UV irradiating flux is produced by a region located outside the outflow, the extension of which depends on the mass transfer. In addition, for extremely super-critical mass transfer rates, the region outside the photospheric radius of the outflow is too cold to produce a significant X-ray-UV flux: the disc-self-irradiation is therefore suppressed, but the intrinsic optical flux of the outer regions is very high. The size of the irradiating region in presence of an outflow is shown in Fig. 5.10 for all the BH masses considered. It is analogous of Fig. 4.3, but the mass transfer is normalized to Eddington, and the irradiating region to the gravitational radius. From top to bottom, the BH mass increases from 10 to 100 $M_\odot$. As already discussed in chapter 4, for each BH mass, the irradiating region ΔR increases with the mass transfer rate, reaches a peak, and then decreases. The more massive is the BH, the smaller

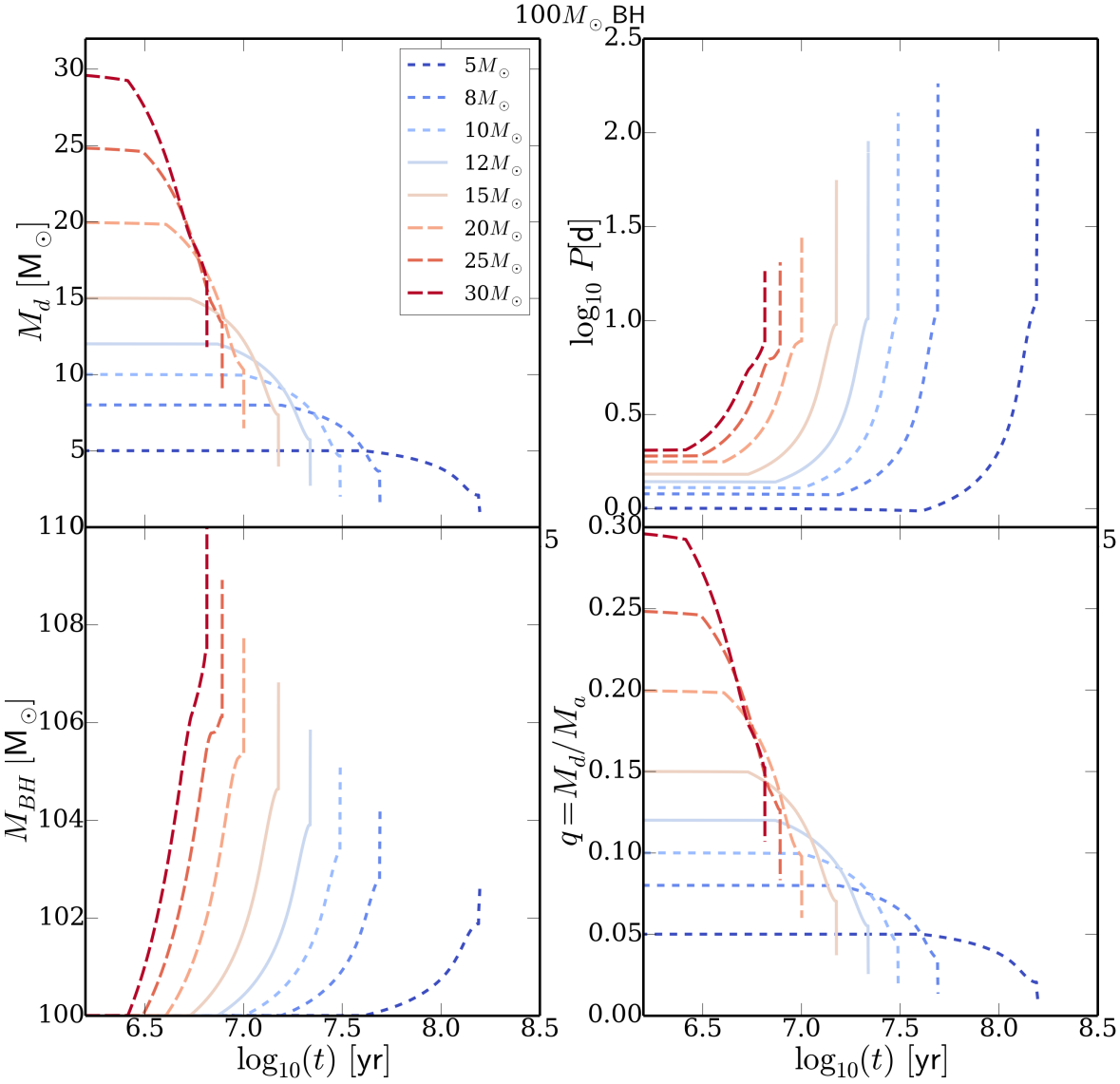

Figure 5.9: Same as Fig. 5.4 for a BH of 100 $M_\odot$.

is the value of $\dot{m}$ at which the irradiating region reaches its maximum ($\dot{m}_{max,\Delta R}$). For a 100 $M_\odot$ BH, $\log_{10}(\dot{m}_{max,\Delta R}) \sim 2.1$, while for a $10M_\odot$ BH $\log_{10}(\dot{m}_{max,\Delta R}) \sim 2.4$.

We computed the tracks on the CMD of the systems described in the previous section from the onset of RLOF to the end of their evolution, which occurs while they ascend the giant branch. The duration of the tracks depends considerably on the donor mass: the more massive is the donor, the shorter is the evolutionary path, irrespectively of the BH mass. Systems with $30M_\odot$ donor last about $10^{6.5}$ yr, while systems with a $5M_\odot$ last about $10^{8.2}$ yr. The evolutionary tracks on the CMD calculated with the MESA tracks and the emission model described in chapter 4 are shown in Fig. 5.11 ($B-V$ color and M_V magnitude) and in Fig 5.12 ($V-I$ color and M_V magnitude). They are ordered for increasing BH mass, which is fixed in each panel.

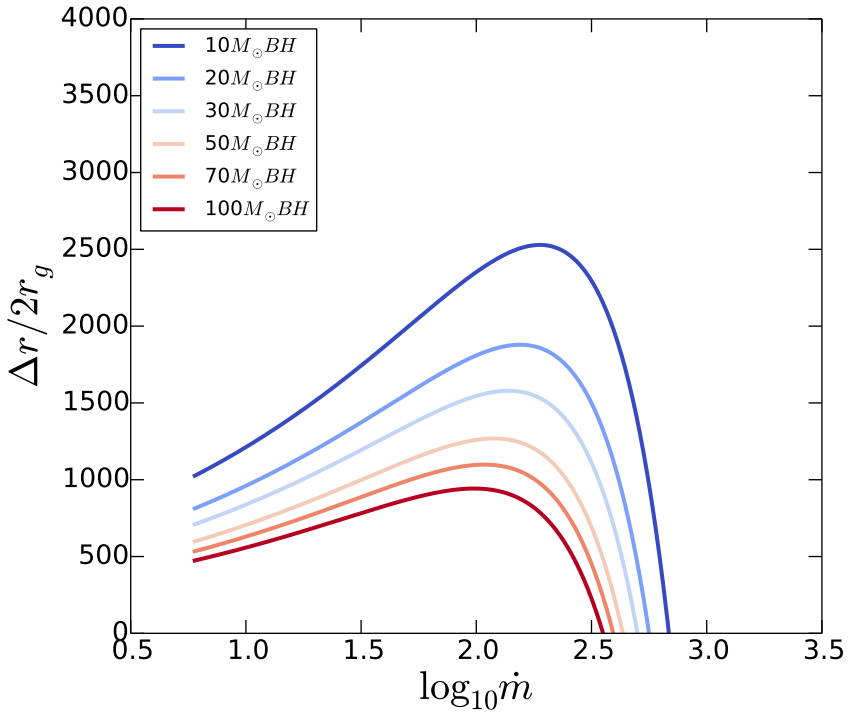

Figure 5.10: X-ray-UV irradiating region, $\Delta r = r_x - r_{ph}$, for the binary systems evolved with MESA. From top to bottom, the BH mass increases from 10 $M_\odot$ to 100 $M_\odot$.

The color code represents the magnitude of the accretion rate.
The evolutionary tracks of ULXs occupy two regions on the CMD, depending on the evolutionary stage of the donor. When the donor is on the MS and accretion is sub-critical or marginally super-critical, the tracks are blue and their M_V magnitude is limited to ~ -6. They occupy the bluer and comparatively fainter corner of the CMD, and are represented by the light-pink coloured lines in Fig. 5.11. We notice that they are similar in shape for different BH masses, the main difference being the maximum value of M_V: more massive BHs generate more luminous tracks.
When the donor ascends towards the giant branch, the properties of the evolutionary tracks are governed by the mass transfer rate, which is now super critical, as shown in Fig. 5.1. Moreover, the binary separation increases rapidly producing a more extended accretion disc, which emits a huge optical flux enhanced by self-irradiation. This evolution drives the tracks towards higher V band luminosities. The colors are initially blue because the mass transfer rate at the beginning of the giant phase is very high and the disc becomes hot. As the super-Eddington mass transfer continues, the systems widen and the accretion disc becomes more extended, driving the tracks towards redder colors. In addition, self-irradiation is essentially suppressed. However, after the peak, the mass transfer rate starts to decrease, irradiation starts to contribute again and the evolution towards the red slows down. These super-critical evolutionary stages are reproduced with the dark pink lines in Fig. 5.11. We notice that the track of the 5 $M_\odot$ donor differs from the others. In the following we will analyze this case and the behaviour of the tracks for the

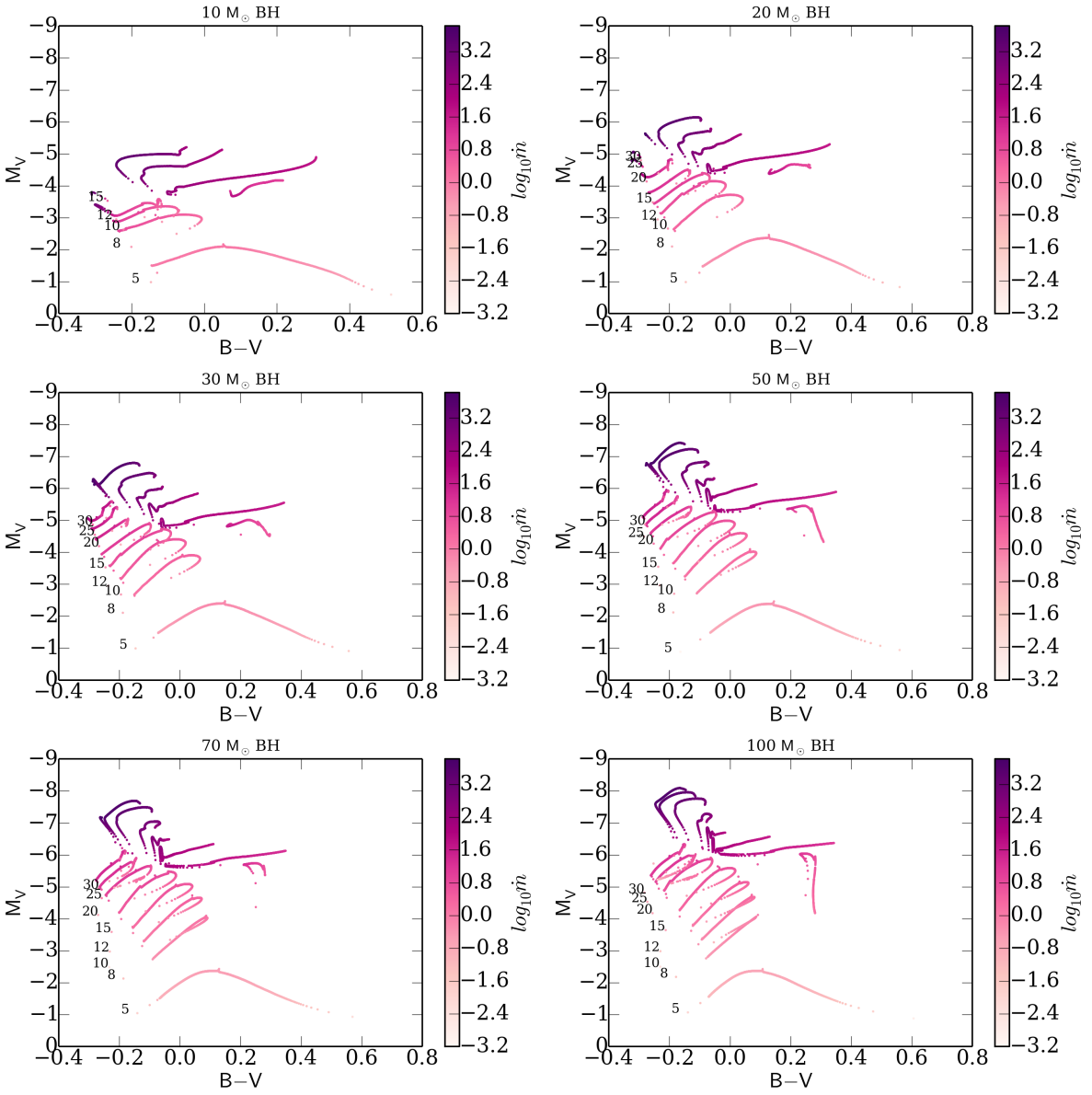

Figure 5.11: Evolutionary tracks on the color-magnitude diagram of the synthethic binary systems evolved with MESA with magnitude V and color B-V.

various BH masses in detail.

5.2.1 Systems accreting onto a 10 $M_\odot$ BH

The evolutionary tracks on the CMD for systems accreting onto a 10 $M_\odot$ BH are shown in the upper left panel of Figs. 5.11 and 5.12. We notice first that the track of the 20 $M_\odot$ donor does not appear in the CMD, while that of a 15 $M_\odot$ donor is only marginally represented. During the first contact episode during MS, these systems accrete at very high super-Eddington rates (see the upper left panel of Fig. 5.1) so that the outflow engulfs the binary and we cannot follow their

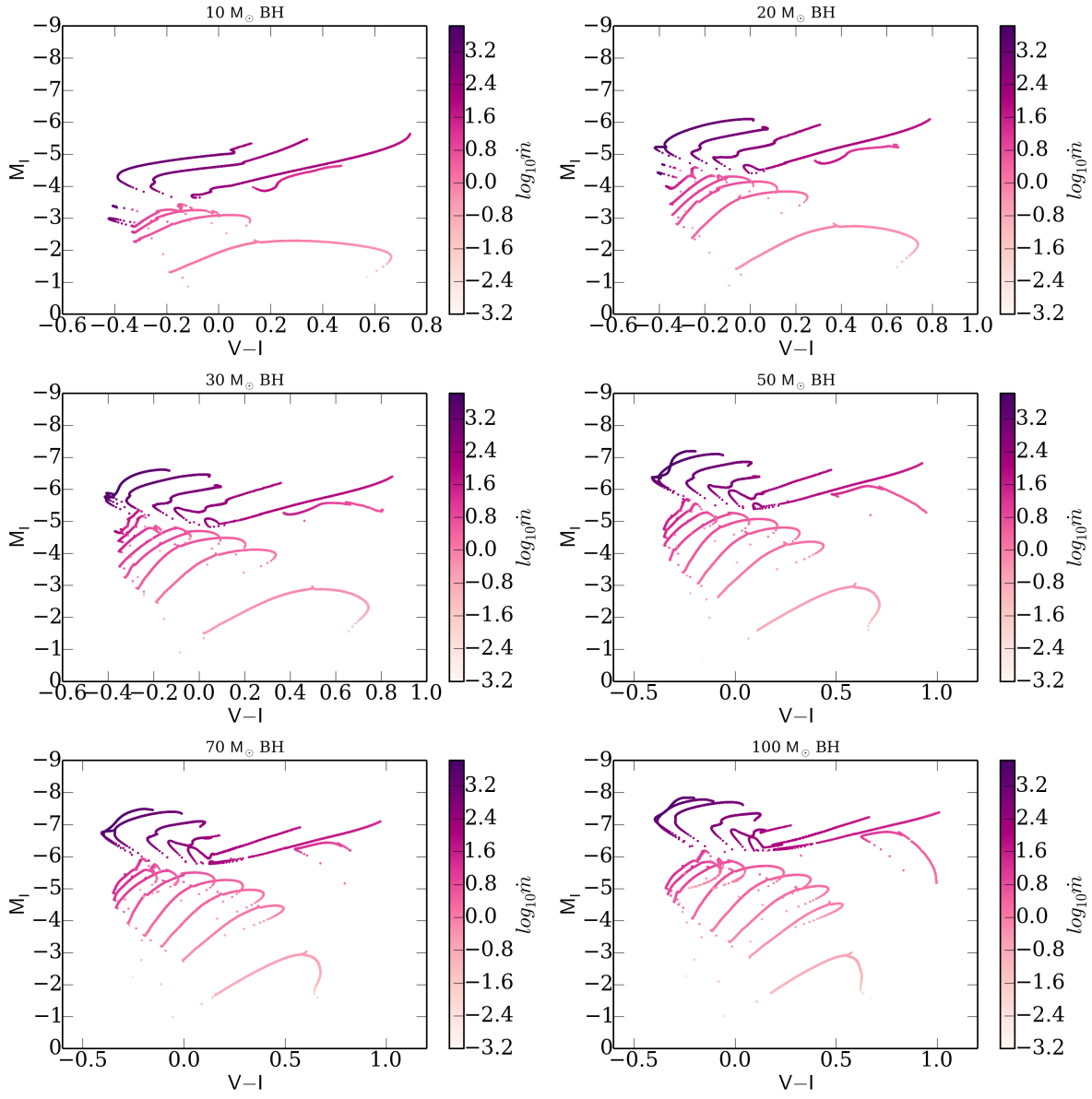

Figure 5.12: Evolutionary tracks on the color-magnitude diagram of the synthethic binary systems evolved with MESA with magnitude V and color V-I.

evolution with our model. This is similar to what happens to some of the post-MS Eggleton tracks (see chapter 4). We are left with the systems accreting from less massive donors: from 5 to 12 $M_\odot$.

When the donors are on the MS, the tracks are blue ($B - V \simeq -0.3 : -0.0$) and not very luminous ($M_V \simeq -2 : -3.5$). The 5 $M_\odot$ donor represents an exception (see below): during Main Sequence it becomes redder ($B - V$ increases up to 0.5) and its luminosity progressively decreases ($M_V \simeq -1 : -2.3$).

When the donors evolve off the MS and the mass transfer becomes super-Eddington, the evolution is similar to that described in Sec. 5.2. Colors are initially blue and then they become

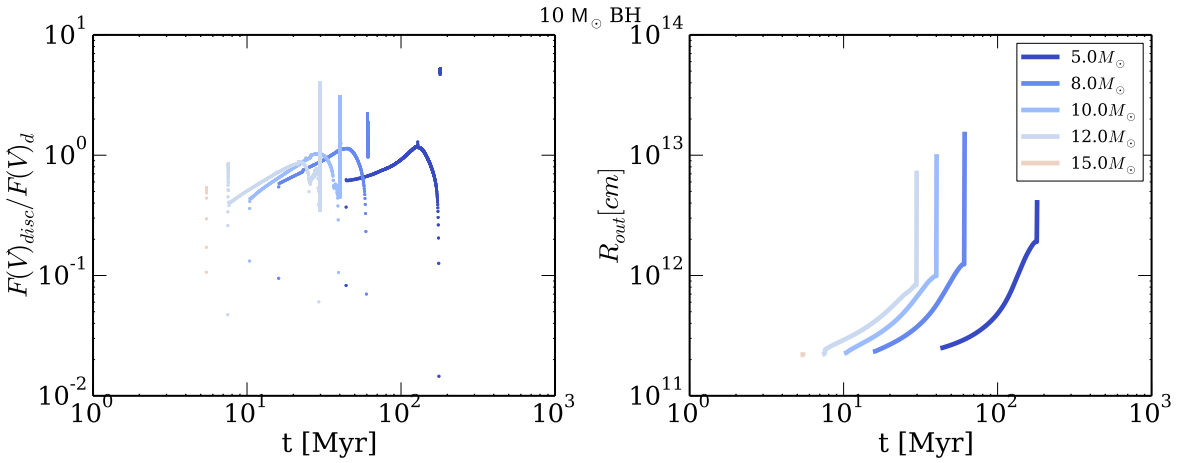

Figure 5.13: Evolution of the ratio between the flux emitted in the V filter by the disc ($F(V)_{disc}$) and that emitted by the donor star ($F(V)_d$) for the binary systems evolved with MESA accreting onto a 10 $M_\odot$ BH.

redder. The magnitudes are brighter than in MS, in the range $M_V = -3.8 : -5.2$.
Consider now the left panel of Fig. 5.13, where we show the evolution of the ratio between the flux emitted from the disc and that emitted from the donor in the V filter. During the sub-Eddington accreting phases of the MS, the donor flux overcomes that emitted by the disc but, as the evolution proceeds, the ratio of the two fluxes changes in favour of the disc flux. During the post-MS the optical flux is emitted mainly by the accretion disc (see Fig. 5.13). In the right panel we show also the evolution of the disc size. The disc radius increases with time, as expected.
As mentioned above, the 5 $M_\odot$ donor behaves in a different way. First, the radius of the disc at the TAMS is larger than that of the other systems, as shown in the left panel of fig 5.13. Moreover, the mass transfer rate is considerably sub-Eddington. These two facts imply that accretion disc is relatively cold. Also the donor star, which at TAMS is a low mass star (see Fig. 5.4), is relatively weak and cold. Therefore, the V magnitude of the system is weak and colors are red ($B - V \sim 0.5$). Given the low star and disc temperatures the system with a 5 $M_\odot$ donor is more luminous in the I band than in the V band, as it can be seen comparing Fig. 5.11 Fig. 5.12.

5.2.2 Systems accreting onto a 20 $M_\odot$ BH

Let now consider the CMDs for systems accreting onto a 20 $M_\odot$ BH (upper right panel of Figs. 5.11 and 5.12). At variance with the previous case, the tracks belonging to all the donor stars appear in the diagram. In fact, the lower value of the q ratio (Fig. 5.5) allows for a less eruptive initial mass transfer phase. We could evolve steadily the 15 $M_\odot$ donor. The track of a 20 $M_\odot$ donor is stopped only at the final stages along the giant branch. More massive donors (25 and 30 $M_\odot$) are evolved only shortly before their evolution is stopped because the outflow engulfs the binary.
The evolution of the optical properties of systems are similar to those described above for a 10

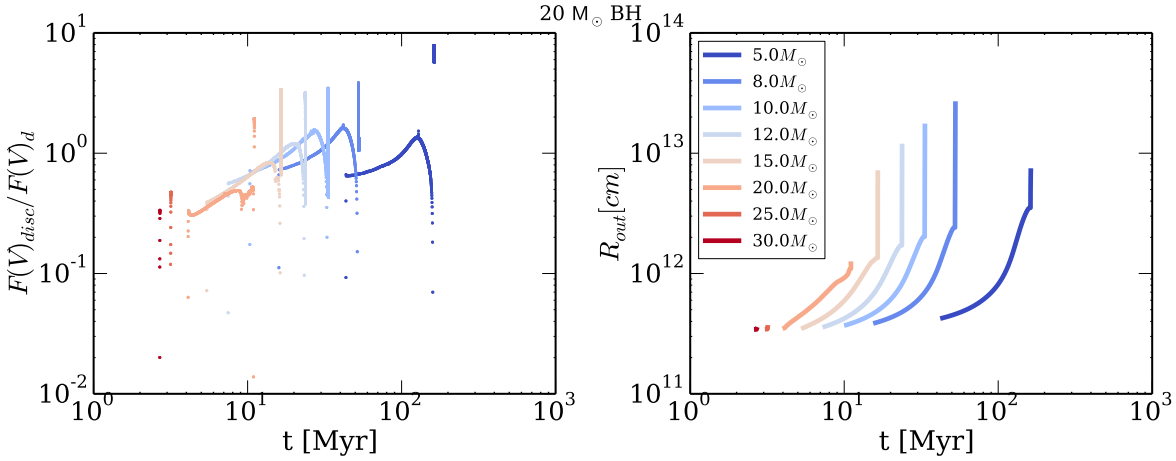

Figure 5.14: Same of Fig. 5.13 for systems accreting onto a 20 $M_\odot$ BH.

$M_\odot$ BH. The only difference is that V-I colors are redder than the those of systems accreting a 10 $M_\odot$ BH, because the discs are more extended (Fig. 5.14). During MS the 5 $M_\odot$ donor evolves differently also in this case, because it accretes at sub-Eddington rates.
For the more massive donors ($M > 10M_\odot$), the accretion in the post MS phases is characterized by blue colors and high V magnitude ($B-V \sim -0.23:0$, $M_V \sim -5, -6.3$). For lower mass donors ($M \leq 10M_\odot$), systems are comparatively redder and fainter ($B-V \simeq 0:0.6$, $V-I \sim -0.2:0.8$, $M_I \sim -4.0:-5.3$, $M_I \sim -4.5:-6.1$).

5.2.3 Systems accreting onto a 30 $M_\odot$ BH

If we steadily increase the BH mass up to 30 $M_\odot$, accretion is more stable from the beginning of the RLOF also for donors of 30 $M_\odot$ (middle left panel of Fig. 5.1) and the binary separation is larger for a given mass. This prevents the outflow to engulf the binary during MS. All the systems with donor mass $M_d \leq 25$ $M_\odot$ can be evolved completely with our model, while the system with initial donor mass $M_d = 30$ $M_\odot$ is truncated in the middle of the giant phases. During MS, the flux emitted by the disc overcomes that emitted by the star for donor less massive than $20M_\odot$ (see Fig. 5.15). The evolution of the optical emission is essentially similar to that of the 10 and 20 $M_\odot$ case.
When systems go off the MS the flux of the disc is dominant for all the systems, and the emission is controlled by super-Eddington accretion. The tracks of more massive donors remain blue, and luminous ($B-V \sim -0.:-0.05$,$V-I \sim -0.4:0.1$, $M_V = -5.1:-6.9$, $M_I \sim -5:-6.7$). Systems with less massive donors turn into redder colors and are slightly less luminous ($B-V \sim -0.1:0.4$, $V-I \sim -0.3:0.9$, $M_V = -1.5:-5.5$, $M_I \sim -4.5:-6.5$).

5.2.4 Systems accreting onto a 50 $M_\odot$ BH

Only the track with the donor of 30 $M_\odot$ is truncated because the outflow engulfs the binary. Fig. 5.16 shows that also in these systems, during MS, the flux of the donor overcomes that of the disc for the more massive donors ($M_d \geq 20$ $M_\odot$). On the contrary, the V flux for systems with less

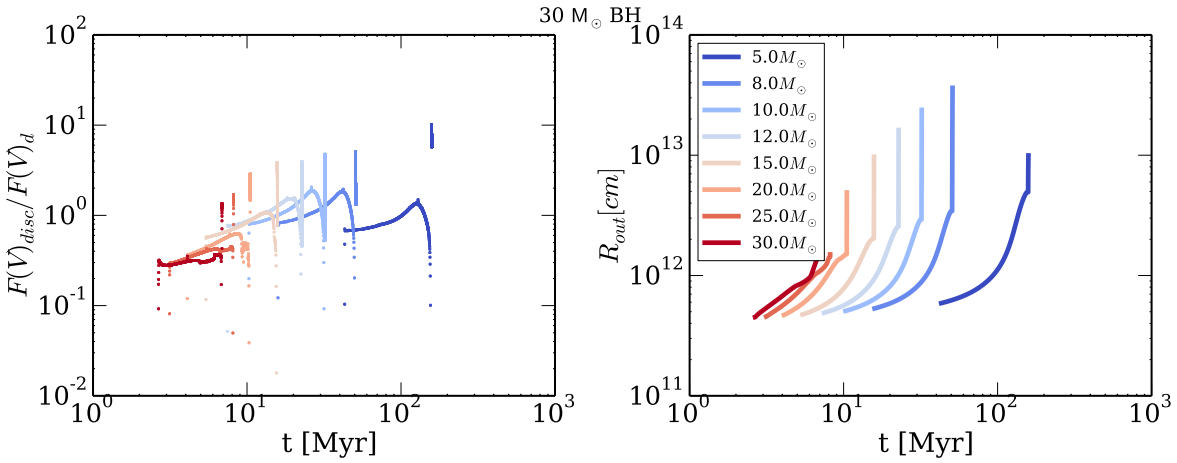

Figure 5.15: Same of Fig. 5.13 for systems accreting onto a 30 $M_\odot$ BH.

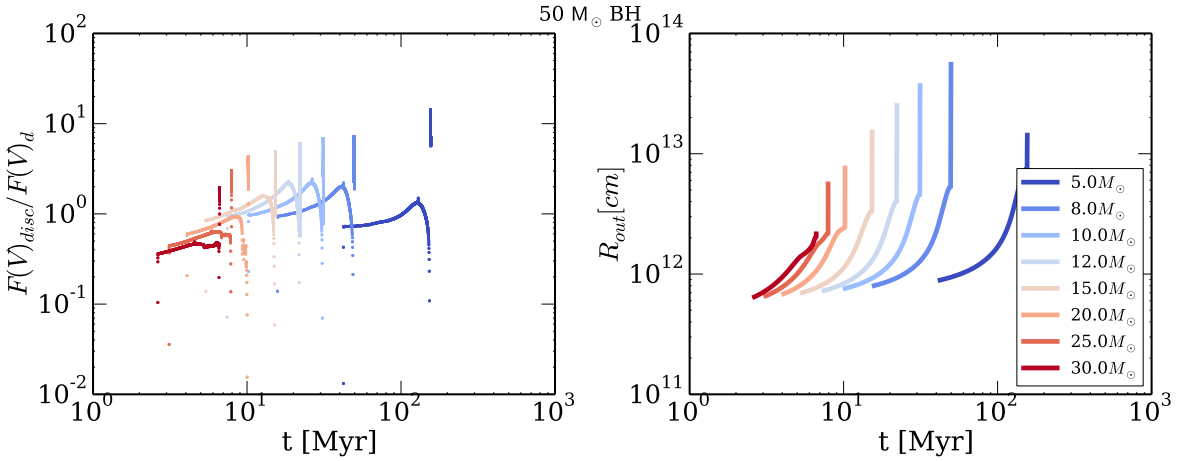

Figure 5.16: Same of Fig. 5.13 for systems accreting onto a 50 $M_\odot$ BH.

massive donors is driven by the emission of the disc. The post-MS phases, characterized also in this case by super-Eddington accretion, follows the trends that we found for the other systems. The range of colors and magnitudes of these systems during the super-Eddington accretion phases are: $B-V \sim -0.1:0.4$, $V-I \sim -0.4:1$, $M_V = -5.2:-7.5$, $M_I \sim -5.4:-7.2$

5.2.5 Systems accreting onto a 70 $M_\odot$ BH

Let now consider the systems accreting onto a 70 $M_\odot$ BH (lower left panel of Figs. 5.11 and 5.12). Their evolution on the CMDs is similar to that of the 50 $M_\odot$ BH. Also in this case, the track of the 30 $M_\odot$ donor is interrupted because the outflow becomes too extended. Figs. 5.17 shows that during MS the flux of the disc is dominant also for the systems with 20 $M_\odot$ donor. The tracks are similar to the 50 $M_\odot$ case but slightly redder, being the accretion disc larger. Magnitude and colors during MS are in the range: $B-V \sim -0.3:0.6$, $V-I \sim -0.4:0.5$, $M_V = -2.5:-6$, $M_I \sim -2.8:-5.9$, while during the post-MS phases are in the range:

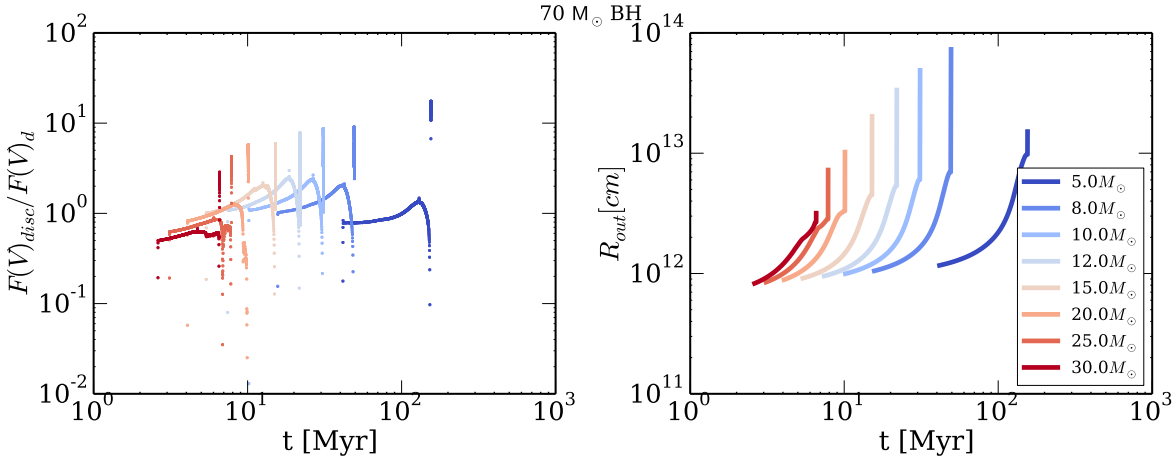

Figure 5.17: Same of Fig. 5.13 for systems accreting onto a 70 $M_\odot$ BH.

$B-V \sim -0.1:0.4$, $V-I \sim -0.4:1.0$, $M_V = -5.5:-7.8$, $M_I \sim -5.8:-7.7$.

5.2.6 Systems accreting onto a 100 $M_\odot$ BH

We finish by describing systems accreting onto a 100 $M_\odot$ BH, which is the maximum BH mass considered in this work (lower right panels in Figs. 5.11 and 5.12). Even for the high mass

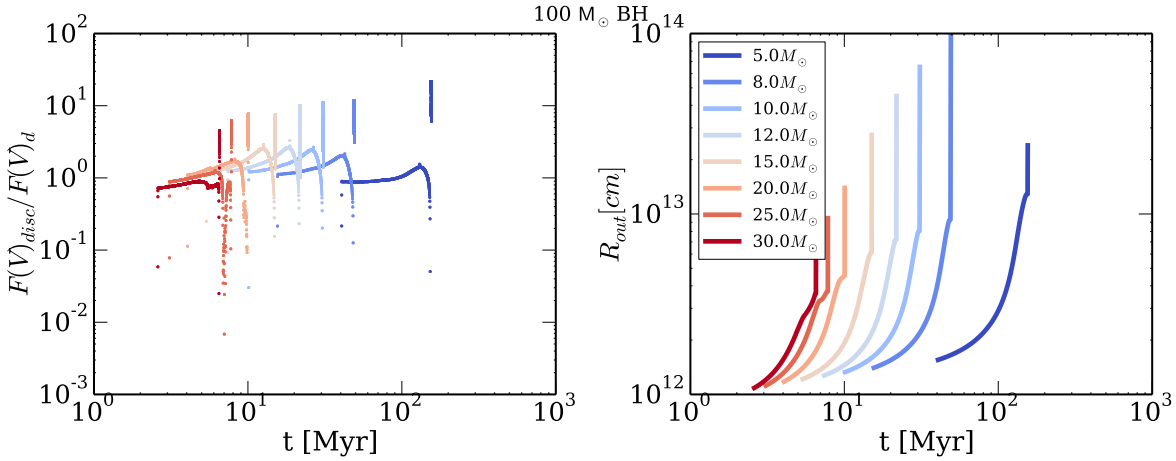

Figure 5.18: Same of Fig. 5.13 for systems accreting onto a 100 $M_\odot$ BH.

transfer rate which characterizes the initial evolution of a 30 $M_\odot$ donor, see Fig. 5.1, the outflow does not engulf the system. We can evolve it up to the moment in which the donor starts He-burning in the nucleus, which is the endpoint of the evolutionary tracks we evolved with MESA. The behaviour is similar to that of the systems with 50 or 70 $M_\odot$ donor. Only the post-MS stages of evolution of the 5 $M_\odot$ donor are different as the accretion disc is very extended (see Fig. 5.18) and the donor mass extremely low (Fig. 5.9). The systems becomes very red and the luminosity in the V band decreases significantly. Magnitude and colors, during MS are in the

range: $B-V \sim -0.3 : -0.1$, $V-I \sim -0.45 : 0.5$, $M_V = -2.5 : -6.3$, $M_I \sim -2.3 : -6.1$, while during the post-MS phases are in the range: $B-V \sim -0.25 : -0.1$, $V-I \sim -0.4 : 0.1$, $M_V = -6 : -8.2$, $M_I \sim -6.1 : -7.9$.

5.3 Conclusions

We calculated a new grid of evolutionary tracks of ULX binary systems with the MESA code and found that they occupy two regions on the CMD, depending on the evolutionary stage of the donor.

When the donor is on the MS and accretion is sub-critical or marginally super-critical, the tracks are blue and their M_V magnitude is limited up to ~ -6. They occupy the bluer and comparatively fainter corner of the CMD. We notice that they are similar in shape for different BH masses, the main difference being the maximum value of MV: more massive BHs generate more luminous tracks.

When the donor is ascending towards the Giant Branch, the properties of the evolutionary tracks are governed by the mass transfer rate, which is now super critical. Moreover, the binary separation increases rapidly producing a more extended accretion disc, which emits a very large flux in the optical band, eventually enhanced by self-irradiation. This evolution drives the tracks towards higher V band luminosities. The colors are initially blue because the mass transfer rate at the beginning of the Giant phase is very high and the disc becomes hot. As the super-Eddington mass transfer continues, the systems widens and the accretion disc becomes more extended, driving the tracks towards redder colors. In addition, self-irradiation is essentially suppressed. After the peak, the mass transfer rate starts to decrease, irradiation starts to contribute again and the evolution towards the red slows down.

Chapter 6

Modelling the Multiwavelength Emission of ULXs

6.1 Introduction

This chapter is dedicated to the comparison of our model, applied to the new MESA evolutionary tracks, with the optical and X-ray data of a few nearby ULXs. We constrain the model parameters using the photometric data and X-ray spectra of the sources. In chapter 4 we concluded that the emission of the disc plus outflow alone cannot fully reproduce the observed data, because the X-ray spectrum at the highest energies is too soft and cannot properly describe the ULXs spectra. Observations show that ULX spectra require the existence of an optically thick and cool corona which is believed to cover the innermost regions of the disc (e.g. Gladstone et al. 2009, Pintore and Zampieri 2012, Sutton et al. 2013b). Therefore we added such component to our model.

6.2 Comptonization from an optically thick corona

In order to model the hard X-ray emission, we added to our model the contribution of a comptonizing corona which covers the innermost regions of the disc. We approximate the corona with a sphere which extends up to the the radius where the outflow becomes optically thick. Therefore its radius is:

$$r_c = r_{ph,in}, \tag{6.1}$$

where $r_{ph,in}$ is the inner radius of the outflow (see chapter 4). Following the observational evidence gathered from the X-ray spectral analysis (e.g. Pintore and Zampieri 2012, Pintore et al. 2014), we assume that the Compton parameter in the corona is significantly larger than unity and that Comptonization is saturated. In these assumptions, the high energy part of the spectrum can be approximated with a Wien (Rybicki and Lightman, 1986):

$$I_\nu^W = \frac{2h\nu^3}{c^2} e^{-\alpha} e^{-h\nu/kT_c} \tag{6.2}$$

where the factor $e^{-\alpha}$ is related to the rate at which the photons are produced and T_c is the electron temperature of the corona.
The corona is assumed to cover only the inner regions of the disc. Therefore, since Compton scattering conserves the photon number, the value of the factor $e^{-\alpha}$ is determined from the relation:

$$N_{ph}^{W} = N_{ph}^{d}, \tag{6.3}$$

where N_{ph}^{d} is the number of photons per unit time emitted from the disc which, for an observer at distance D, takes the form:

$$N_{ph}^{d} = \pi \int_{0}^{\infty} \int_{r_{in}}^{r_{ph,in}} \left(\frac{I_{\nu}^{d}}{h\nu}\right) \frac{2rD^2}{(r^2+D^2)^2} dr d\nu, \tag{6.4}$$

while

$$N_{ph}^{W} = \pi \frac{r_c^2}{r_c^2+D^2} \int_{0}^{\infty} \frac{I_{\nu}^{W}}{h\nu} d\nu \tag{6.5}$$

is the number of photons which is emitted per unit time from the corona. In the following, we consider three reference electron temperatures: 1.2, 1.5 and 3 keV. These temperatures sample the typical range of temperatures inferred from modelling the observed ULXs spectra (Pintore et al., 2014).

6.3 Results

With the addition of an optically thick Comptonizing corona, our model can reproduce the Multiwavelength emission of ULXs in an acceptable way, and can be effectively used to constrain the properties of ULXs. For each source analyzed in this work, we proceed according to the following steps:

1. **Comparison with the CMD diagram**: the first step is to search the synthetic evolutionary tracks that intersect the observed data points of a ULX on the CMD (considering their errorbars). We search for intersections, when possible, in more than two colors, which provides an additional constrain.

2. **Age selection:** the comparison with the evolutionary tracks typically produces several intersections. Therefore we select the model using an additional constrain, which is the age of the ULX inferred from the population study on the host environment.

3. **Search for the best fit of the multiwavelength SED:** finally, after having selected the intersections which correspond to the age of the ULXs, we compute the synthetic optical-through-X-ray SED of the systems considering three electron temperature of the optically thick corona: $kT_c = 1.2$, 1.5 and 3 keV. The best fit solutions are found applying a chi-square test to the data-model comparison for each adopted electron temperature, considering as free parameter the age of the system. The X-ray spectra used for the analysis in this chapter are taken from the literature or were kindly provided by Fabio Pintore and Anna Wolter.

6.3.1 NGC 1313 X-2

In Chap. 4, we studied the optical counterpart of NGC 1313 X-2 and found that it is better reproduced with a system containing a BH of $\sim 20\ M_{\odot}$ accreting above Eddington. Here we show the results obtained calculating the emission properties of binary systems evolved with the MESA code applied to this source. Moreover, we constrained further the data-model comparison using the entire SED of NGC 1313 X-2, including the X-rays. Also in this case we adopted a distance of of 4.07 ± 0.22 Mpc (Grisé et al. 2008) and an optical extinction $E(B-V) = 0.13$ (Tao et al. 2011). For the optical magnitude and colors we adopted the same values reported in 4 : F555W $= -4.88 \pm 0.06$, F450W-F555W $= -0.18 \pm 0.1$. Fig. 6.1 shows the intersection of X-2 with the evolutionary tracks on the CMD calculated using the F555W and F435W filters. The optical counterpart of X-2 is intersected by : a) the track of a BH of 10 $M_{\odot}$ accreting from a donor with initial mass of 12 $M_{\odot}$ in the H-shell burning phase, b) the track of a 20 $M_{\odot}$ BH accreting from a donor with initial mass of 20 $M_{\odot}$ at terminal age main sequence (TAMS), c) the tracks of donors with initial mass of 15, 20 and 25 $M_{\odot}$ in the H-burning phase which accrete matter onto a BH of 30 $M_{\odot}$, d) the tracks of donors of initial mass of 15, 20 and 25 $M_{\odot}$ that accrete onto a 50 $M_{\odot}$ BH at the beginning of the MS. Finally; e-f) the tracks of donors with M $> 15\ M_{\odot}$ during MS accreting onto BHs of 70 and 100 $M_{\odot}$.
Considering the constraint of the age of the parent stellar association ($\sim$ 20 Myrs; Grisé et al. 2008), we rule out case (a), (e), and (f) because the system is either too young or too old. W We are left with systems accreting onto a 20, 30 or 50 $M_{\odot}$ BH.
After selecting the systems which fit the optical data and have the corrected age, we further constrain them comparing their optical-through X-ray SED with that of NGC 1313 X-2. For the X-ray data we consider four Epochs: 23 Aug. 2004, 16/17 Oct. 2006 (Pintore and Zampieri 2011, 2012), 16 and 22 Dec. 2012 (Bachetti et al. 2013). All of them have been fitted with a *diskpbb*[1]+*compTT*[2] model. In these four Epochs, X-2 shows pronounced variability. Considering that optical and X-ray measurements are not simultaneous, we performed the fit of the SED taking into account the observed X-ray variability of the source. We then rebinned the X-ray spectrum in 8 energy bins, calculating for each of them the mean value and taking as an estimate of the variability interval the standard deviation. The latter is also considered the 'error' in calculating the χ^2.
We then compared the synthetic SED calculated at the time of intersections of systems accreting onto a 20, 30 and 50 $M_{\odot}$ BH with the observed optical-through-X-ray SED of NGC 1313 X-2. We search for the best fitting SEDs with the χ^2 method adopting as free parameters the age and the electron temperature of the corona. The best-fitting model found minimizing the χ^2 method is shown in Tab. 6.1. While systems with a donor and BH of initial mass of 15 $M_{\odot}$ and 30 $M_{\odot}$, respectively, provide acceptable fits, X-2 is best reproduced with a system accreting marginally above Eddington onto a BH with actual mass of 25 $M_{\odot}$ from a donor with present mass of about 9 $M_{\odot}$ at TAMS. The systems is aged $\sim$ 10 Myrs and evolved from a donor with

[1]In the X-ray spectral fitting package XSPEC the *diskpbb* model is a multi-temperature blackbody disc model, where the local disc temperature T(r) is proportional to r^{-p}, where p is a free parameter (see Mineshige et al. 1994).

[2]In the X-ray spectral fitting package XSPEC the *compTT* model is an analytic model describing Comptonization of a soft photon input in a hot plasma, developed by Titarchuk (see Titarchuk 1994).

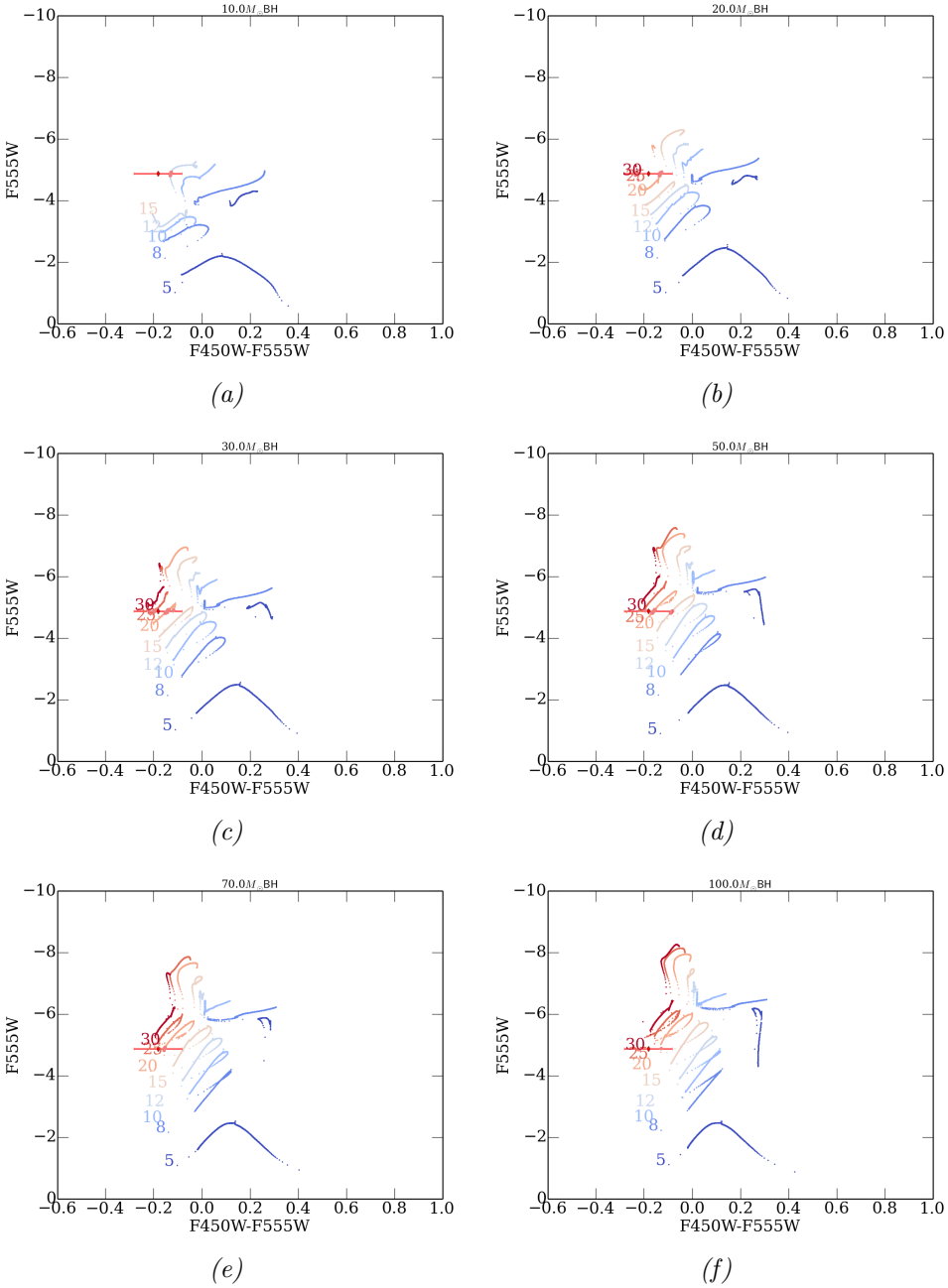

Figure 6.1: Comparison of the optical counterpart of NGC1313 X-2 with the evolutionary tracks that we calculated using the MESA code. For the CMD we used the F555W magnitude and F450W-F555W color. From panels a through f the BH mass increases from 10 to 100 $M_\odot$.

NGC 1313 X-2								
Best fit model for systems with $M_{d,i} = 20\ M_\odot$ and $M_{BH,i} = 20\ M_\odot$								
kT_e (keV)	t (Myr)	$M_d(t)$ ($M_\odot$)	$M_{BH}(t)$ ($M_\odot$)	$\dot{m}$	P (d)	L_{tot} (erg/s)	χ^2	d.o.f.
1.2	10.5	9.84	25.96	12.2	$\sim$ 4	$6.1 \cdot 10^{39}$	11.81	12
1.5	10.5	9.84	25.96	12.2	~ 4	$6.7 \cdot 10^{39}$	11.99	12
3.0	10.5	9.88	25.94	12.2	~ 4	$9.3 \cdot 10^{39}$	12.15	12
Best fit model for systems with $M_{d,i} = 15\ M_\odot$ and $M_{BH,i} = 30\ M_\odot$								
1.2	13	8.44	~ 34	10.6	$\sim$ 4.8	$7.9 \cdot 10^{39}$	28.25	12
1.5	13	8.44	~ 34	10.6	~ 4.8	$8.7 \cdot 10^{39}$	27.43	12
3.0	13	8.37	~ 34	10.4	~ 4.8	$1.2 \cdot 10^{40}$	27.82	12

Table 6.1: Best fit models found minimizing the χ^2 method for NGC 1313 X-2. Reported are the significant parameters of the best-fit intersections.

initial mass of 20 $M_\odot$ and a BH of initial mass of 20 $M_\odot$. The orbital period at intersection is ~ 4 days and the total luminosity is in the range of $5 \cdot 10^{39} - 1.4 \cdot 10^{40} erg \cdot s^{-1}$.
The luminosity is in agreement with the bolometric luminosity inferred from X-ray observations ($1.0 \cdot 10^{39} - 3.0 \cdot 10^{40} erg\ s^{-1}$,see Pintore and Zampieri 2012), while the orbital period is slightly smaller than the measured value: P $= 6.12 \pm 0.16$ d (for significant X-ray irradiation;Liu et al. 2009; Zampieri et al. 2012. We estimated an uncertainty of ~ 0.2 days averaging among the intersections on the CMD bounded by the error bars on magnitude and colors. We note that, although this is formally not consistent with the observed period within the errorbars, the agreement could be improved in the future either making the grid of computed models tighter or varying some other parameters of the model (such as, e.g., the efficiency in accelerating the outflow or the starting time of the RLOF phase) that, at present, have been kept fixed. We note also that, while formally acceptable, the fits with a 'hot' corona ($T > 3keV$) show a high energy bump of which there is no evidence in *NuSTAR* data (Bachetti et al., 2013) and would also leave significantly structured residual at lower energies, again not observed. The fit with lower coronal temperatures are consistent with the so called 'very thick corona state' of Pintore and Zampieri (2012). The findings reported here confirm those reported in Chap 4 (Ambrosi and Zampieri, 2018), based on the comparison of the tracks on the CMD and on the age selection criterion (see Figs. 6.2 and 6.3).

6.3.2 NGC 4559 X-7

As reported in chapter 4, we assume a Galactic extinction $E(B-V) = 0.018$ and a distance of 10 Mpc (Tao et al., 2011; Soria et al., 2005). We consider the average of the magnitudes and colors taken from two measurements (Tao et al., 2011) : F555W $= -7.05 \pm 0.08$ and F555W-F814W $= -0.11 \pm 0.13$. We take as reference age for this source the age of the parent population: ~ 20 Myrs (Soria et al., 2005). In Fig. 6.4 we compare the position of the optical counterpart of X-7 with the computed evolutionary tracks of ULXs. Panels a) b) and c) show that X-7 is too luminous to be a binary accreting onto BHs with mass up to 30 $M_\odot$. Conversely, accretion onto more massive BHs is possible: X-7 intersects the tracks of donors with initial mass of 15

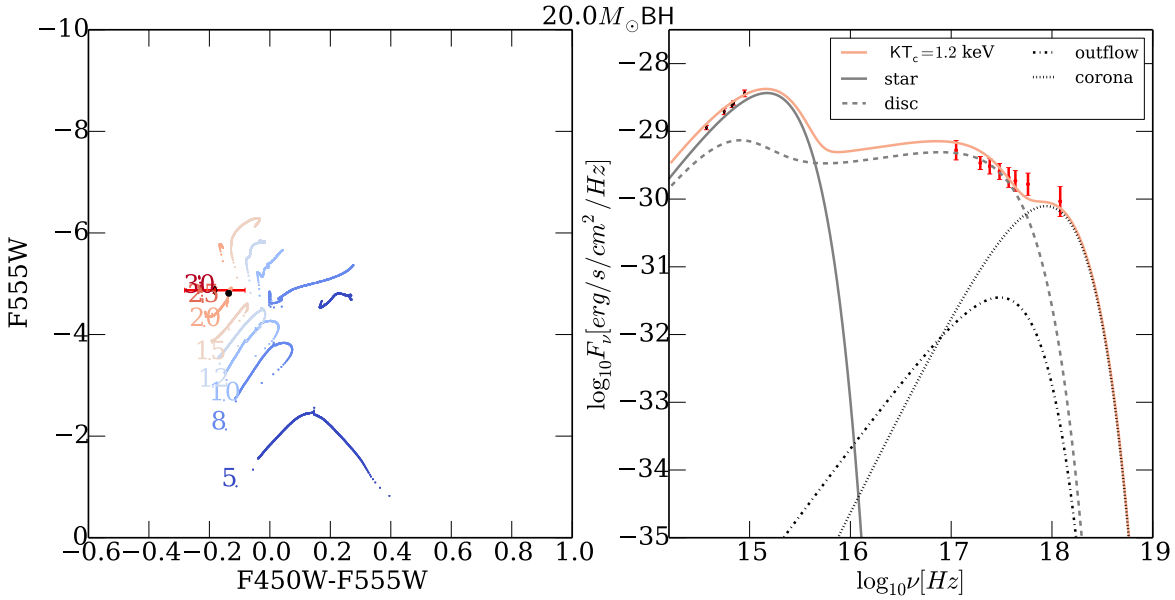

Figure 6.2: Intersection of the best-fit solution among the evolutionary tracks accreting onto a 20$M_\odot$ BH with the optical counterpart of NGC 1313 X-2 (left),total Spectral Energy Distribution for the best fit solution together with those of the single components (right).

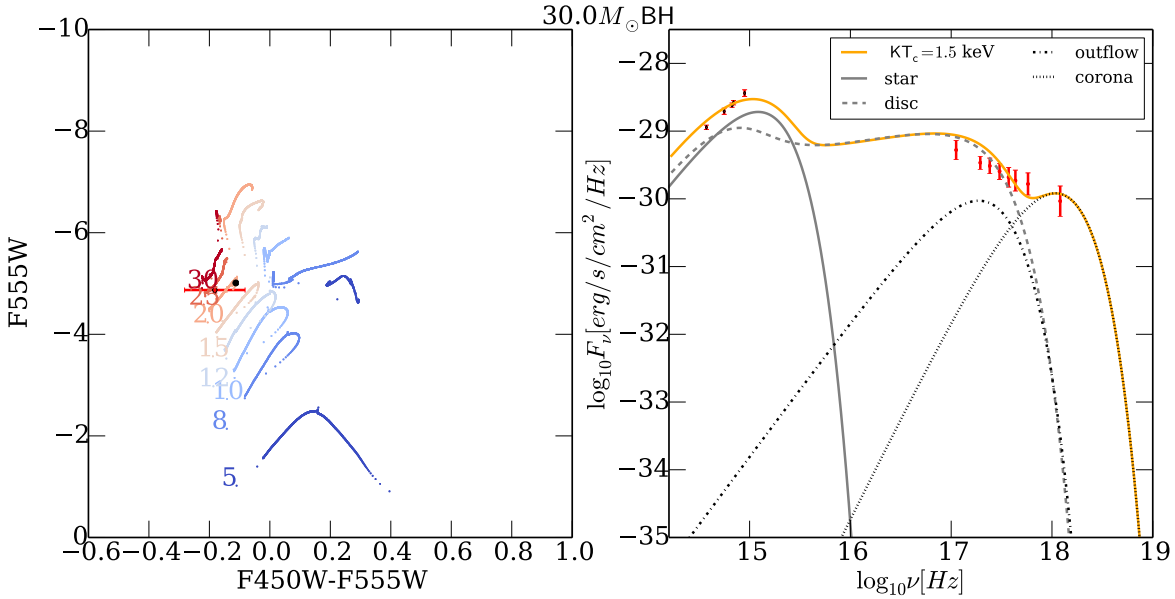

Figure 6.3: Same of Fig. 6.2 but for the best fit solution of NGC 1313 X-2 for systems accreting onto 30$M_\odot$ BH.

$M_\odot$ accreting onto a 50 and 70 $M_\odot$ BH during the H-burning shell phase (panels d and e) and tracks of evolved donors with initial mass of 12, 15 and 20 $M_\odot$ accreting onto a 100 $M_\odot$ BH. The age of all tracks of X-7 at intersection ($\sim$ 15 Myr) are in agreement with that estimated from its stellar environment ($\sim$ 20 Myrs, Soria et al. 2005). We then fitted their multiwavelength SEDs to further constrain them. We consider the *XMM-Newton* observation of Epoch 2 May

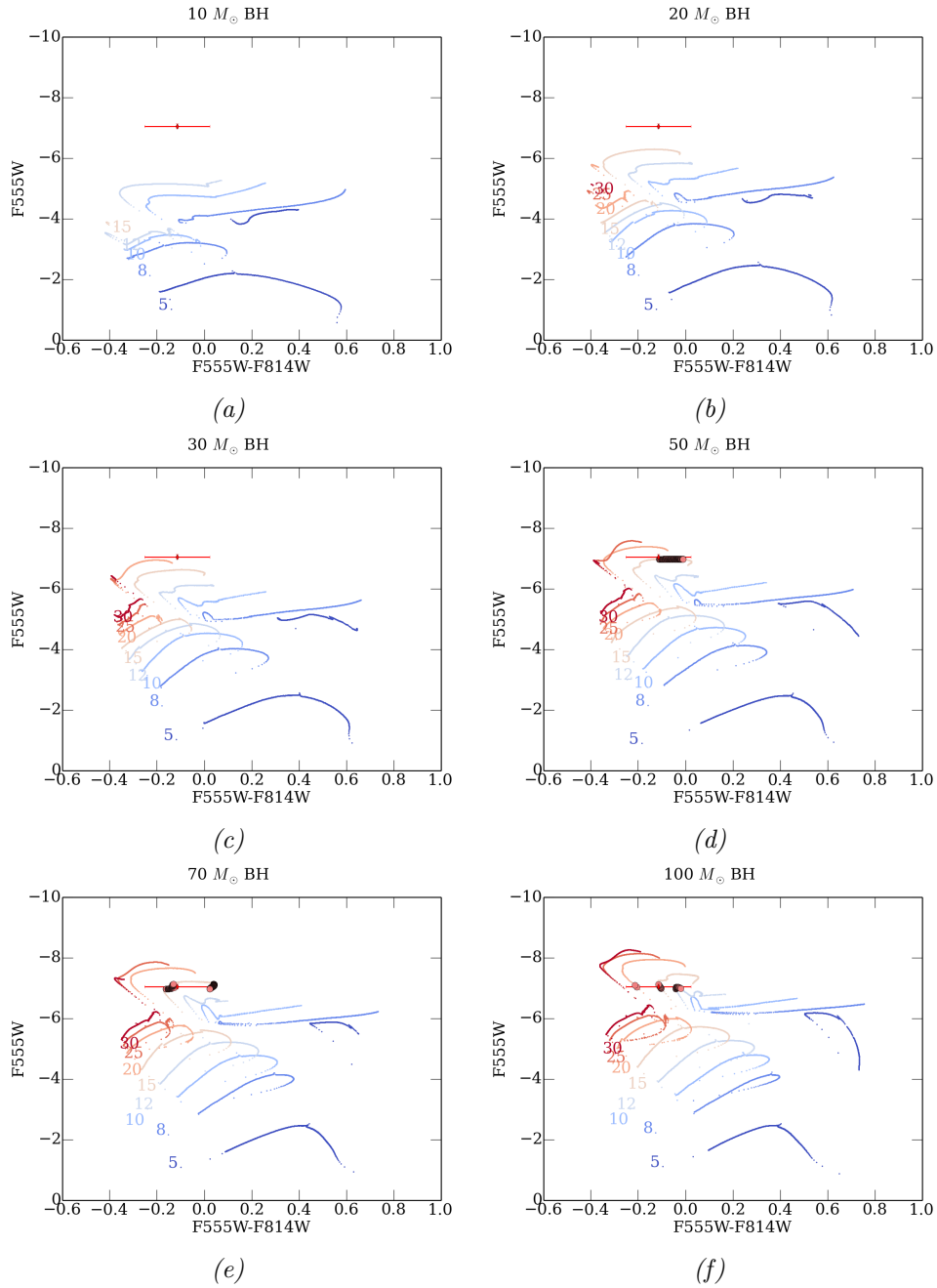

Figure 6.4: Comparison of the optical counterpart of NGC 4559 X-7 with the evolutionary tracks that we evolved in this study in the CMD with F555W magnitude and color F555W-F814W. From panels a-f the BH mass increases from 10 to 100 $M_\odot$.

2003 considering a flux variability interval of a factor of 2. Table 6.2 shows the best fitting evolutionary tracks based on the χ^2 statistic: X-7 is reproduced with systems having donor of actual mass in the range 5-6 $M_\odot$ accreting onto massive BHs with masses of ~ 56 or ~ 75 $M_\odot$. From figs. 6.5 and 6.6 we see that the fits are formally acceptable, but those with temperature of the corona > 1.5 keV are slightly worse and would leave clear residuals in the fit not present

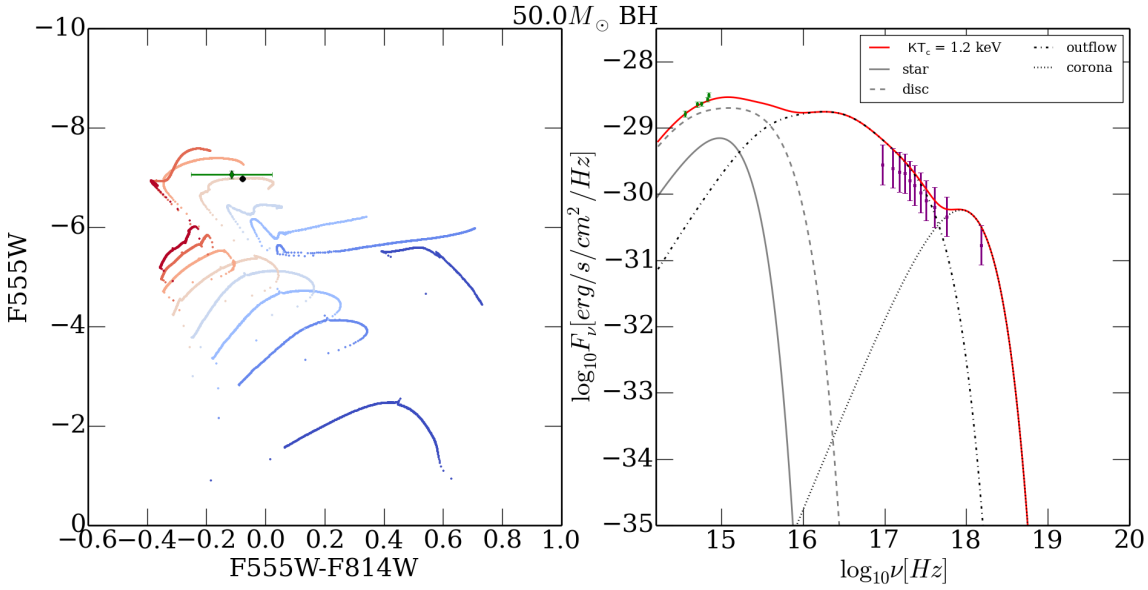

Figure 6.5: Intersection of the best-fit solution among the evolutionary tracks accreting onto a $50M_\odot$ BH with the optical counterpart of NGC 4559 X-7 (left),total Spectral Energy Distribution for the best fit solution together with those of the single components (right).

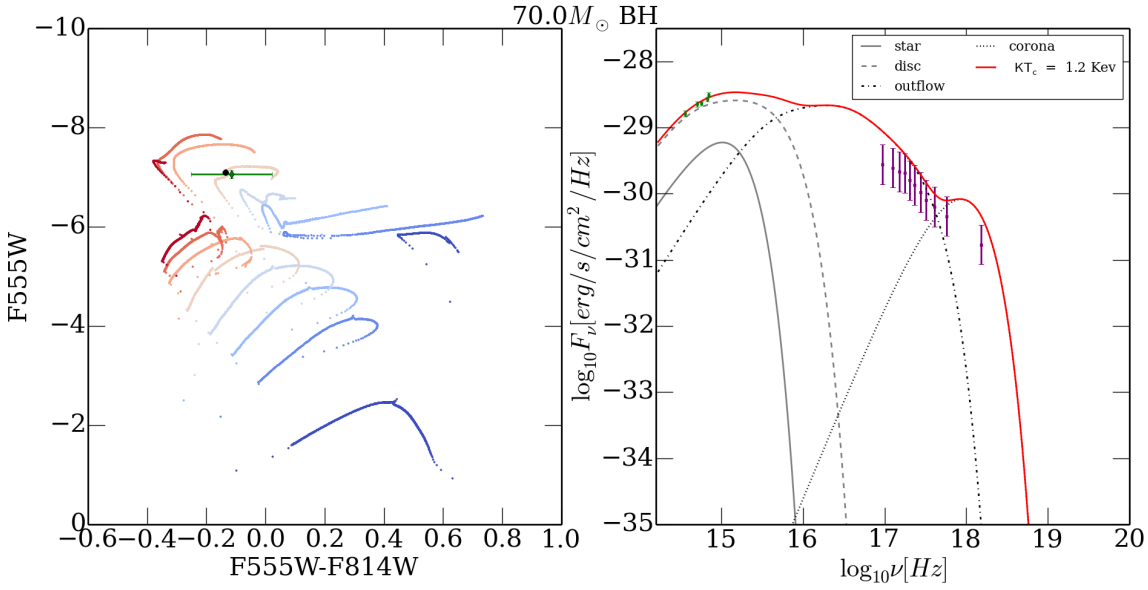

Figure 6.6: Same as Fig. 6.5 for a BH of 70 $M_\odot$

NGC 4559 X-7								
Best fit model for systems with $M_{d,i} = 15\ M_\odot$ and $M_{BH,i} = 50\ M_\odot$								
kT_e(keV)	t (Myr)	$M_d(t)$ $(M_\odot)$	$M_{BH}(t)$ $(M_\odot)$	$\dot{m}$	P (d)	$L_{tot}(erg/s)$	χ^2	d.o.f.
1.2	15.3	5.5	55.85	$\sim 1.110^3$	~ 18	$3.234 \cdot 10^{40}$	17.927	15
1.5	15.3	5.5	55.85	$\sim 1.110^3$	~ 18	$3.455 \cdot 10^{40}$	19.964	15
3.0	15.3	5.5	55.85	$\sim 1.110^3$	~ 18	$4.55 \cdot 10^{40}$	20.022	15
Best fit model for systems with $M_{d,i} = 15\ M_\odot$ and $M_{BH,i} = 70\ M_\odot$								
1.2	15.1	6.6	75.13	895	12	$4.28 \cdot 10^{40}$	22.071	15
1.5	15.1	6.6	75.13	895	12	$4.59 \cdot 10^{40}$	26.955	15
3.0	15.1	6.6	75.13	895	12	$6.17 \cdot 10^{40}$	26.493	15

Table 6.2: Best fit models found minimizing the χ^2 method for NGC 4559 X-7. Reported are the significant parameters of the best-fit intersections.

in the data. In addition, the observed X-ray luminosity of X-7 is $\sim 2 \cdot 10^{40} erg/s$ Soria et al. (2005), is better in agreement with the fit with lower corona temperature (Tab. 6.2). Therefore we conclude that X-7 is a system accreting at largely super-critical rates onto massive BHs from donors which are ascending along the Giant Branch and, having lost the moss of their mass during during the MS, are now less massive, with masses in the range 5-6 $M_\odot$. The orbital period of these systems is quite long because the donor is evolved and has lost a large amount of mass.

Figs. 6.5 and 6.6 show that at these stages of the evolution, optical emission is dominated by the outer accretion disc, which reaches a very high optical luminosity because of the high value of the mass transfer rate (dashed black line). Moreover, also the outflow emits a considerable flux, because it is very extended.

6.3.3 NGC 5204 X-1

NGC 5204 X-1 is located in the spiral galaxy NGC 5204. Its X-ray luminosity has an average value of $3 \cdot 10^{39} erg \cdot s^{-1}$, and it is found to vary in 10 years by $\sim 50\%$ (Liu et al., 2004). It is thought to reside in a young stellar cluster with age $< 10 Myr$ (Goad et al., 2002). Among the data collected by Tao et al. (2011), we will consider the average values of those taken in August 2008: F555W $= -5.646 \pm 0.055$ and F450W $= -5.848 \pm 0.027$ adopting a distance of 4.3 Mpc and galactic extinction $E(B-V) = 0.013$.

Panel a of Fig. 6.7 shows that accretion onto a 10 $M_\odot$ BH can be ruled out. On the contrary, the optical counterpart of NGC 5204 X-1 is intersected by: b) the tracks of donors with initial mass of 20 and 25 $M_\odot$ accreting onto a 20 $M_\odot$ BH at super-critical rates while the donor is ascending the Giant Branch, c) the track of a 20 $M_\odot$ donor accreting onto a 30 $M_\odot$ BH in the first stages of its H-shell burning phase, or the track of a donor with initial mass of 30 $M_\odot$ near the TAMS, d) the tracks of donors with initial mass 25 and 30 $M_\odot$ accreting onto BHs of 50, 70 and 100 $M_\odot$ during Main Sequence. These three intersections differ in the evolutionary stages at which they occur: the more massive is the BH, the younger is the age of a system with the same initial donor mass and magnitude, as we discussed in the previous chapter.

Constraining the tracks with the very young age of the parent population does not rule out a

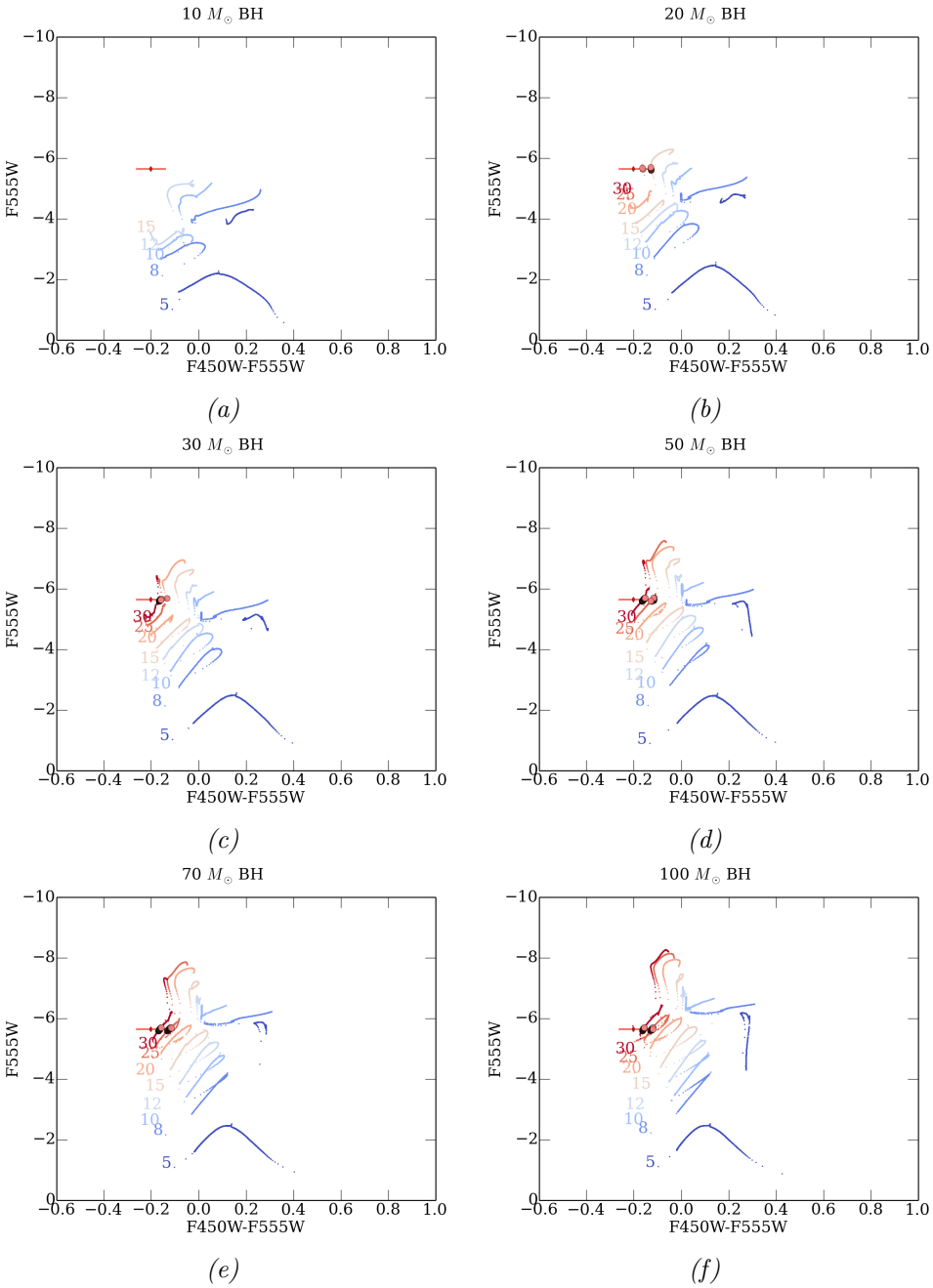

Figure 6.7: Comparison of the optical counterpart of NGC 5204 X-1 with the evolutionary tracks that we evolved in this study in the CMD with magnitude F555W and color F450W-F555W. From panels a-f the BH mass increases from 10 to 100 $M_\odot$.

large number of models, because the intersections are with tracks of very massive donors, whose evolution is very fast. We could rule out the tracks of donors with initial mass of 25 $M_\odot$ which accrete onto BHs of 20 and 30 $M_\odot$. We calculated the SED for all the other intersections and searched for the models that best fit our data, using only one X-ray observation and assuming an X-ray flux variability of 50% (Liu et al., 2004) .

NGC 5204 X-1								
Best fit model for systems with $M_{d,i} = 30\ M_\odot$ and $M_{BH,i} = 30\ M_\odot$								
kT_e(keV)	t (Myr)	$M_d(t)$ $(M_\odot)$	$M_{BH}(t)$ $(M_\odot)$	$\dot{m}$	P (d)	$L_{tot}(erg/s)$	χ^2	d.o.f.
1.2	6.8	13.9	39	6.4	5.5	$8.20 \cdot 10^{39}$	106.487	21
1.5	6.8	13.9	39	6.4	5.5	$9.04 \cdot 10^{39}$	108.927	21
3.0	6.8	13.9	39	6.4	5.5	$1.31 \cdot 10^{40}$	317.599	21

Table 6.3: Best fit models found minimizing the χ^2 method for NGC 5204 X-1. Reported are the significant parameters of the best-fit intersections.

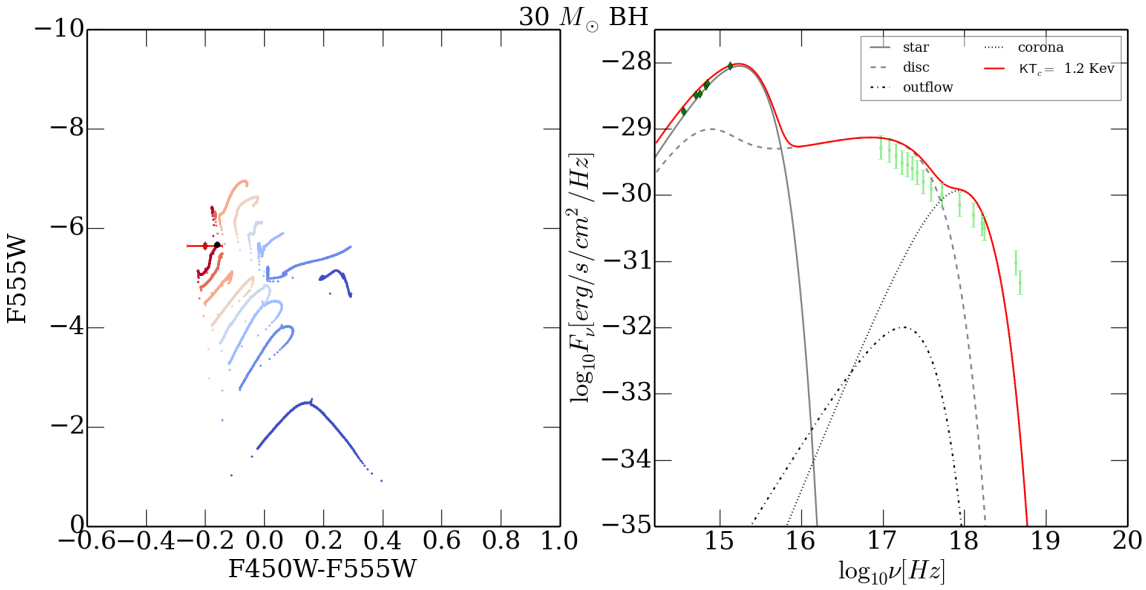

Figure 6.8: Intersection of the best-fit solution among the evolutionary tracks accreting onto a $30M_\odot$ BH with the optical counterpart of NGC 5204 X-1 (left),total Spectral Energy Distribution for the best fit solution together with those of the single components (right).

Running through all the SED selected according to photometry and age, with the three different electron temperatures of the corona, leads us to exclude the majority of the models. The system which better reproduces the optical and X-ray data is the one with initial donor and BH mass of 30 $M_\odot$, with actual donor mass of about 13 $M_\odot$ and present BH mass of about 40 $M_\odot$ in a marginally super-Eddington accretion phase during TAMS.
However, the fit is formally not statistically acceptable and the bolometric luminosity is not well reproduced. The reason for which the fit is not satisfactory is related to the fact that the last two points of the X-ray spectrum are not well reproduced. The source is harder than what predicted by our model and seems to require an additional tail to fit the highest X-ray data points, as noted by Mukherjee et al. (2015).

HolmbergII X1								
Best fit model for systems with $M_{d,i} = 20\ M_\odot$ and $M_{BH,i} = 50\ M_\odot$								
kT_e(keV)	t (Myr)	$M_d(t)$ $(M_\odot)$	$M_{BH}(t)$ $(M_\odot)$	$\dot{m}$	P (d)	$L_{tot}(erg/s)$	χ^2	d.o.f.
1.2	< 10	11.5	55	~ 10.5	5.56	$1.3 \cdot 10^{40}$	31.77	36

Table 6.4: Best fit models found minimizing the χ^2 method for HolmbergII X-1. Reported are the significant parameters of the best-fit intersections.

6.3.4 HolmbergII X-1

HolmbergII X-1 is located in the dwarf irregular galaxy, HolmbergII, which is in the M81 group of galaxies at a distance of 3.05 Mpc (see Tao et al. 2011, 2012 and references therein). Its luminosity reaches values $\sim 3 \cdot 10^{40} erg\ s^{-1}$ (Grisé et al., 2010) and is surrounded by a photoionized optical nebula (Kaaret et al., 2004) containing a point-like optical counterpart. A study recently published by Egorov et al. 2017 shows that X-1 is escaping from a very young cluster aged ~ 3.5--4.5 Myrs (Stewart et al., 2000), which we will be the reference age for our study. We take the photometry from Tao et al. (2012), that reported the average fluxes of non simultaneous observations in the F814W, F555W, F450E and F336W filers: $(2.71 \pm 0.54) \cdot 10^{-18}$, $(7.74 \pm 1.55) \cdot 10^{-18}$, $(1.34 \pm 0.27) \cdot 10^{-17}$ and $(2.70 \pm 0.54) \cdot 10^{-17}$ in units of $erg \cdot s^{-1} \cdot cm^{-2} \cdot \mathring{A}^{-1}$,respectively. We search for intersections with of the evolutionary tracks with data points on the CMD (calculated for different filters). Note that, because of the significant optical variability of the source, the error bar on the color is large. Fig. 6.9 shows the intersection of the evolutionary tracks of synthetic binaries in the F450W and F555W filters with the photometric measurements of HolmbergII X-1. This source cannot be reproduced by systems accreting onto a 10 $M_\odot$ BH, as shown in panel a). On the contrary, HolmbergII X1 can be reproduced with: a system accreting onto a BH with initial mass of 20 $M_\odot$ and donor with initial mass of 10, 12, 15 and 20 $M_\odot$ ascending along the Giant Branch panel b); system with a BH of initial mass of 30 and 50 $M_\odot$ accreting from donors whose initial mass spans a large range of values, from 10 and 30 $M_\odot$ in the H-shell burning phase (panels c and d); systems accreting onto more massive BHs of 70 and 100 $M_\odot$ from low massive donors, at TAMS, or from more massive donors of 25 and 30 $M_\odot$ in the middle of the Main Sequence. Considering the very young age inferred for this system by Stewart et al. (2000), the majority of the intersections are ruled out and we are left with the systems accreting onto massive BHs (50 and 70 $M_\odot$) from donors with initial mass from 15 to 25 $M_\odot$. We compared the SEDs obtained with our model with the observed optical through X-ray SED of HolmbergII X-1 to search for the best fit solution. The X-ray data are taken from Pintore et al. (2014). Given the very young age, the majority of the best fitting SED are systems in the sub-Eddington accretion phase, which can reproduce well the softer part of the X-ray spectrum but have a significantly different Spectral Energy Distribution at the higher frequencies. The intersection which best fits the data is a system with a MS donor younger than 10 Myrs with initial mass of 20 $M_\odot$ accreting onto a BH with initial mass of 50 $M_\odot$. The system is accreting marginally above Eddington. The actual mass of the donor is about 11 $M_\odot$ and that of the BH about 55 $M_\odot$. The orbital period is short, because during the long and stable RLOF phase which occurs during the MS, the mass ratio of the system does not change dramatically.

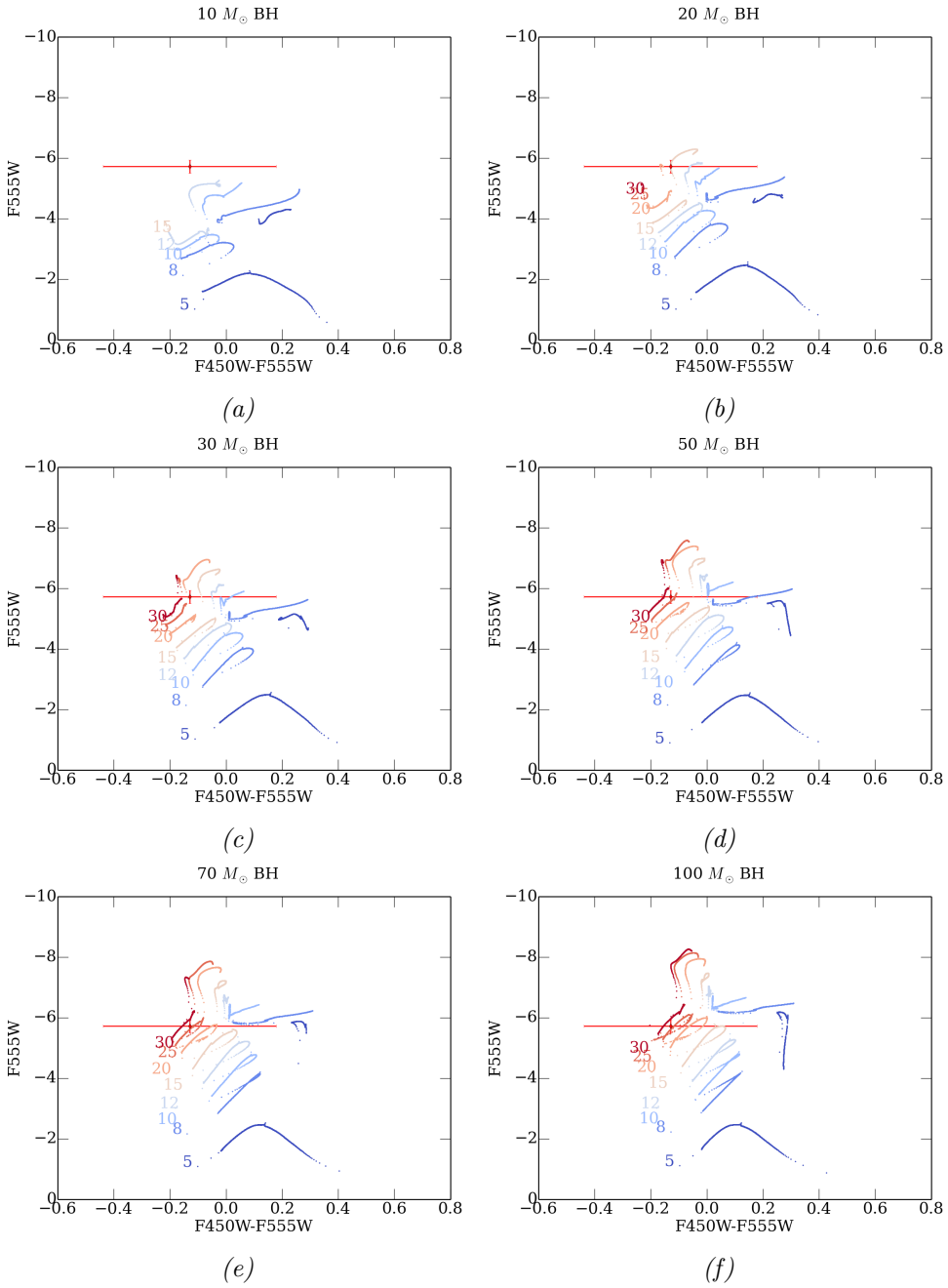

Figure 6.9: Comparison of the optical counterpart of HolmbergII X-1 with the evolutionary tracks that we evolved in this study in the CMD with magnitude F555W and color F450W-F555W. From panels a-f the BH mass increases from 10 to 100 $M_\odot$.

Fig. 6.10 shows that the SED that best fits the data, is produced by a cool corona with an electron temperature of 1.2 keV. Moreover, being the accretion rate marginally super-critical, the outflow is not very extended and does not contribute much to the X-ray emission. Looking at the optical emission, it is dominated by the donor star but also the standard disc contributes in a significant way.

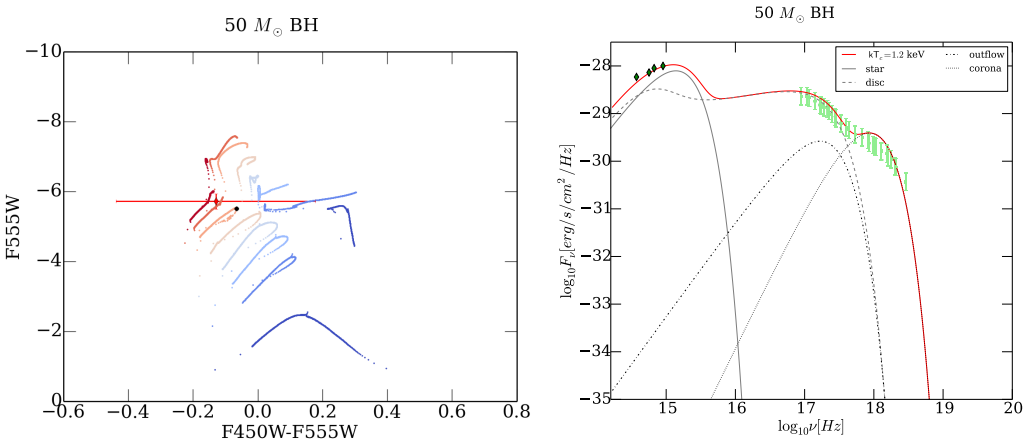

Figure 6.10: Intersection of the best-fit solution among the evolutionary tracks accreting onto a 50$M_\odot$ BH with the optical counterpart of HolmbergII X-1 (left),total Spectral Energy Distribution for the best fit solution together with those of the single components (right)

6.3.5 NGC 5907 ULX2

NGC5907 ULX2 is a recently discovered ULX (Pintore et al., 2018) at a distance of 17.1 Mpc and it reached a peak X-ray luminosity of $6.4 \cdot 10^{39} ergs^{-1}$. Being a recently discovered ULX, it is not well studied, and we do not have much information on its variability during the active phase. However, we know that the source is transient because in a previous observation taken in 2012, Chandra did not detect the source (with an upper limit of $1.5 \cdot 10^{38} ergs^{-1}$ on the X-ray luminosity). Although our model does not take into account the disc instabilities that may lead to a transient behaviour, we applied it to this source assuming that it can approximately describe its active phase We used the optical photometry and X-ray data presented in Pintore et al. (2018). Fig. 6.11 shows the intersection of the synthetic tracks with the photometric point of NGC 5907 ULX-2 on the CMD computed using the F450W magnitude and F450E and F814W filters. Panels a) and b) show that the source cannot be reproduced by systems accreting onto a 10 or 20 $M_\odot$ BH. Panel c) shows that the system can be reproduced by accretion from a donor which has an initial mass of 15 $M_\odot$ during its giant phase. On the basis of the photometry, panels d) e) and f) show that the system can be accreting onto more massive BHs of 50 $M_\odot$ from donor with initial mass of 15 $M_\odot$, 70 from donor with initial mass of 12 and 20 $M_\odot$ and 100 $M_\odot$ from donors with initial mass of 15 and 12 $M_\odot$. For this source we did not find information on the age of the host environment, therefore in the following we considered all the snapshots that intersect the photometric point of NGC 5907 ULX-2. Tab. 6.5 shows the result of the χ^2 statistic applied to the snapshots that we run for this source. The observed multiwavelength SED is better reproduced with a system composed of a donor star with mass of about 5.4 $M_\odot$ which is accreting at super-Eddington rates onto a BH of about 36 $M_\odot$. The system initially consisted of a 15 $M_\odot$ donor and a 30 $M_\odot$ BH. The accretion phase takes place while the donor is ascending along the Giant Branch. The binary has an orbital period of $\sim 24d$, therefore the disc is very extended. In Fig. 6.12 we show the different components which contribute to the overall emission spectrum: the optical band is dominated by the outer accretion disc, which is very bright being fuelled with a very high mass transfer rate.

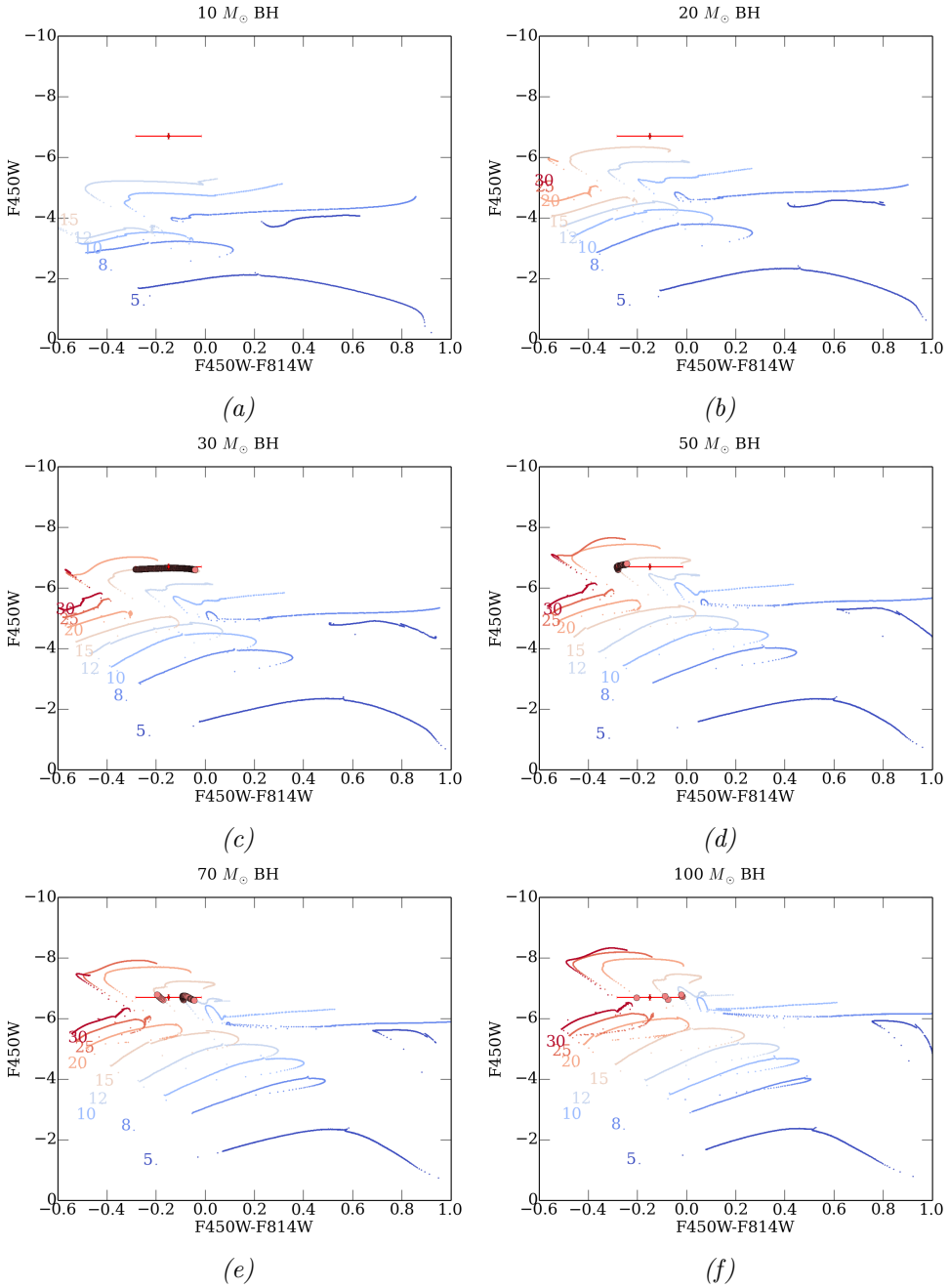

Figure 6.11: Comparison of the optical counterpart of NGC 5907 ULX2 with the evolutionary tracks that we evolved in this study in the CMD with magnitude F450W and color F450W-F814W. From panels a-f the BH mass increases from 10 to 100 $M_\odot$.

NGC 5907 ULX 2								
Best fit model for systems with $M_{d,i} = 15\ M_\odot$ and $M_{BH,i} = 30\ M_\odot$								
kT_e(keV)	t (Myr)	$M_d(t)$ $(M_\odot)$	$M_{BH}(t)$ $(M_\odot)$	$\dot{m}$	P (d)	$L_{tot}(erg/s)$	χ^2	d.o.f.
1.2	15.7	5.4	35.9	1890	~ 14	$2.1 \cdot 10^{40}$	8.390	10
1.5	15.7	5.4	35.9	1890	~ 14	$2.2 \cdot 10^{40}$	8.642	10
3.0	15.7	5.4	35.9	1890	~ 14	$2.9 \cdot 10^{40}$	9.008	10

Table 6.5: Best fit models found minimizing the χ^2 method for NGC 5907 ULX2. Reported are the significant parameters of the best-fit intersections.

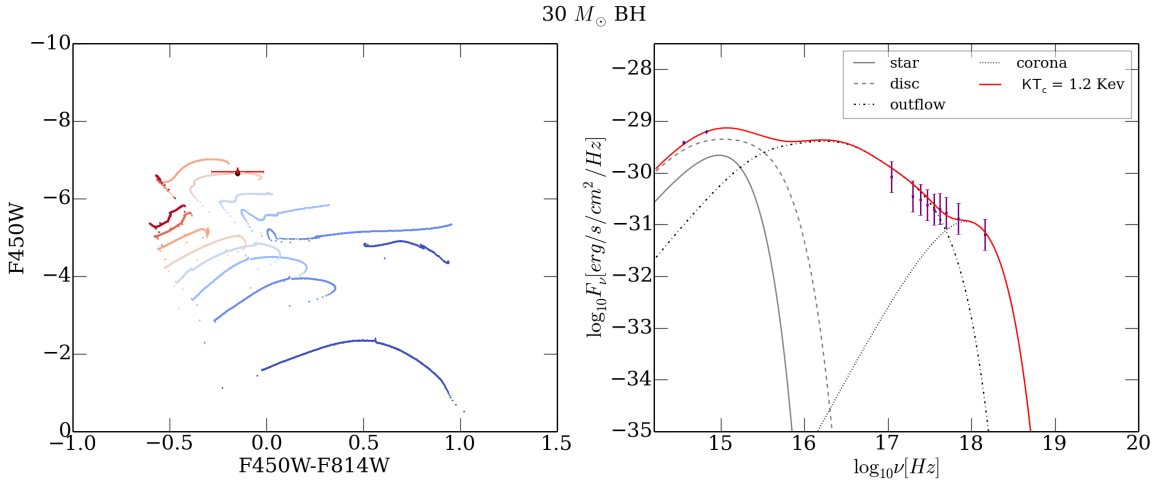

Figure 6.12: Intersection of the best-fit solution among the evolutionary tracks accreting onto a $30M_\odot$ BH with the optical counterpart of NGC 5907 ULX2 (left),total Spectral Energy Distribution for the best fit solution together with those of the single components (right).

Chapter 7

Summary, discussion and conclusions

The main goal of my PhD thesis was to investigate the nature of ULXs using their multiwavelength emission properties and to extend the treatment of the evolution of their binary systems including the effects of super-Eddington accretion. In this way we constrain the masses of the black holes and donor stars in these systems, and their accretion regime.
To this end, we developed a code that enables us to constrain the properties of ULXs binaries from their position on the Color-Magnitude Diagram, from their multiwavelength SED and from additional information available on the systems (such as the age of its parent stellar population). A novelty of this present treatment is the inclusion of super-Eddington accretion, with the possibility to produce the output in the HST photometric system; the extension of the parameter space for BH and donor masses with a proper computation of the orbital angular momentum loss during super-critical accretion; the possibility to model the Multiwavelength emission of ULXs considering the effects of a Comptonzing corona covering the innermost regions of the disc.

Method

The approach adopted in our investigation is described in detail in Chapters 4, 5, 6 and is shortly summarized here. We modelled the optical emission of ULXs accreting above the Eddington limit. At first we considered a bimodal accretion disc formed by an inner advection-dominated slim disc and an outer standard disc, adopting the parametrization of Watarai et al. (2000). Then, we included the effects of an outflow produced by radiation pressure, following the model by Poutanen et al. (2007). We studied the effects of the geometry of an advection-dominated disc without and with the outflow on the disc self-irradiation. We found that disc self-irradiation is significantly affected by the geometry of the disc and its implementation differs from that used for standard accretion. Therefore, in our model, the UV-X-ray irradiating luminosity is produced by the inner portions of the outer standard disc, if it is sufficiently hot. This is in contrast to sub-Eddington accretion, where the irradiating flux is produced by the entire inner region of the disc. We used the model of super-Eddington accretion disc plus outflow to compute the evolution of 12 binary systems, with BH mass of 20 and 100 $M_{\odot}$ and donor masses in the range $8 - 25\ M_{\odot}$.

In order to perform a direct comparison of the emission properties of ULX binary systems with the available HST photometric measurements, we used the code of Girardi et al. (2003) to calculate the donor magnitudes for a given luminosity, mass and metallicity. The Color-Magnitude-Diagrams produced with this model were compared to those obtained by PZ. With this method we analyzed the optical emission of two well studied ULXs: NGC 1313 X−2 and NGC 4559 X−7.
We applied our model to the new evolutionary tracks evolved with MESA and calculated the optical emission in the UBVRI Johnson and in the HST WFPC2, ACS and WFPC3 photometric systems. We then characterized the evolution of the new tracks on the CMD.
Finally, we introduced in the calculation of the SED of our systems an approximate treatment of Comptonization to better reproduce the hard X-ray emission of ULXs. We added to our model the contribution of a Comptonizing corona which covers the innermost regions of the disc. Following the observational evidence gathered from the X-ray spectral analysis (Pintore et al., 2014), we assumed that the Compton parameter of the corona is significantly larger than unity and that Comptonization is saturated. We considered four reference electron temperatures for the corona: 1.2, 1.5, 3 and 6 Kev, which adequately sample the range inferred from the fits of the observed ULXs spectra (Pintore et al., 2014).
Finally, we applied our calculation of the emission properties of evolved binary systems accreting above Eddington to a number of ULXs with well studied stellar optical counterparts: NGC 1313 X−2, NGC4559 X−7, NGC 5204 X−1, HolmbergII X−1 and NGC 5907 ULX−2.
Our approach followed these steps:

- search for the synthetic evolutionary tracks that intersect the observed photometric point of a ULX;
- among all the intersections,selection of those which have an age similar to that of the parent population of a given ULX;
- search for the best fitting of the multiwavelength SED among all remaining intersections.

Results

Here I briefly summarize the main results obtained in my Thesis using the model and method outlined above.
Effects of super-Eddington accretion on self-irradiation.
We found that, for super-Eddington accretion the disc self-irradiation is very different from that produced in the standard case. The innermost regions do not radiate the outer ones. Two competing effects affect self-irradiation. On one side, the irradiating flux grows with $\dot{m}$. On the other side, it decreases because the size of the irradiating region diminishes. Irradiation is considerably stronger than that produced by an Eddington-limited disc, but at very high $\dot{m}$ it is progressively less important than the intrinsic disc and donor emission.
Comparative analysis of the evolutionary tracks on the CMD.
We then compared the results obtained with our model with those of Patruno and Zampieri (2008). During MS, the evolutionary tracks on the CMD obtained with our model almost overlap with those of Patruno and Zampieri (2008). The residual difference depends on the

treatment of photometry and on the fact that the accretion rate can be mildly super-Eddington. On the other hand, the post MS evolution is markedly different and is characterized by two phases. Initially, when the accretion disc is not very extended, the luminosity increases with $\dot{m}$ and the system becomes bluer ($B - V = -0.3 - 0.1$). As the orbital separation increases, the accretion disc becomes bigger, the emission becomes progressively redder and the system moves to the right on the CMD. At super-Eddington rates, the disc flux typically overcomes that produced by the donor (apart from the case of small black holes and very massive donors) and the 'optical bump' that characterizes standard self-irradiated discs disappears.

Analysis of the optical counterparts of NGC 1313 X−2 and NGC 4559 X−7.

We found that the position of NGC 1313 X-2 on the CMD is in agreement with a $20M_{\odot}$ BH accreting above the Eddington limit from a post-MS donor with initial mass in the range $12 - 15M_{\odot}$. The orbital period of the system is ~ 5 days, in fair agreement with the observed one.

Considering NGC 4559 X-7, it is better reproduced with a 100 $M_{\odot}$ BH accreting above the Eddington limit from a ~ 15 $M_{\odot}$ donor. We did not consider donors more massive than $25M_{\odot}$ for a 20 $M_{\odot}$ BH because, after the MS, the outflow starts to engulf the binary and the model is no longer self-consistent. For less massive donors, no agreement is found because the optical emission is not sufficiently luminous. For a 100 $M_{\odot}$ BH, agreement is found for evolved donors of $15 - 25M_{\odot}$, smaller than in the Eddington-limited systems of PZ owing to the fact that super-Eddington accretion makes the tracks more luminous and bluer for a given donor mass.

Evolutionary tracks on the CMD.

We calculated a new grid of evolutionary tracks of ULX binary systems with the MESA code and found that they occupy two regions on the CMD, depending on the evolutionary stage of the donor.

When the donor is on the MS and accretion is sub-critical or marginally super-critical, the tracks are blue and their M_V magnitude is limited up to ~ -6. They occupy the bluer and comparatively fainter corner of the CMD. We notice that they are similar in shape for different BH masses, being the main difference the maximum value of M_V: more massive BHs generate more luminous tracks.

When the donor is ascending towards the Giant Branch, the properties of the evolutionary tracks are governed by the mass transfer rate, which is now super critical. Moreover, the binary separation increases rapidly producing a more extended accretion disc, which emits a huge of flux in the optical band, eventually enhanced by self-irradiation. This evolution drives the tracks towards higher V band luminosities. The colors are initially blue because the mass transfer rate at the beginning of the Giant phase is very high and the disc becomes hot. As the super-Eddington mass transfer continues, the systems widens and the accretion disc becomes more extended, driving the tracks towards redder colors. In addition, self-irradiation is essentially suppressed. However, after the peak, the mass transfer rate starts to decrease, irradiation starts to contribute again and the evolution towards the red slows down.

Modelling multiwavelength emission of ULXs. We applied our model to a number of ULXs with well studied stellar optical counterparts: NGC 1313 X−2, NGC 4559 X−7, NGC 5204 X−1, HolmbergII X−1 and NGC 5907 ULX−2.

- *NGC 1313 X-2:* We found that the best fit solution points to a system which is accreting

marginally super-Eddington from a donor of about 10 $M_{\odot}$ on to a BH of about 25 $M_{\odot}$. This system is aged $\sim$ 10 Myrs and descends from a system whose masses of the donor and the BH were original both 20 $M_{\odot}$. The orbital period of this system is $\sim$ 4 days, in reasonable agreement with the observed $\sim$ 6 d period.
The results obtained with the more extended grid of MESA models are in agreement with those obtained using the Eggleton code. A detailed discussion of previous estimates of the BH and donor masses for this source based on the analysis of the optical data is reported in Chapter 4. Here we add a few other estimates that are reported in the literature based on X-ray observations. Fitting the *XMM-Newton* data with a phenomenological model of a disc plus comptonizing corona, Pintore and Zampieri (2012) found that the source exhibits two different states. The first is characterized by low electron temperature of the corona ($kT_{cor} \sim 1.5$ keV) and high optical depth ($\tau \geq 10$), while the second shows smaller optical depths ($\tau \leq 8$), and a wider range of electron temperatures ($1.5 \lesssim kT_{cor} \lesssim 6$ keV). They suggest that, based on the X-ray properties, this source can be accreting slightly above the Eddington limit. Also Bachetti et al. (2013) analyzed in detail the X-ray spectral regimes of this source using also *NuSTAR* data, concluding that the spectra are consistent with an advection-dominated disc and a BH mass of about 25 $M_{\odot}$. Finally, Fiacconi et al. (2017) used the same outflow model by Poutanen et al. (2007) adopted in this work and, using the observed properties of the wind, found that the BH mass of this source is in the range 10-100 $M_{\odot}$.

- *NGC 4559 X-7:* The optical photometry of this source, together with the X-ray data, point to super-Eddington accretion onto massive BHs for this systems. We found that the observed properties are produced by a system accreting super-critical ($\dot{m}$: $900 - 1000$) onto a BH of $\sim$ 55 $M_{\odot}$ from a donor of $\sim$ 5.5 $M_{\odot}$ or with a more massive BH of $\sim$ 75 $M_{\odot}$ accreting from a $\sim$6 $M_{\odot}$ donor. The systems consists of a standard disc emitting most of the optical emission, and an optically thick an extended outflow which covers part of the standard disc and almost the entire inner advection dominated disc, and an optically thick cool corona, with electron temperature of $\sim 1.2keV$, which dominates the hard X-ray emission. The orbital period is fairly long, $\sim$ 18 d for a 55 $M_{\odot}$ BH and $\sim$ 12 d for a 70 $M_{\odot}$ BH. In fact, when accretion occurs at super-critical rates, the orbital separation increases rapidly. Both systems produce very high bolometric luminosity ($\sim 3 \cdot 10^{40} - 4 \cdot 10^{40} erg \cdot s^{-1}$), which are in agreement with the observed data. The results obtained with the MESA tracks are in agreement with those obtained with the Eggleton evolutionary tracks. This source was studied previously by other authors, and our results are in agreement with their findings. PZ found that the optical counterpart of X-7 is reproduced by a massive BH which accretes from a donor of 30-50 $M_{\odot}$ during the H-shell burning phase. Stobbart et al. (2006) analyzed some *XMM-Newton* observations of this source (which they refer to as NGC4559 X-1) finding that its spectral shape is consistent with super-Eddington accretion onto BHs with masses up to 80 $M_{\odot}$.

- *NGC 5204 X-1:* The result obtained from the χ^2 fit of the SED at the time of intersection on the CMD was not statistically acceptable but it suggests accretion at marginally super-critical rates from a donor with mass of $\sim$ 14 $M_{\odot}$ onto a BH with mass of $\sim$ 40 $M_{\odot}$.

The system is 6.8 Myrs old and accretion is taking place while the donor, whose initial mass was $\sim 30\ M_{\odot}$, is reaching the TAMS. However, the fit is not statistically acceptable and the bolometric luminosity is not well reproduced. The reason for which the fit is not satisfactory is related to the fact that the hard X-ray spectrum is not well reproduced. The source is harder than what predicted by our model and seems to require additional tail to fit the highest X-ray data points. The existence of such a tail was proposed by Mukherjee et al. (2015) on the basis of the spectral analysis of *NuSTAR* observations of NGC 5204 X-1.

- *HolmbergII X-1:* The modelling of this source shows that this system is accreting at marginally super-Eddington rates. The BH has a mass of about 55 $M_{\odot}$ while the donor star has $\sim 11\ M_{\odot}$. The best fit of the SED returns a corona temperature $\sim 1keV$. Kajava et al. (2012) studied the evolution of the spectral curvature of HolmbII finding that the *diskpbb*[1] model, with $p \approx 0.5$ fits the data better than the *diskbb*[2] model. Moreover, adding a Comptonizing component reproduces the spectrum well if a low electron temperature is considered ($kT_e \approx 1.2keV$). Their findings are in agreement with the results obtained with our model.

- *NGC5907 ULX-2 :* The observed multiwavelength SED is better reproduced with a system composed of a donor star with mass of about 4.5 $M_{\odot}$ which is accreting at super-Eddington rates onto a BH of about 36.5 $M_{\odot}$. The system initially consisted of a 15 $M_{\odot}$ donor and a 30 $M_{\odot}$ BH. The accretion phase takes place while the donor is ascending along the Giant Branch. The binary has an orbital period of $\sim 24d$, therefore the disc is very extended. As reported by Pintore et al. (2018) the color and luminosity of the optical counterpart are consistent with those of an O-B type star. From our modelling, it is clear that the contribution of the accretion disc to the optical emission is dominant. Therefore the overall scenario can be misinterpreted if optical emission is ascribed only to the donor star. The outer standard disc contribute enormously to the optical flux miming the emission of that of a massive donor.

Three out of five ULXs are well represented by systems with BH mass in the range between 25-30 $M_{\odot}$, while for two of them the best-fit solution points to more massive Black Holes, in the range 40-55 $M_{\odot}$. Therefore, although the present sample of ULXs is very small and not representative of the whole population, the observational properties, together with the age estimate, seem to favour the existence of massive BHs in these sources.

Future perspectives

The model presented in this work, can be applied to all the ULXs for which an unique optical counterpart has been identified. We are working at analysing the properties of other ULXs

[1] In the X-ray spectral fitting package XSPEC the *diskpbb* model is a multi-temperature blackbody disc model, where the local disc temperature T(r) is proportional to r^{-p}, where p is a free parameter (see Mineshige et al. 1994).

[2] In the X-ray spectral fitting package XSPEC the *diskbb* model refers to a multi-temperature blackbody disc model, where the the local disc temperature T(r) is proportional to $r^{-3/4}$ (see Mitsuda et al. 1984).

for which optical data of the counterparts and the environment are available, although not as accurate as the one available for the sources presented here.
The investigation presented in this Thesis can be extended in different directions. One possibility is improving the modelling of the X-ray emission of the disc, considering various electron temperatures for the Comptonizing corona. Moreover, adding the size of the corona as a free parameter, would improve the quality of the fit.
Another important area of future investigation is certainly the treatment of the outflow and its efficiency in removing accretion energy. We run our models fixing the fraction of radiative luminosity which accelerates the outflow, following (Poutanen et al., 2007). We analysed the effects of variations of this parameter on the optical emission, finding that there they are not very important. However, the effects on the X-ray emission need to be properly addressed in the future.
Most importantly, the results presented in this Thesis refer entirely to the optical emission of ULXs powered by accretion onto Black Holes. The next step, already partly implemented, is to consider ULXs with Neutron Stars (NSs) and include the effects of the magnetic field geometry in the multi-wavelength emission model. The ultimate goal will be to compare the emission properties of stellar-mass/massive BHs to those of NSs systems, and confront the model predictions with the available observations of Pulsars ULXs. As detecting pulsations has proven to be difficult, this activity is of high importance because it may provide an independent tool to distinguish NS from BH ULXs.
The problem here is that mass transfer from a massive star onto a Neutron Star can be very unstable and the evolution of these system is complex to reproduce. Although not sufficiently developed to be included in this Thesis, we note that a few preliminary results of this work were already obtained and presented at the "Ultra-luminous X-ray Pulsars Workshop", held in Madrid last June.

Appendices

Appendix A

Unveiling ULX Pulsars from Optical Data: an Exploratory Study

A.1 Introduction

This appendix is dedicated to the ULX pulsars. Since the discovery of the first pulsating ULX in 2014 (Bachetti et al., 2014) three other sources have been found to be accreting pulsars (Israel et al., 2017a,b; Carpano et al., 2018). Detecting the pulsation is far from being simple: it can be feasible if the pulse axis is aligned to the observer. Given the low probability that the entire sample of ULX pulsars is in a such favourable condition, it is of fundamental importance to find alternative methods to distinguish between ULXs accreting onto a BH or a NS.
In Pintore et al. (2017) a large sample of bright ULXs have been studied with the aim to search for a specific signature in the spectra through which infer the nature of the compact object. They found that at temperature above 2 keV, the spectra of the known ULX pulsars are harder respect to the other ULXs analyzed in their study. Despite the effort of searching distinguishing spectral clues, a clear spectral signature has not been found so far.
With this in mind, we ask whether it is possible to apply the method presented in this thesis also to ULX pulsars. In this appendix we are going to present the results of the preliminary study applied to the optical emission alone.

A.2 Optical Emission of Pulsar ULXs

As we did for the case with accretion onto BHs, we want to assess if it is possible to constrain the mass of the donor and the evolutionary stage of ULXs pulsar from their optical emission. We used the evolutionary code MESA (Paxton et al., 2011, 2015) to evolve binaries with different masses accreting onto a neutron star. In these first exploratory study we did not consider the magnetic field of the neutron star, because we are only interested on the optical emission.
The first steps aim at investigating the possibility to perform this kind of study. We therefore assume:

- non-magnetized NS of 1.4 $M_{\odot}$;

- conservative mass transfer;
- case A mass transfer until the NS becomes very massive (we choose an upper limit of 2.5 $M_\odot$) or mass transfer becomes unstable;
- donor stars with masses in the range 2-4 $M_\odot$. This range of mass is broadly consistent with the estimate of M82 X−2 (Bachetti et al., 2014) and NGC5907 ULX−1 (Israel et al. 2017a, see also Tauris et al. 2000). More massive donors cannot steadily evolve with this model. [1]

A.2.1 Evolution during the accretion phase of a NS ULX binary with donors of 2.5 and 4 $M_\odot$

Systems with donor of 2.5 $M_\odot$

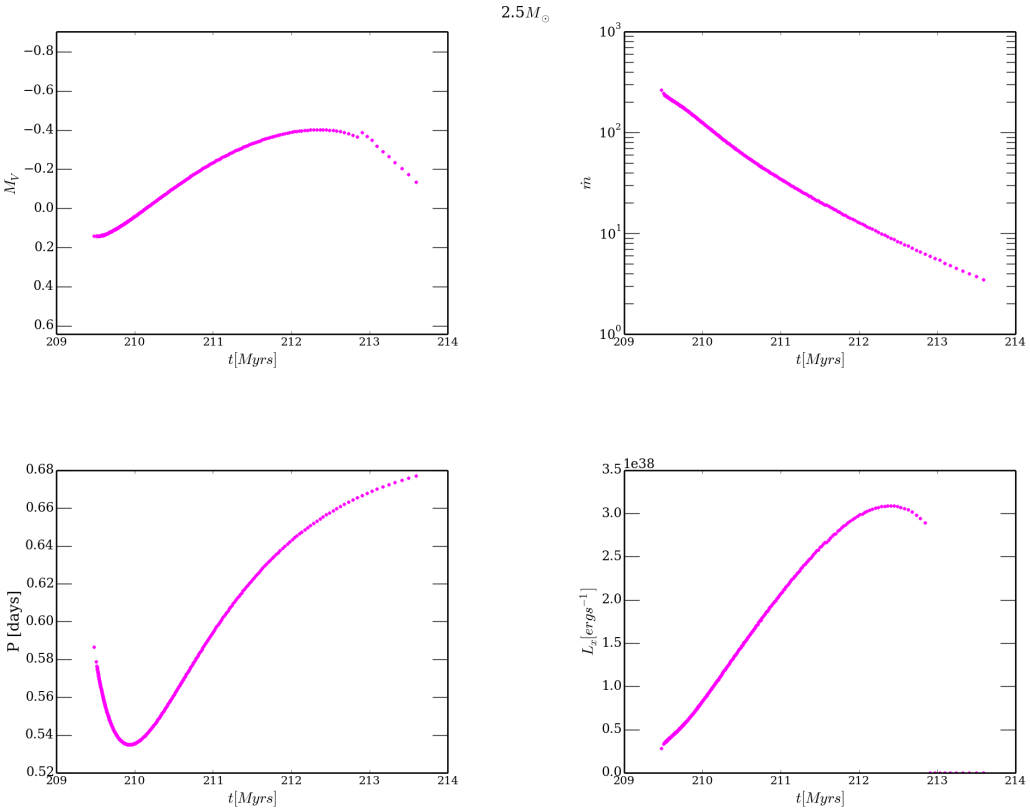

Figure A.1: Evolution during the accretion phase of a NS ULX binary with donor of 4 $M_\odot$. Evolution of the V band magnitude (upper left panel), evolution of $\dot{m}$ (upper right panel), evolution of the orbital period (lower left) and of the X-ray irradiating luminosity (lower right)

The RLOF phase of this system starts with super-Eddington accretion: as can be seen from

[1] Given the low mass of the neutron star, we found that systems with donors more massive than 4 $M_\odot$ went abruptly to dynamic unstable mass transfer.

the upper right panel of Fig. A.1, $\dot{m} \sim 10^2$ at the beginning of the RLOF and decreases during the evolution. The X-ray irradiation luminosity is important for this value of mass transfer (see lower right panel of Fig. A.1) and drives the evolution of the V band magnitude (upper left panel of Fig. A.1): the intrinsic emission of the irradiated outer accretion disc, which extends as the evolution proceeds (lower right panel of Fig. A.1), dominates the optical flux.

Systems with donors of 4 $M_\odot$

The system with donor of 4 $M_\odot$ starts the accretion phase with a higher mass transfer rate than the system with 2.5 $M_\odot$ donor, as can be seen from the upper right panel of Fig. A.2:

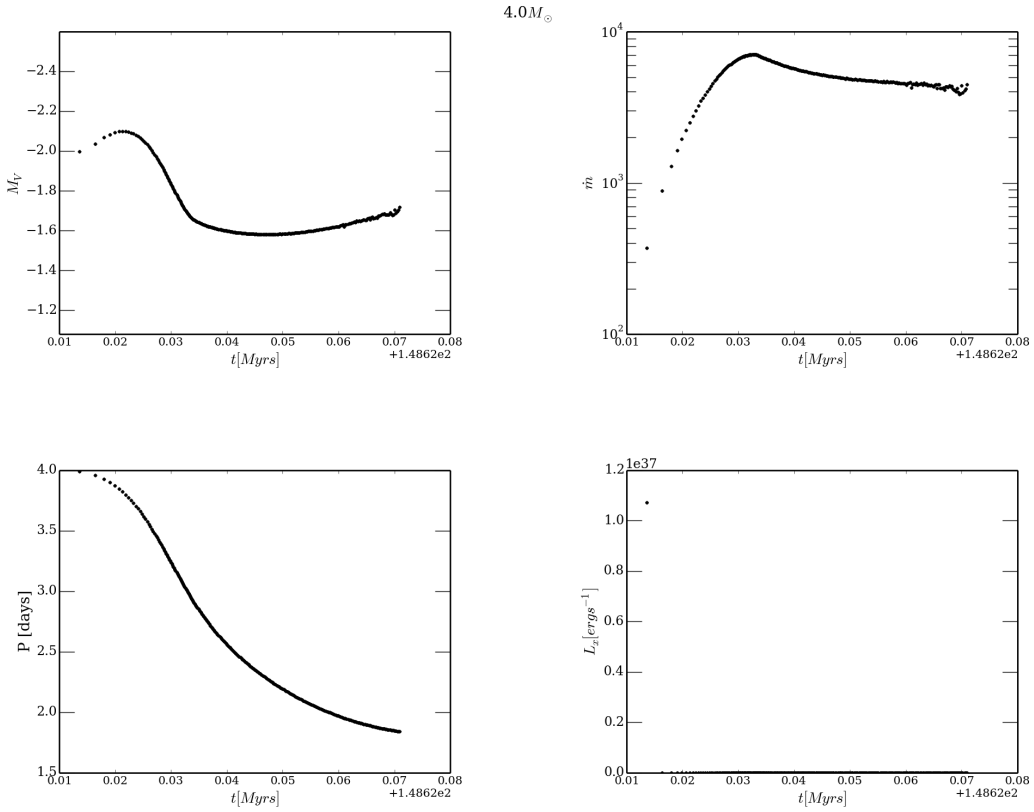

Figure A.2: Evolution during the accretion phase of a NS ULX binary with donor of 2.5 $M_\odot$. Evolution of the V band magnitude (upper left panel), evolution of $\dot{m}$ (upper right panel), evolution of the orbital period (lower left) and of the X-ray irradiating luminosity (lower right)

it reaches values up to $\approx 10^4 \dot{M}_{Edd}$. Self-irradiation is suppressed when $\dot{m}$ is extremely super-Eddington (lower-right panel of Fig. A.2) because the outflow is so extended to emit the bulk of its radiation in the optical band of the spectrum, as we shown in chapter 4. Also in this case, the emission in the V band is dominated by the accretion disc. Conversely to the previous case, V band magnitude diminishes on the evolutionary path because the system shrinks, (the lower left panel of Fig. A.2 shows a decreasing period with time) and the disc becomes less extended and cooler, also because the mass transfer rate diminishes (upper right panel of Fig. A.2.)

A.2.2 Evolutionary tracks on the B-V color and V magnitude CMD

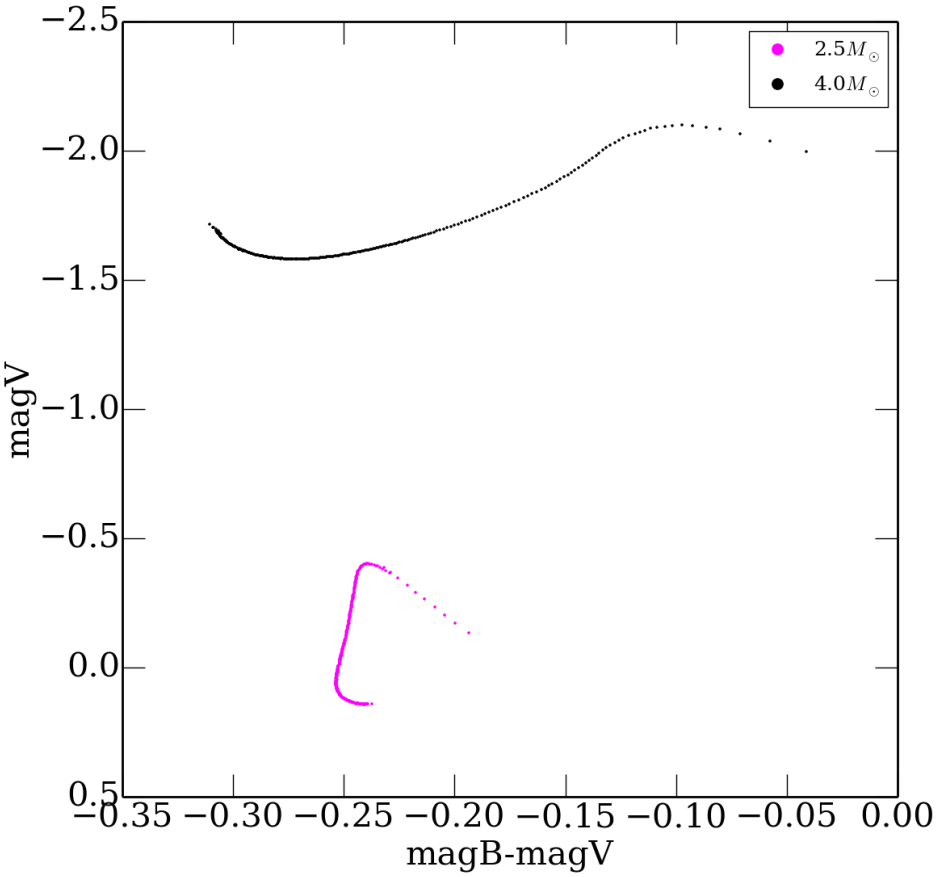

Figure A.3: Colour-magnitude diagram in the $B-V$ colour and M_V magnitude for systems with donors of 2.5 (purple lower line) and 4 (black upper line) $M_\odot$ accreting onto a NS with initial mass of 1.4 $M_\odot$.

The evolutionary tracks on the CMD of the two representative ULX pulsars described above are shown in Fig. A.3. The upper black line represents the system with a 4 $M_\odot$ donor, while the lower pink line refers to the system with 2.5 $M_\odot$ donor.
Both the tracks have blue colors but the V band magnitude is very faint and considerably weaker than those obtained for the evolutionary tracks of BH ULXs. We conclude that, for distances such that those of the observed ULXs, the optical counterparts of ULX pulsars are essentially undetectable with HST if the masses of the donor stars are in the range 2.5-4 $M_\odot$. This result is consistent with the non-detection of the counterpart of NGC 5907 ULX-1 (Sutton et al., 2013a). We underline that the ULX pulsar with a detected optical counterpart is the system NGC 7793 P13, which is accreting from a massive donor (18-23 $M_\odot$ Israel et al. 2017b) and has been proved to be an eccentric binary system (Israel et al., 2017b; Hu et al., 2017), therefore the accretion from a massive donor onto a neutron star is feasible. We propose to study in the future this kind of systems, considering the evolution of binaries in case of non-zero eccentricity.

Appendix B

Bimodal disc structure without outflow

In this section we report for comparison the results obtained for a disc with a bimodal structure without outflow (Sec. 4.3.1). Fig. B.1 shows the evolutionary tracks for systems with donors of 10 and 25 $M_{\odot}$ and BHs of 20 and 100 $M_{\odot}$, compared to the model of PZ.

The synthetic spectra are computed for the same evolutionary phases considered before for the case with outflow (a, b and c) and are shown in Figs. B.2- B.5. When $\dot{m}$ is highly super-Eddington, the systems are more luminous than those of PZ. At the beginning of the Giant phase they are bluer while, at the final stages of their evolution (when the accretion disc is very extended), they become redder.

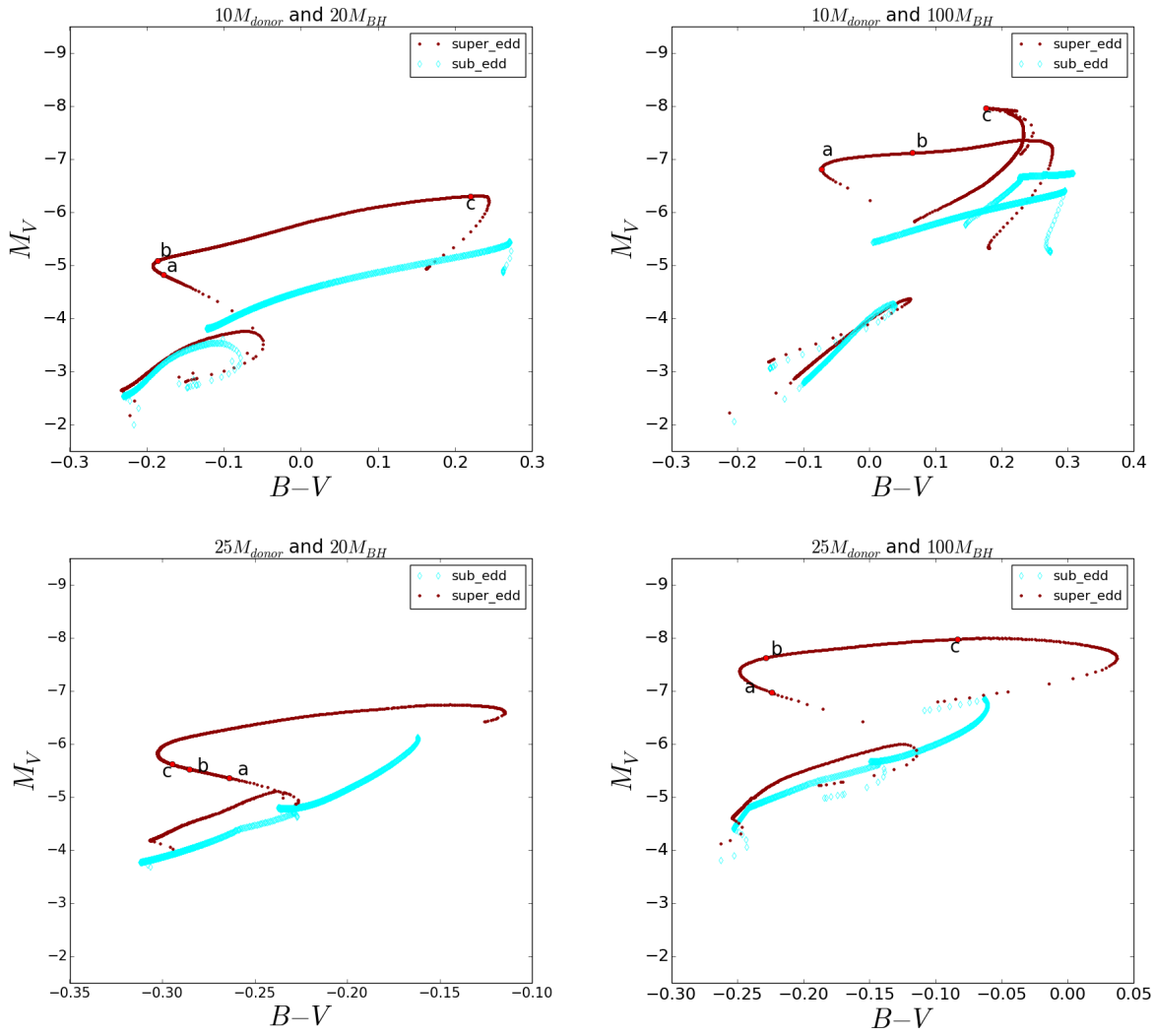

Figure B.1: Evolution on the colour-magnitude diagram of a ULX binary system with a donor mass of $10M_{\odot}$ (upper panels) or $25M_{\odot}$ (lower panels) at zero age main sequence and a BH mass of $20M_{\odot}$ (left panels) or $100M_{\odot}$ (right panels). The thick (light grey, cyan in the on-line version) line represents the evolution calculated assuming standard sub-Eddington accretion (PZ). The thin (dark gray, red in the on-line version) line represents the new evolution computed for super-Eddington accretion without an outflow. Points a, b and c mark the evolutionary phases at which the spectral energy distribution is computed.

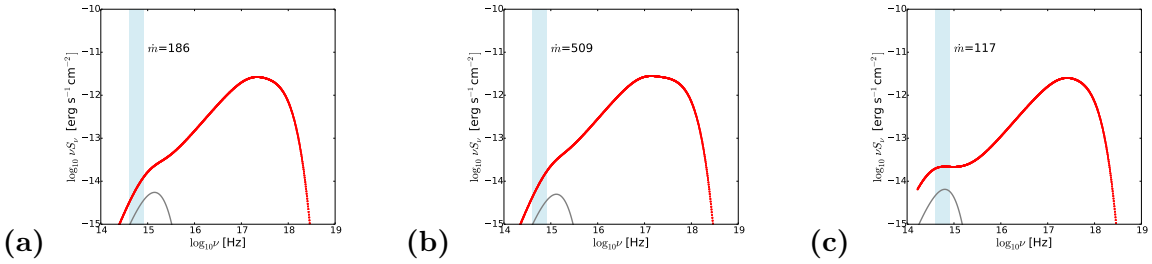

Figure B.2: Optical-through-X-ray spectrum of the system with a $10M_\odot$ donor and a $20M_\odot$ BH at the phases marked with a, b and c on the evolutionary tracks for super-Eddington accretion without an outflow. The thick (red) line represents the spectrum of the self-irradiated outer disc plus the outflow and the innermost slim disc, while the thin (gray) line is the spectrum of the X-ray heated donor. The gray (light blue) strip marks the optical band. Irradiation is significant at all phases and causes the observed increase of the optical flux.

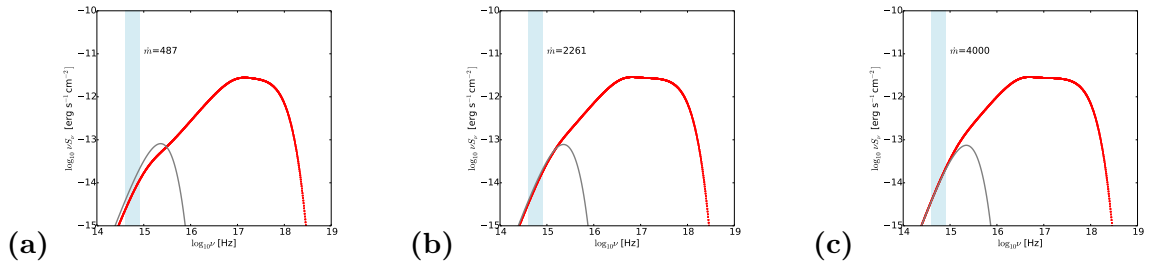

Figure B.3: Same as Figure B.2 for a $25M_\odot$ donor and a $20M_\odot$ BH. The accretion rate is so high that the optical flux emitted from the disc dominates over that from irradiation.

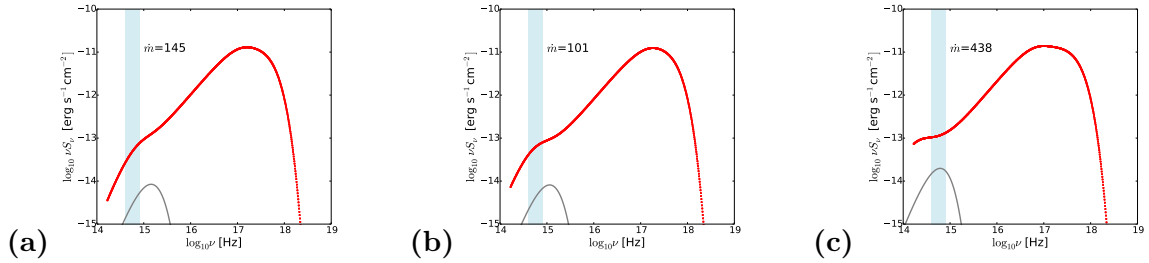

Figure B.4: Same as Figure B.2 for a $10M_\odot$ donor and a $100M_\odot$ BH. Irradiation is significant at all phases and causes the observed increase of the optical flux.

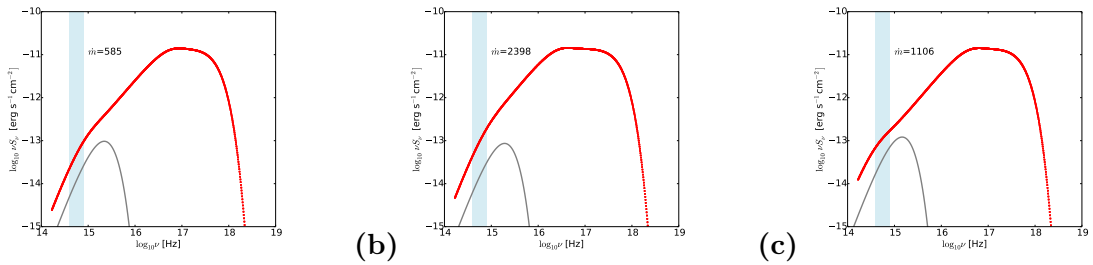

Figure B.5: Same as Figure B.2 for a $25M_\odot$ donor and a $100M_\odot$ BH. The accretion rate is so high that the optical flux emitted from the disc dominates over that from irradiation.

Appendix C

Comparison between two stellar and binary evolution codes: MESA and Eggleton codes

The work of this thesis is based on the synthetic binary evolutionary tracks that we obtained using two different environments: the first is the Eggleton code (STARS, Eggleton 1971; Pols et al. 1995) and the second is the Modules for Experiments in Stellar Astrophysics (MESA, Paxton et al. 2011, 2013, 2015).
The work described in chapter 4 makes use of the evolutionary tracks produced with the Eggleton code, which were used also by PZ and PZ2. We adopted the same evolutionary tracks in order to compare the differences on the optical emission induced by a diverse accretion physics itself. We successively produced a new grid of evolutionary tracks adopting another stellar evolution environment: MESA. In the following we are going to briefly discuss the convenience of this choice.
As reported by Paxton et al. (2015) in the presentation paper of the MESAbinary environment, the innovation of this module, respect to the STAR code for binary evolution, resides on the way in which the evolution of the binary is performed. While STARS solves simultaneously the two stars and the orbit of the binary in a single Newton-Raphson solver, MESA uses the same timestep to evolve independently the structure of each star and the orbital parameters. Moreover, the choice of the timestep is different between the two codes: in STARS the user must define it as an initial input parameter given in years. A different approach is defined in MESA, which calculates the time step depending on the relative variation of some binary parameters: the Roche lobe radius, the total orbital angular momentum, the orbital separation and the envelope mass of the donor. The user has the possibility to choose which and how many parameters invoke in the determination of the timestep. Moreover, she/he can also determine the relative variation of the donor structure in different cases of mass transfer (A, B or C described in chapter 3). This last choice permits to integrate the evolution of the more stable mass transfer episodes, such those occurring when the donor is on the MS, with the advantage of save computational time.
Moreover, MESA is notoriously more user-friendly than STARS and, via its useful tool *pgstar*, one can visualize on-screen the run progresses.

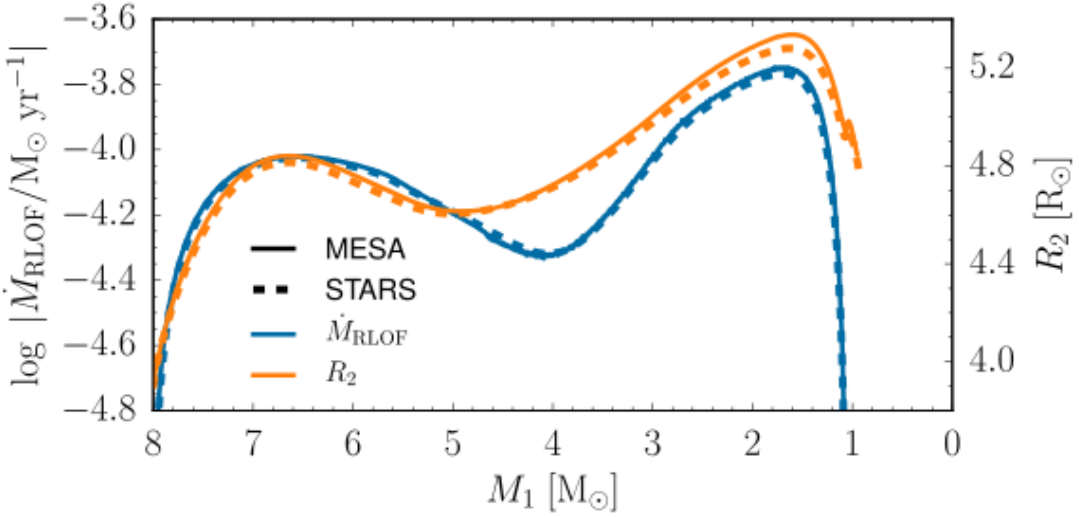

Figure C.1: Mass transfer rate and accretor radius as computed by MESA (solid lines) and STARS (dashed lines) for a binary of $8M_\odot$ + 6.5 $M_\odot$ with initial orbital period P = 3 d. Taken from Paxton et al. (2015)

Despite these differences, the physics of both MESA and STARS are up to date, and the two codes produce analogous results. Fig. C.1, taken from the MESAbinary paper (Paxton et al., 2015) shows the evolution of a binary with donor of $8M_\odot$ accreting onto a $6.5M_\odot$, calculated with MESA (solid lines) and STARS (dashed lines). The evolution of the binary is similar, with a slightly higher value of the mass transfer rate (blue lines) obtained by MESA respect to that obtained by STARS, to which it is associated a higher donor radius (orange lines) given by MESA than that given by STARS.

Last, MESA gives the possibility to easily adapt non-Eddington-limited accretion to our model of disc plus outflow described in this thesis.

Appendix D

Inlists for the MESA evolutionary tracks

Inlist Project

&*binary_job inlist_names*(1) =′ *inlist*1′
inlist_names(2) =′ *inlist*2′
evolve_both_stars = .*false*.
!*endofbinary_jobnamelist* &*binary_controls*
*read_extra_binary_controls_inlist*1 = .*true*.
*extra_binary_controls_inlist*1_*name* = "*inlist_timestep*1"
! Mass transfer rates are computed following Ritter scheme
mdot_scheme = "*roche_lobe*"
*m*1 = ! donor mass in Msun
*m*2 = ! companion mass in Msun
initial_period_in_days =
!*initial_separation_in_Rsuns* = 10! only used when *initial_period_in_days* < 0
mass_transfer_beta = 0.3525
!Mass accretion to the black hole is limited to the point where it reaches its
!Eddingtion luminosity
limit_retention_by_mdot_edd = .*false*.
initial_BH_spin = 0

!orbital J controls
do_jdot_mb = .*false*.
max_tries_to_achieve = 150
implicit_scheme_tolerance = 1*d* − 5
min_change_factor = 1.01*d*0
max_change_factor = 1.25*d*0
initial_change_factor = 1.25*d*0
change_factor_fraction = 0.8*d*0
implicit_lambda = 0.4*d*0
min_mdot_for_implicit = 1*d* − 16

$starting\_mdot = 1d - 12$
$terminal\_interval = 1$
!!set this to true to get more information on the mass transfer solver
!$report\_rlo\_solver\_progress = .true.$
!$endofbinary\_controls\_namelist$

Timestep controls

! timestep controls
fr = 0.005
$fr\_limit = 1\mathsf{d} - 3$
$fr\_dt\_limit = 1d2$
fj = 0.001
$varcontrol\_ms = 1d - 4$
$varcontrol\_post\_ms = 1d - 5$
$varcontrol\_case\_b = 1d - 5$
$varcontrol\_case\_a = 1d - 5$

Appendix E

Additional Figures

Here we report the evolutionary tracks in the CMD in the B-V color and M_V magnitude for the MESA evolutionary tracks grouped with systems with fixed donor mass.

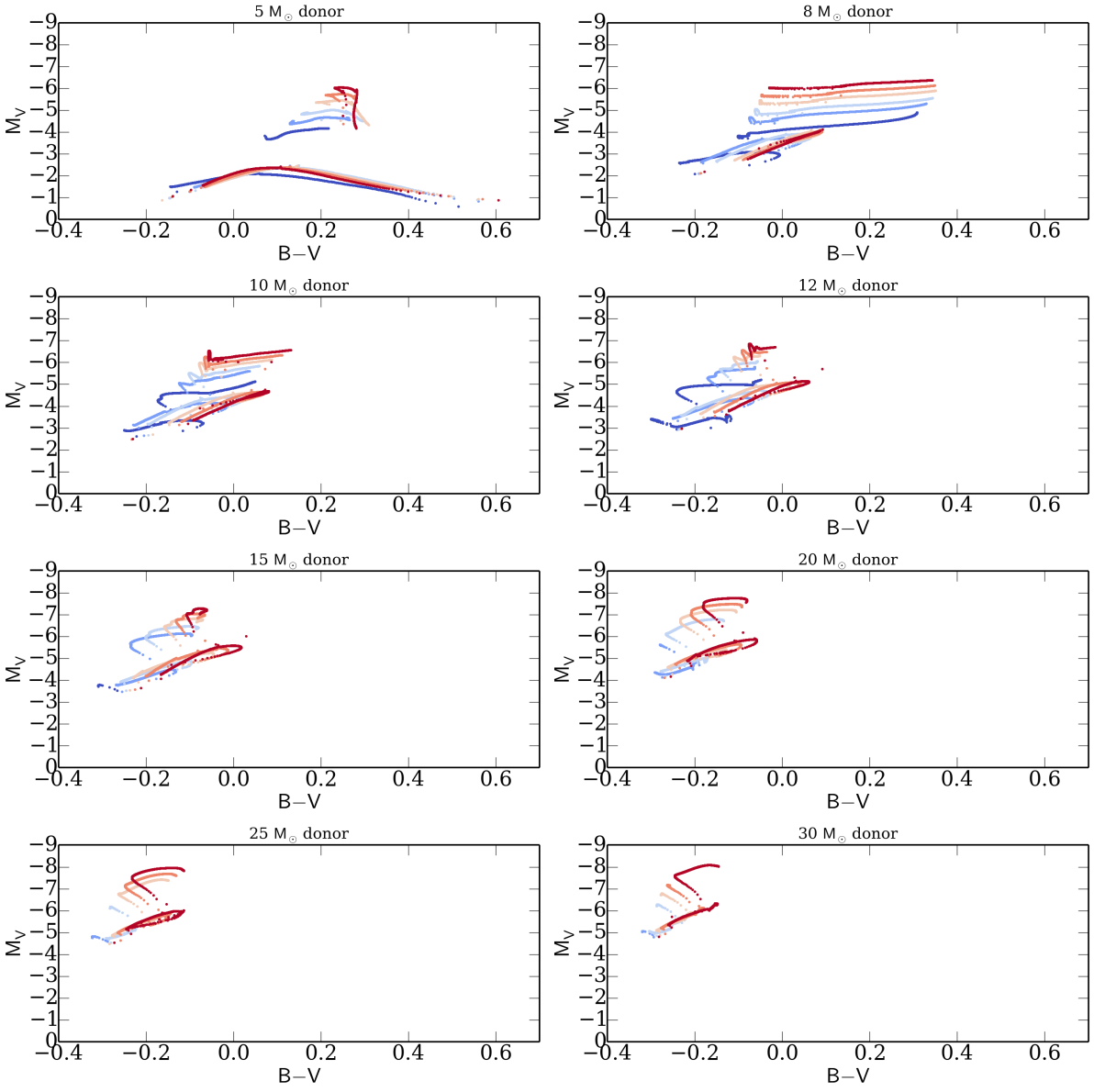

Figure E.1: CMD in the M_V magnitude and $B-V$ color for MESA binary systems with donor mass fixed.

Bibliography

Abbott, B. P., Abbott, R., Abbott, T. D., Abernathy, M. R., Acernese, F., Ackley, K., Adams, C., Adams, T., Addesso, P., Adhikari, R. X., Adya, V. B., Affeldt, C., Agathos, M., Agatsuma, and other authors (2016). Observation of gravitational waves from a binary black hole merger. *Phys. Rev. Lett.*, 116:061102.

Abramowicz, M. A., Czerny, B., Lasota, J. P., and Szuszkiewicz, E. (1988). Slim accretion disks. *The Astrophysical Journal*, 332:646–658.

Ambrosi, E. and Zampieri, L. (2018). Modelling optical emission of ultraluminous X-ray sources accreting above the Eddington limit. *Monthly Notices of the Royal Astronomical Society*, 480:4918–4930.

Bachetti, M., Harrison, F. A., Walton, D. J., Grefenstette, B. W., Chakrabarty, D., Fürst, F., Barret, D., Beloborodov, A., Boggs, S. E., Christensen, F. E., Craig, W. W., Fabian, A. C., Hailey, C. J., Hornschemeier, A., Kaspi, V., Kulkarni, S. R., Maccarone, T., Miller, J. M., Rana, V., Stern, D., Tendulkar, S. P., Tomsick, J., Webb, N. A., and Zhang, W. W. (2014). An ultraluminous X-ray source powered by an accreting neutron star. *Nature*, 514:202–204.

Bachetti, M., Rana, V., Walton, D. J., Barret, D., Harrison, F. A., Boggs, S. E., Christensen, F. E., Craig, W. W., Fabian, A. C., Fürst, F., Grefenstette, B. W., Hailey, C. J., Hornschemeier, A., Madsen, K. K., Miller, J. M., Ptak, A. F., Stern, D., Webb, N. A., and Zhang, W. W. (2013). The Ultraluminous X-Ray Sources NGC 1313 X-1 and X-2: A Broadband Study with NuSTAR and XMM-Newton. *The Astrophysical Journal*, 778:163.

Balbus, S. A. and Hawley, J. F. (1991). A powerful local shear instability in weakly magnetized disks. I - Linear analysis. II - Nonlinear evolution. *The Astrophysical Journal*, 376:214–233.

Belczynski, K., Bulik, T., Fryer, C. L., Ruiter, A., Valsecchi, F., Vink, J. S., and Hurley, J. R. (2010). On the Maximum Mass of Stellar Black Holes. *The Astrophysical Journal*, 714:1217–1226.

Carpano, S., Haberl, F., Maitra, C., and Vasilopoulos, G. (2018). Discovery of pulsations from NGC 300 ULX1 and its fast period evolution. *Monthly Notices of the Royal Astronomical Society*, 476:L45–L49.

Colbert, E. J. M. and Mushotzky, R. F. (1999). The Nature of Accreting Black Holes in Nearby Galaxy Nuclei. *The Astrophysical Journal*, 519:89–107.

Copperwheat, C., Cropper, M., Soria, R., and Wu, K. (2005). Optical and infrared signatures of ultra-luminous X-ray sources. *Monthly Notices of the Royal Astronomical Society*, 362:79–88.

Copperwheat, C., Cropper, M., Soria, R., and Wu, K. (2007). Irradiation models for ULXs and fits to optical data. *Monthly Notices of the Royal Astronomical Society*, 376:1407–1423.

Cox, A. (1999). editor, Allen's Astrophysical Quantities.

Cropper, M., Soria, R., Mushotzky, R. F., Wu, K., Markwardt, C. B., and Pakull, M. (2004). Probable intermediate-mass black holes in NGC 4559: XMM-Newton spectral and timing constraints. *Monthly Notices of the Royal Astronomical Society*, 349:39–51.

de Jager, C., Nieuwenhuijzen, H., and van der Hucht, K. A. (1988). Mass loss rates in the Hertzsprung-Russell diagram. *Astronomy and Astrophysics Supplement Series*, 72:259–289.

Ebisawa, K., Życki, P., Kubota, A., Mizuno, T., and Watarai, K.-y. (2003). Accretion Disk Spectra of Ultraluminous X-Ray Sources in Nearby Spiral Galaxies and Galactic Superluminal Jet Sources. *The Astrophysical Journal*, 597:780–797.

Eggleton, P. P. (1971). The evolution of low mass stars. *Monthly Notices of the Royal Astronomical Society*, 151:351.

Eggleton, P. P. (1983). Approximations to the radii of Roche lobes. *The Astrophysical Journal*, 268:368.

Egorov, O. V., Lozinskaya, T. A., and Moiseev, A. V. (2017). The ultraluminous X-ray source HoII X-1: kinematic evidence of its escape from a cluster. *Monthly Notices of the Royal Astronomical Society*, 467:L1–L5.

Fabbiano, G. (1989). X rays from normal galaxies. *Annual Review of Astronomy and Astrophysics*, 27:87–138.

Fabbiano, G., Kim, D. W., Fragos, T., Kalogera, V., King, A. R., Angelini, L., Davies, R. L., Gallagher, J. S., Pellegrini, S., Trinchieri, G., Zepf, S. E., and Zezas, A. (2006). The Modulated Emission of the Ultraluminous X-Ray Source in NGC 3379. *The Astrophysical Journal*, 650:879–884.

Fabrika, S., Ueda, Y., Vinokurov, A., Sholukhova, O., and Shidatsu, M. (2015). Supercritical accretion disks in ultraluminous X-ray sources and SS 433. *Nature Physics*, 11:551–553.

Feng, H. and Kaaret, P. (2005). XMM-Newton Observations of Ultraluminous X-Ray Sources in Nearby Galaxies. *The Astrophysical Journal*, 633:1052–1063.

Feng, H. and Kaaret, P. (2008). Optical Counterpart of the Ultraluminous X-Ray Source IC 342 X-1. *The Astrophysical Journal*, 675:1067–1075.

Feng, H. and Soria, R. (2011). Ultraluminous X-ray sources in the Chandra and XMM-Newton era. *New Astronomical Review*, 55:166–183.

Fiacconi, D., Pinto, C., Walton, D. J., and Fabian, A. C. (2017). Constraining the mass of accreting black holes in ultraluminous X-ray sources with ultrafast outflows. *Monthly Notices of the Royal Astronomical Society*, 469:L99–L103.

Frank, J., King, A., and Raine, D. (2002). *Accretion power in astrophysics*. Cambridge University Press.

Frank, J., King, A., and Raine, D. J. (2002). *Accretion Power in Astrophysics: Third Edition*.

Fürst, F., Walton, D. J., Harrison, F. A., Stern, D., Barret, D., Brightman, M., Fabian, A. C., Grefenstette, B., Madsen, K. K., Middleton, M. J., Miller, J. M., Pottschmidt, K., Ptak, A., Rana, V., and Webb, N. (2016). Discovery of Coherent Pulsations from the Ultraluminous X-Ray Source NGC 7793 P13. *The Astrophysical Journal Letters*, 831:L14.

Girardi, L., Bertelli, G., Bressan, A., Chiosi, C., Groenewegen, M. A. T., Marigo, P., Salasnich, B., and Weiss, A. (2003). Theoretical isochrones in several photometric systems. *Mem. Soc. Astronom. Italiana*, 74:474.

Gladstone, J. C., Copperwheat, C., Heinke, C. O., Roberts, T. P., Cartwright, T. F., Levan, A. J., and Goad, M. R. (2013). Optical Counterparts of the Nearest Ultraluminous X-Ray Sources. *The Astrophysical Journal Supplement*, 206:14.

Gladstone, J. C., Roberts, T. P., and Done, C. (2009). The ultraluminous state. *Monthly Notices of the Royal Astronomical Society*, 397:1836–1851.

Goad, M. R., Roberts, T. P., Knigge, C., and Lira, P. (2002). The optical counterpart of the ultraluminous X-ray source NGC 5204 X-1. *Monthly Notices of the Royal Astronomical Society*, 335:L67–L70.

Grisé, F., Kaaret, P., Feng, H., Kajava, J. J. E., and Farrell, S. A. (2010). X-ray Spectral State is not Correlated with Luminosity in Holmberg II X-1. *The Astrophysical Journal Letters*, 724:L148–L152.

Grisé, F., Pakull, M. W., Soria, R., Motch, C., Smith, I. A., Ryder, S. D., and Böttcher, M. (2008). The ultraluminous X-ray source NGC 1313 X-2. Its optical counterpart and environment. *Astronomy and Astrophysics*, 486:151–163.

Heil, L. M., Vaughan, S., and Roberts, T. P. (2009). A systematic study of variability in a sample of ultraluminous X-ray sources. *Monthly Notices of the Royal Astronomical Society*, 397:1061–1072.

Hu, C.-P., Li, K. L., Kong, A. K. H., Ng, C.-Y., and Lin, L. C.-C. (2017). Swift Detection of a 65 Day X-Ray Period from the Ultraluminous Pulsar NGC 7793 P13. *The Astrophysical Journal Letters*, 835:L9.

Hulse, R. A. and Taylor, H. J. (1974). Discovery of a Pulsar in a Close Binary System. In *Bulletin of the American Astronomical Society*, volume 6 of *Bulletin of the American Astronomical Society*, page 453.

Israel, G. L., Belfiore, A., Stella, L., Esposito, P., Casella, P., De Luca, A., Marelli, M., Papitto, A., Perri, M., Puccetti, S., Castillo, G. A. R., Salvetti, D., Tiengo, A., Zampieri, L., D'Agostino, D., Greiner, J., Haberl, F., Novara, G., Salvaterra, R., Turolla, R., Watson, M., Wilms, J., and Wolter, A. (2017a). An accreting pulsar with extreme properties drives an ultraluminous x-ray source in NGC 5907. *Science*, 355:817–819.

Israel, G. L., Papitto, A., Esposito, P., Stella, L., Zampieri, L., Belfiore, A., Rodríguez Castillo, G. A., De Luca, A., Tiengo, A., Haberl, F., Greiner, J., Salvaterra, R., Sandrelli, S., and Lisini, G. (2017b). Discovery of a 0.42-s pulsar in the ultraluminous X-ray source NGC 7793 P13. *Monthly Notices of the Royal Astronomical Society*, 466:L48–L52.

Kaaret, P., Corbel, S., Prestwich, A. H., and Zezas, A. (2003). Radio Emission from an Ultraluminous X-ray Source. *Science*, 299:365–368.

Kaaret, P., Feng, H., and Roberts, T. P. (2017). Ultraluminous X-Ray Sources. *Annual Review of Astronomy and Astrophysics*, 55:303–341.

Kaaret, P., Ward, M. J., and Zezas, A. (2004). High-resolution imaging of the HeII λ4686 emission line nebula associated with the ultraluminous X-ray source in Holmberg II. *Monthly Notices of the Royal Astronomical Society*, 351:L83–L88.

Kajava, J. J. E., Poutanen, J., Farrell, S. A., Grisé, F., and Kaaret, P. (2012). Evolution of the spectral curvature in the ultraluminous X-ray source Holmberg II X-1. *Monthly Notices of the Royal Astronomical Society*, 422:990–996.

King, A. R., Davies, M. B., Ward, M. J., Fabbiano, G., and Elvis, M. (2001). Ultraluminous X-Ray Sources in External Galaxies. *The Astrophysical Journal Letters*, 552:L109–L112.

Kopal, Z. (1959). *Close binary systems*.

Landau, L. and Lifshitz, E. (1951). *The classical theory of Fields*.

Liu, J., Bregman, J. N., and McClintock, J. E. (2009). Hubble Space Telescope Monitoring Reveals a 6.1 Day Period for an Ultraluminous X-Ray Source in NGC 1313. *The Astrophysical Journal Letters*, 690:L39–L42.

Liu, J.-F., Bregman, J., Miller, J., and Kaaret, P. (2007). Optical Studies of the Ultraluminous X-Ray Source NGC 1313 X-2. *The Astrophysical Journal*, 661:165–172.

Liu, J.-F., Bregman, J. N., Bai, Y., Justham, S., and Crowther, P. (2013). Puzzling accretion onto a black hole in the ultraluminous X-ray source M 101 ULX-1. *Nature*, 503:500–503.

Liu, J.-F., Bregman, J. N., and Seitzer, P. (2004). The Optical Counterpart of an Ultraluminous X-Ray Source in NGC 5204. *The Astrophysical Journal*, 602:249–256.

Lorenzin, A. and Zampieri, L. (2009). A comparative analysis of standard accretion discs spectra: an application to ultraluminous X-ray sources. *Monthly Notices of the Royal Astronomical Society*, 394:1588–1596.

Madhusudhan, N., Justham, S., Nelson, L., Paxton, B., Pfahl, E., Podsiadlowski, P., and Rappaport, S. (2006). Models of Ultraluminous X-Ray Sources with Intermediate-Mass Black Holes. *The Astrophysical Journal*, 640:918–922.

Makishima, K., Kubota, A., Mizuno, T., Ohnishi, T., Tashiro, M., Aruga, Y., Asai, K., Dotani, T., Mitsuda, K., Ueda, Y., Uno, S., Yamaoka, K., Ebisawa, K., Kohmura, Y., and Okada, K. (2000). The Nature of Ultraluminous Compact X-Ray Sources in Nearby Spiral Galaxies. *The Astrophysical Journal*, 535:632–643.

Mapelli, M., Colpi, M., and Zampieri, L. (2009). Low metallicity and ultra-luminous X-ray sources in the Cartwheel galaxy. *Monthly Notices of the Royal Astronomical Society*, 395:L71–L75.

Mapelli, M., Ripamonti, E., Zampieri, L., and Colpi, M. (2011a). Dynamics of massive stellar black holes in young star clusters and the displacement of ultra-luminous X-ray sources. *Monthly Notices of the Royal Astronomical Society*, 416:1756–1763.

Mapelli, M., Ripamonti, E., Zampieri, L., and Colpi, M. (2011b). Remnants of massive metal-poor stars: Viable engines for ultra-luminous X-ray sources. *Astronomische Nachrichten*, 332:414.

Mapelli, M. and Zampieri, L. (2014). Roche-lobe Overflow Systems Powered by Black Holes in Young Star Clusters: The Importance of Dynamical Exchanges. *The Astrophysical Journal*, 794:7.

McClintock, J. E. and Remillard, R. A. (2010). *Black hole binaries*, page 157.

Middleton, M. J., Heil, L., Pintore, F., Walton, D. J., and Roberts, T. P. (2015a). A spectral-timing model for ULXs in the supercritical regime. *Monthly Notices of the Royal Astronomical Society*, 447:3243–3263.

Middleton, M. J., Roberts, T. P., Done, C., and Jackson, F. E. (2011). Challenging times: a re-analysis of NGC 5408 X-1. *Monthly Notices of the Royal Astronomical Society*, 411:644–652.

Middleton, M. J., Walton, D. J., Fabian, A., Roberts, T. P., Heil, L., Pinto, C., Anderson, G., and Sutton, A. (2015b). Diagnosing the accretion flow in ultraluminous X-ray sources using soft X-ray atomic features. *Monthly Notices of the Royal Astronomical Society*, 454:3134–3142.

Miller, J. M., Fabbiano, G., Miller, M. C., and Fabian, A. C. (2003). X-Ray Spectroscopic Evidence for Intermediate-Mass Black Holes: Cool Accretion Disks in Two Ultraluminous X-Ray Sources. *The Astrophysical Journal Letters*, 585:L37–L40.

Miller, J. M., Fabian, A. C., and Miller, M. C. (2004). A Comparison of Intermediate-Mass Black Hole Candidate Ultraluminous X-Ray Sources and Stellar-Mass Black Holes. *The Astrophysical Journal Letters*, 614:L117–L120.

Miller, J. M., Fabian, A. C., and Miller, M. C. (2005). On the Robustness of Cool Disc Components in Bright ULXs. *ArXiv Astrophysics e-prints*.

Mineshige, S., Hirano, A., Kitamoto, S., Yamada, T. T., and Fukue, J. (1994). Time-dependent disk accretion in X-ray Nova MUSCAE 1991. *The Astrophysical Journal*, 426:308–312.

Mitsuda, K., Inoue, H., Koyama, K., Makishima, K., Matsuoka, M., Ogawara, Y., Shibazaki, N., Suzuki, K., Tanaka, Y., and Hirano, T. (1984). Energy spectra of low-mass binary X-ray sources observed from Tenma. *Publications of the Astronomical Society of Japan*, 36:741–759.

Mizuno, T., Kubota, A., and Makishima, K. (2001). Spectral Variability of Ultraluminous Compact X-Ray Sources in Nearby Spiral Galaxies. *The Astrophysical Journal*, 554:1282–1289.

Motch, C., Pakull, M. W., Soria, R., Grisé, F., and Pietrzyński, G. (2014). A mass of less than 15 solar masses for the black hole in an ultraluminous X-ray source. *Nature*, 514:198–201.

Mucciarelli, P., Zampieri, L., Treves, A., Turolla, R., and Falomo, R. (2007). X-Ray and Optical Variability of the Ultraluminous X-Ray Source NGC 1313 X-2. *The Astrophysical Journal*, 658:999–1005.

Mukherjee, E. S., Walton, D. J., Bachetti, M., Harrison, F. A., Barret, D., Bellm, E., Boggs, S. E., Christensen, F. E., Craig, W. W., Fabian, A. C., Fuerst, F., Grefenstette, B. W., Hailey, C. J., Madsen, K. K., Middleton, M. J., Miller, J. M., Rana, V., Stern, D., and Zhang, W. (2015). A Hard X-Ray Study of the Ultraluminous X-Ray Source NGC 5204 X-1 with NuSTAR and XMM-Newton. *The Astrophysical Journal*, 808:64.

Pakull, M. W., Grisé, F., and Motch, C. (2006). Ultraluminous X-ray Sources: Bubbles and Optical Counterparts. In Meurs, E. J. A. and Fabbiano, G., editors, *Populations of High Energy Sources in Galaxies*, volume 230 of *IAU Symposium*, pages 293–297.

Pakull, M. W. and Mirioni, L. (2002). Optical Counterparts of Ultraluminous X-Ray Sources. *ArXiv Astrophysics e-prints*.

Patruno, A., Colpi, M., Faulkner, A., and Possenti, A. (2005). Radio pulsars around intermediate-mass black holes in superstellar clusters. *Monthly Notices of the Royal Astronomical Society*, 364:344–352.

Patruno, A. and Zampieri, L. (2008). Optical emission from massive donors in ultraluminous X-ray source binary systems. *Monthly Notices of the Royal Astronomical Society*, 386:543–552.

Patruno, A. and Zampieri, L. (2010). The black hole in NGC 1313 X-2: constraints on the mass from optical observations. *Monthly Notices of the Royal Astronomical Society*, 403:L69–L73.

Paxton, B., Bildsten, L., Dotter, A., Herwig, F., Lesaffre, P., and Timmes, F. (2011). Modules for Experiments in Stellar Astrophysics (MESA). *The Astrophysical Journal Supplement*, 192:3.

Paxton, B., Cantiello, M., Arras, P., Bildsten, L., Brown, E. F., Dotter, A., Mankovich, C., Montgomery, M. H., Stello, D., Timmes, F. X., and Townsend, R. (2013). Modules for Experiments in Stellar Astrophysics (MESA): Planets, Oscillations, Rotation, and Massive Stars. *The Astrophysical Journal Supplement*, 208:4.

Paxton, B., Marchant, P., Schwab, J., Bauer, E. B., Bildsten, L., Cantiello, M., Dessart, L., Farmer, R., Hu, H., Langer, N., Townsend, R. H. D., Townsley, D. M., and Timmes, F. X. (2015). Modules for Experiments in Stellar Astrophysics (MESA): Binaries, Pulsations, and Explosions. *The Astrophysical Journal Supplement*, 220:15.

Pinto, C., Alston, W., Soria, R., Middleton, M. J., Walton, D. J., Sutton, A. D., Fabian, A. C., Earnshaw, H., Urquhart, R., Kara, E., and Roberts, T. P. (2017). From ultraluminous X-ray sources to ultraluminous supersoft sources: NGC 55 ULX, the missing link. *Monthly Notices of the Royal Astronomical Society*, 468:2865–2883.

Pinto, C., Fabian, A., Middleton, M., and Walton, D. (2016a). Ultrafast outflows in ultraluminous X-ray sources. *ArXiv e-prints*.

Pinto, C., Middleton, M. J., and Fabian, A. C. (2016b). Resolved atomic lines reveal outflows in two ultraluminous X-ray sources. *Nature*, 533:64–67.

Pintore, F., Belfiore, A., Novara, G., Salvaterra, R., Marelli, M., De Luca, A., Rigoselli, M., Israel, G., Rodriguez, G., Mereghetti, S., Wolter, A., Walton, D. J., Fuerst, F., Ambrosi, E., Zampieri, L., Tiengo, A., and Salvaggio, C. (2018). A new ultraluminous X-ray source in the galaxy NGC 5907. *Monthly Notices of the Royal Astronomical Society*, 477:L90–L95.

Pintore, F. and Zampieri, L. (2011). Six years of XMM-Newton observations of NGC 1313 X-1 and X-2. *Astronomische Nachrichten*, 332:337.

Pintore, F. and Zampieri, L. (2012). X-ray spectral states and metallicity in the ultraluminous X-ray sources NGC 1313 X-1 and X-2. *Monthly Notices of the Royal Astronomical Society*, 420:1107–1114.

Pintore, F., Zampieri, L., Stella, L., Wolter, A., Mereghetti, S., and Israel, G. L. (2017). Pulsator-like Spectra from Ultraluminous X-Ray Sources and the Search for More Ultraluminous Pulsars. *The Astrophysical Journal*, 836:113.

Pintore, F., Zampieri, L., Wolter, A., and Belloni, T. (2014). Ultraluminous X-ray sources: a deeper insight into their spectral evolution. *Monthly Notices of the Royal Astronomical Society*, 439:3461–3475.

Podsiadlowski, P., Rappaport, S., and Han, Z. (2003). On the formation and evolution of black hole binaries. *Monthly Notices of the Royal Astronomical Society*, 341:385–404.

Pols, O. (2011). " binaries and stellar evolution lecture notes". https://www.astro.ru.nl/~onnop/education/binaries_utrecht_notes/Binaries_ch6-8.pdf.

Pols, O. R., Tout, C. A., Eggleton, P. P., and Han, Z. (1995). Approximate input physics for stellar modelling. *Monthly Notices of the Royal Astronomical Society*, 274:964–974.

Poutanen, J., Lipunova, G., Fabrika, S., Butkevich, A. G., and Abolmasov, P. (2007). Supercritically accreting stellar mass black holes as ultraluminous X-ray sources. *Monthly Notices of the Royal Astronomical Society*, 377:1187–1194.

Ramsey, C. J., Williams, R. M., Gruendl, R. A., Chen, C.-H. R., Chu, Y.-H., and Wang, Q. D. (2006). An Optical Study of Stellar and Interstellar Environments of Seven Luminous and Ultraluminous X-Ray Sources. *The Astrophysical Journal*, 641:241–251.

Rappaport, S., Verbunt, F., and Joss, P. C. (1983). A new technique for calculations of binary stellar evolution, with application to magnetic braking. *The Astrophysical Journal*, 275:713–731.

Rappaport, S. A., Podsiadlowski, P., and Pfahl, E. (2005). Stellar-mass black hole binaries as ultraluminous X-ray sources. *Monthly Notices of the Royal Astronomical Society*, 356:401–414.

Remillard, R. A. and McClintock, J. E. (2006). X-Ray Properties of Black-Hole Binaries. *Annual Review of Astronomy and Astrophysics*, 44:49–92.

Roberts, T. P., Gladstone, J. C., Goulding, A. D., Swinbank, A. M., Ward, M. J., Goad, M. R., and Levan, A. J. (2011). (No) dynamical constraints on the mass of the black hole in two ULXs. *Astronomische Nachrichten*, 332:398.

Roberts, T. P., Goad, M. R., Ward, M. J., and Warwick, R. S. (2003). The unusual supernova remnant surrounding the ultraluminous X-ray source IC 342 X-1. *Monthly Notices of the Royal Astronomical Society*, 342:709–714.

Roberts, T. P., Levan, A. J., and Goad, M. R. (2008). New Hubble Space Telescope imaging of the counterparts to six ultraluminous X-ray sources. *Monthly Notices of the Royal Astronomical Society*, 387:73–78.

Roberts, T. P., Warwick, R. S., Ward, M. J., Goad, M. R., and Jenkins, L. P. (2005). XMM-Newton EPIC observations of the ultraluminous X-ray source NGC 5204 X-1. *Monthly Notices of the Royal Astronomical Society*, 357:1363–1369.

Rybicki, G. B. and Lightman, A. P. (1986). *Radiative Processes in Astrophysics*.

Sanbuichi, K., Yamada, T. T., and Fukue, J. (1993). Self-irradiated accretion disks around Schwarzschild black holes. *Publications of the Astronomical Society of Japan*, 45:443–448.

Shakura, N. I. and Sunyaev, R. A. (1973). Black holes in binary systems. Observational appearance. *Astronomy and Astrophysics*, 24:337–355.

Sirianni, M., Jee, M. J., Benítez, N., Blakeslee, J. P., Martel, A. R., Meurer, G., Clampin, M., De Marchi, G., Ford, H. C., Gilliland, R., Hartig, G. F., Illingworth, G. D., Mack, J., and McCann, W. J. (2005). The Photometric Performance and Calibration of the Hubble Space Telescope Advanced Camera for Surveys. *Publications of the Astronomical Society of the Pacific*, 117:1049–1112.

Soberman, G. E., Phinney, E. S., and van den Heuvel, E. P. J. (1997). Stability criteria for mass transfer in binary stellar evolution. *Astronomy and Astrophysics*, 327:620–635.

Soria, R., Cropper, M., Pakull, M., Mushotzky, R., and Wu, K. (2005). The star-forming environment of an ultraluminous X-ray source in NGC4559: an optical study. *Monthly Notices of the Royal Astronomical Society*, 356:12–28.

Stewart, S. G., Fanelli, M. N., Byrd, G. G., Hill, J. K., Westpfahl, D. J., Cheng, K.-P., O'Connell, R. W., Roberts, M. S., Neff, S. G., Smith, A. M., and Stecher, T. P. (2000). Star Formation Triggering Mechanisms in Dwarf Galaxies: The Far-Ultraviolet, Hα, and H I Morphology of Holmberg II. *The Astrophysical Journal*, 529:201–218.

Stobbart, A.-M., Roberts, T. P., and Wilms, J. (2006). XMM-Newton observations of the brightest ultraluminous X-ray sources. *Monthly Notices of the Royal Astronomical Society*, 368:397–413.

Sutton, A. D., Roberts, T. P., Gladstone, J. C., Farrell, S. A., Reilly, E., Goad, M. R., and Gehrels, N. (2013a). A bright ultraluminous X-ray source in NGC 5907. *Monthly Notices of the Royal Astronomical Society*, 434:1702–1712.

Sutton, A. D., Roberts, T. P., and Middleton, M. J. (2013b). The ultraluminous state revisited: fractional variability and spectral shape as diagnostics of super-Eddington accretion. *Monthly Notices of the Royal Astronomical Society*, 435:1758–1775.

Takeuchi, S., Ohsuga, K., and Mineshige, S. (2013). Clumpy Outflows from Supercritical Accretion Flow. *Publications of the Astronomical Society of Japan*, 65:88.

Tao, L., Feng, H., Grisé, F., and Kaaret, P. (2011). Compact Optical Counterparts of Ultraluminous X-Ray Sources. *The Astrophysical Journal*, 737:81.

Tao, L., Kaaret, P., Feng, H., and Grisé, F. (2012). The Nature of the UV/Optical Emission of the Ultraluminous X-Ray Source in Holmberg II. *The Astrophysical Journal*, 750:110.

Tauris, T. M. and van den Heuvel, E. P. J. (2006). *Formation and evolution of compact stellar X-ray sources*, pages 623–665.

Tauris, T. M., van den Heuvel, E. P. J., and Savonije, G. J. (2000). Formation of Millisecond Pulsars with Heavy White Dwarf Companions:Extreme Mass Transfer on Subthermal Timescales. *The Astrophysical Journal Letters*, 530:L93–L96.

Titarchuk, L. (1994). Generalized Comptonization Models and Application to the Recent High-Energy Observations. *The Astrophysical Journal*, 434:570.

Urquhart, R. and Soria, R. (2016). Optically thick outflows in ultraluminous supersoft sources. *Monthly Notices of the Royal Astronomical Society*, 456:1859–1880.

van den Heuvel, E. P. J. (1994). Interacting binaries: topics in close binary evolution. In Shore, S. N., Livio, M., van den Heuvel, E. P. J., Nussbaumer, H., and Orr, A., editors, *Saas-Fee Advanced Course 22: Interacting Binaries*, pages 263–474.

Verbunt, F. and Zwaan, C. (1981). Magnetic braking in low-mass X-ray binaries. *Astronomy and Astrophysics*, 100:L7–L9.

Vierdayanti, K., Mineshige, S., Ebisawa, K., and Kawaguchi, T. (2006). Do Ultraluminous X-Ray Sources Really Contain Intermediate-Mass Black Holes? *Publications of the Astronomical Society of Japan*, 58:915–923.

Vierdayanti, K., Watarai, K.-Y., and Mineshige, S. (2008). On Black Hole Mass Estimation from X-Ray Spectra of Ultraluminous X-Ray Sources. *Publications of the Astronomical Society of Japan*, 60:653.

Walton, D. J., Harrison, F. A., Grefenstette, B. W., Miller, J. M., Bachetti, M., Barret, D., Boggs, S. E., Christensen, F. E., Craig, W. W., Fabian, A. C., Fuerst, F., Hailey, C. J., Madsen, K. K., Parker, M. L., Ptak, A., Rana, V., Stern, D., Webb, N., and Zhang, W. W. (2014). Broadband X-Ray Spectra of the Ultraluminous X-Ray Source Holmberg IX X-1 Observed with NuSTAR, XMM-Newton, and Suzaku. *The Astrophysical Journal*, 793:21.

Walton, D. J., Middleton, M. J., Rana, V., Miller, J. M., Harrison, F. A., Fabian, A. C., Bachetti, M., Barret, D., Boggs, S. E., Christensen, F. E., Craig, W. W., Fuerst, F., Grefenstette, B. W., Hailey, C. J., Madsen, K. K., Stern, D., and Zhang, W. (2015). NuSTAR, XMM-Newton, and Suzaku Observations of the Ultraluminous X-Ray Source Holmberg II X-1. *The Astrophysical Journal*, 806:65.

Watarai, K.-y. and Fukue, J. (1999). Radiative Disk Winds from a Self-Similar Slim Disk. *Publications of the Astronomical Society of Japan*, 51:725.

Watarai, K.-y., Fukue, J., Takeuchi, M., and Mineshige, S. (2000). Galactic Black-Hole Candidates Shining at the Eddington Luminosity. *Publications of the Astronomical Society of Japan*, 52:133.

Weisberg, J. M., Taylor, J. H., and Fowler, L. A. (1981). Gravitational waves from an orbiting pulsar. *Scientific American*, 245:74–82.

Wolter, A., Esposito, P., Mapelli, M., Pizzolato, F., and Ripamonti, E. (2015). NGC 2276: a remarkable galaxy with a large number of ultraluminous X-ray sources. *Monthly Notices of the Royal Astronomical Society*, 448:781–791.

Wolter, A., Fruscione, A., and Mapelli, M. (2018). The X-Ray Luminosity Function of Ultraluminous X-Ray Sources in Collisional Ring Galaxies. *The Astrophysical Journal*, 863:43.

Wu, K., Soria, R., Hunstead, R. W., and Johnston, H. M. (2001). Optical spectroscopy of GX 339-4 during the high-soft and low-hard states - II. Line ionization and emission region. *Monthly Notices of the Royal Astronomical Society*, 320:177–192.

Zampieri, L., Impiombato, D., Falomo, R., Grisé, F., and Soria, R. (2012). Searching for the orbital period of the ultraluminous X-ray source NGC 1313 X-2. *Monthly Notices of the Royal Astronomical Society*, 419:1331–1337.

Zampieri, L., Mucciarelli, P., Falomo, R., Kaaret, P., Di Stefano, R., Turolla, R., Chieregato, M., and Treves, A. (2004). The Ultraluminous X-Ray Source NGC 1313 X-2 (MS 0317.7-6647) and Its Environment. *The Astrophysical Journal*, 603:523–530.

Zampieri, L. and Roberts, T. P. (2009). Low-metallicity natal environments and black hole masses in ultraluminous X-ray sources. *Monthly Notices of the Royal Astronomical Society*, 400:677–686.

Zdziarski, A. A. and Gierliński, M. (2004). Radiative Processes, Spectral States and Variability of Black-Hole Binaries. *Progress of Theoretical Physics Supplement*, 155:99–119.